The 2006 Eruption of Augustine Volcano, Alaska
Power, J.A., Coombs, M.L., and Freymueller, J.T., editors
U.S. Geological Survey Professional Paper 1769

Chapter 15

Petrology and Geochemistry of the 2006 Eruption of Augustine Volcano

By Jessica F. Larsen[1], Christopher J. Nye[2], Michelle L. Coombs[3], Mariah Tilman[1], Pavel Izbekov[1], and Cheryl Cameron[2]

Abstract

Deposits from the 2006 eruption of Augustine Volcano, Alaska, record a complex history of magma mixing before and during the eruption. The eruption produced five major lithologies: low-silica andesite scoria (LSAS; 56.5 to 58.7 weight percent SiO_2), mostly during the initial explosive phase; high-silica andesite pumice (HSA; 62.2 to 63.3 weight percent SiO_2), prevalent during the continuous phase; dense low-silica andesite (DLSA; 56.4 to 59.3 weight percent SiO_2), predominantly during the late effusive phase; and dense intermediate andesite (DIA) and banded clasts, present throughout the eruption but most abundant in the continuous phase. The DIA and banded clasts have compositions that fall between and partially overlap the ranges noted above. All rock types are phenocryst-rich (36 to 44 volume percent), containing plagioclase, orthopyroxene, augite, Fe-Ti oxides, olivine, and rare amphibole, apatite, and anhydrite. Glasses from tephra and flow-deposit clasts range from 66 to nearly 80 weight percent SiO_2 and represent highly evolved melt relative to the bulk rock compositions. Fe-Ti oxides recorded f_{O_2}~2 log units above the Ni-NiO buffer and temperatures of 904±47°C and 838±14°C from LSAS and HSA samples, respectively, with the intermediate lithologies falling in the middle of these ranges. The dense low-silica andesite and scoria (collectively LSA) are compositionally nearly identical, and trace-element patterns show that the HSA is not the result of shallow crustal fractionation of the LSA. The petrological and geochemical data indicate that two-component magma mixing between the LSA and HSA caused the compositional spread in eruptive products. The phenocryst population in the LSA suggests that it represents a hybrid formed from the HSA and an unerupted, basaltic “replenishing” magma. On the basis of petrological and geophysical observations reported here and elsewhere in this volume, the HSA was stored as a crystal-rich mush with its top at ~5-km depth. An influx of basalt remobilized and partially mixed with a portion of the mush, forming the hybrid LSA. The lower viscosity LSA ascended towards the surface as a dike, erupting during the explosive phase in mid-January 2006. In late January, a large explosion produced the first significant volumes of HSA, followed by several days of rapid HSA effusion during the eruption’s continuous phase. After a three-week hiatus marked by elevated gas output, signifying an open system, degassed LSA erupted during the final, effusive phase. Consistency in eruptive styles and compositions suggests that the HSA magma body may have been similarly rejuvenated during the past several eruptions.

Introduction

Understanding the magmatic processes that drive eruptions is an integral component of volcano studies. Studying the deposits of recent, well-monitored eruptions allows us to place petrologic studies in a context that would be impossible for prehistoric or more poorly documented eruptions, thus yielding more insight into the link between what happens below the volcano’s surface and what comes out of the vent. Augustine Volcano, located in Cook Inlet in south-central Alaska, is one of the most active volcanoes in the Aleutian arc, with eight confirmed explosive eruptions in the past 200 years (Waythomas and Waitt, 1998). Because of the frequency of eruptions and the unique hazards that Augustine presents, understanding the processes that trigger eruptive events there is an important role of the Alaska Volcano Observatory (AVO). The consistent

---

[1] Alaska Volcano Observatory, Geophysical Institute, 903 Koyukuk Drive, University of Alaska, Fairbanks, AK 99775.

[2] Alaska Volcano Observatory, Alaska Division of Geological and Geophysical Surveys, 3354 College Road, Fairbanks, AK 99709.

[3] Alaska Volcano Observatory, U.S. Geological Survey, 4200 University Drive, Anchorage, AK 99508.

pattern of eruptions, in terms of precursory activity and eruptive style, combined with the increased amount of independent datasets for the 2006 eruption, makes Augustine suitable for cross-disciplinary studies of volcanic processes that can be applied to less well monitored volcanoes. The frequency of eruptions at Augustine also presents an excellent opportunity to compare petrologic data from the three most recent eruptions in 1976, 1986, and 2006.

Petrologists have long recognized that many products of subduction-zone volcanoes show evidence of magma mixing, and recent studies of historical and ongoing eruptions show that mixing is often temporally linked to magma's arrival at the earth's surface (for example, Coombs and others, 2000; Costa and Chakraborty, 2004; Izbekov and others, 2002; Murphy and others, 2000; Nakamura, 1995; Pallister and others, 1996). Understanding the process of magma mixing as a potential eruption trigger is important in the case of Augustine Volcano's most recent eruptions. Magmas erupted at Augustine in the 30 years prior to the 2006 eruption show clear evidence of magma mixing in the form of mingling (banded clasts) and hybridization at both macro and micro scales (Johnston, 1978; Roman and others, 2005). Both the 1976 and 1986 eruptions are thought to have been triggered by the injection of basaltic magma into a more silica-rich andesite/dacite magma body. Their whole-rock compositions are similar and limited in range between 56 to 64 weight percent SiO_2. The 1976 deposits include olivine and hornblende phenocrysts that appear to have grown in a mafic magma that was not found in the erupted material (Johnston, 1978). After the 1986 eruption, a better understanding of magma storage and transport at Augustine emerged from the increased quantity of geophysical and petrological data (Harris, 1994; Power, 1988; Roman and others, 2005). Roman and others (2005) suggest a model of interconnected dikes to explain how Augustine commonly produces mixed magmas but maintains a relatively narrow compositional range (56–64 weight percent SiO_2) throughout 200 years of historical activity, while also maintaining compositional heterogeneity throughout individual eruptive cycles.

The 2006 eruption of Augustine Volcano followed a sequence of events similar to those in 1976 and 1986. A precursory phase began April 30, 2005, and both seismicity and inflation of the edifice slowly increased over the next 7 months (Jacobs and McNutt, this volume; Cervelli and others, 2006). By mid-December 2005, earthquakes were occurring at a rate of 15 per day at a depth close to sea level, along with intermittent steam explosions, the largest of which were observed on December 10, 12, and 15 (Power and others, 2006). On January 11, 2006, seismometers recorded two explosions at Augustine, marking the onset of the explosive phase of the eruption. The explosive phase was dominated by a series of 13 discrete Vulcanian blasts that produced pyroclastic flows and ash fall rich in low-silica andesite scoria (Coombs and others, this volume; Vallance and others, this volume; Wallace and others, this volume; fig. 1). On January 28, Augustine entered a continuous eruptive phase dominated by low-level, ash-rich plumes and multiple pyroclastic flows, likely the result of rapid effusion and collapse of lava at the summit (Coombs and others, this volume; Wallace and others, this volume). Deposits from this phase include crystal-rich high-silica andesite and lesser amounts of banded clasts, dense intermediate andesite, and dense low-silica andesite (Vallance and others, this volume). After a hiatus in eruptive activity that lasted from February 10 to March 3, the eruption entered an effusive phase dominated by dome growth and the extrusion of rubbly lava flows accompanied by small-volume block-and-ash flows (Coombs and others, this volume). The effusive deposits contained primarily dense low-silica andesite and dense intermediate andesite (Vallance and others, this volume). The 2006 eruptive sequence ended on March 16, 2006, with the cessation of drumbeat earthquakes that accompanied the dome growth (Power and Lalla, this volume).

In this paper we present an overview of the petrography, petrology, and geochemistry of the products from the 2006 Augustine eruption. Our results are tied to the dominant lithologies erupted during each of the explosive, continuous, and effusive eruptive phases. We show that the eruptive products are the result of hybridization of an unerupted replenishing mafic magma, not seen in the eruption products in its pure, unmixed form, and a shallowly residing high-silica andesite body that was reinvigorated just before eruption. The data presented in this chapter are used in conjunction with companion studies on melt inclusion preeruptive volatile contents (Webster and others, this volume), geodetic constraints (Cervelli and others, this volume), and reaction-rim growth on olivines (Tilman, 2008), among others, to develop a model for the locations of magma storage and the timescales of magma movement before and during the different phases of the 2006 eruption. This model provides one explanation for the conveyor-belt-like similarity and frequency of historic Augustine eruptions.

Geological Setting

Augustine Volcano lies in the eastern Aleutian arc, approximately 80 km above the Wadati-Benioff zone (Syracuse and Abers, 2006). Volcanism in the eastern arc is caused by northwestward subduction of the Pacific Plate beneath the North American Plate at a rate of roughly 55 mm/yr (Kienle and Swanson, 1983).

The wholly Quaternary volcano sits atop crust of the Peninsular Terrane, thought to have amalgamated with nearby terranes prior to Late Jurassic time and accreted to North America in the mid-Cretaceous (Detterman and Reed, 1980). The terrane comprises Mesozoic marine and nonmarine sedimentary rocks of the Jurassic Naknek Formation, which crop out on the south flank of Augustine from sea level to 400 m above mean sea level (amsl). It is overlain by a thin veneer of friable sandstone and conglomerate of the Cretaceous Kaguyak Formation (Waitt, this volume). Seismic velocity studies suggest that these rocks have been uplifted on the south shoulder by faulting, and that lower-velocity sediments underlie the volcano on other sectors from sea level to ~900

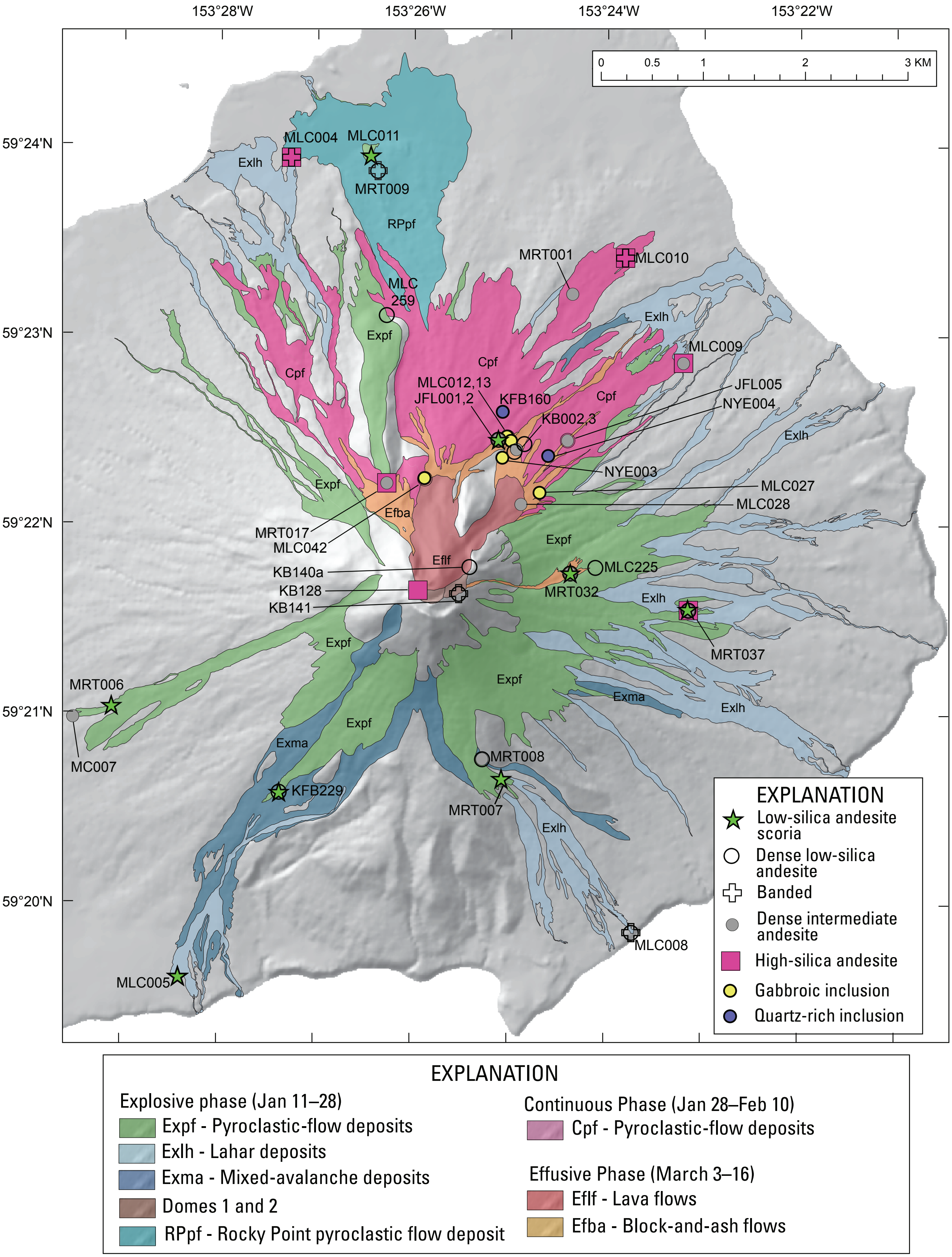

Figure 1. Map of Augustine Island showing deposits from the 2006 eruption and the location of samples used in this study. The 06AU- preface on sample locations is removed for clarity. Units simplified from Coombs and others (this volume).

m below mean sea level (bmsl) (Kienle and others, 1979). Beneath the summit, an intermediate-velocity region from sea level down to 900 m bmsl is interpreted as sedimentary strata that have been interlaced with volcanic dikes and sills (Kienle and others, 1979). High-velocity rocks everywhere underlie the volcano below 900 m bmsl, interpreted by Kienle and others as zeolitized Naknek Formation.

The oldest known products of Augustine Volcano are late Pleistocene in age (Johnston, 1978). They comprise poorly sorted bedded fragmental material, with clasts of olivine basalt as large as 20 cm in diameter, as well as radially fractured clasts of dense juvenile rhyolite. There is extensive palagonitization of the material and it appears to be the result of hyaloclastite eruption likely from a flank vent. The upper 20 cm is interlayered with the base of a rhyolitic tephra-fall deposit.

Records of early to middle Holocene Augustine eruptions are scarce and limited to the base of a few small tephra exposures on the south flank and some distal ashes with Augustine compositional affinities (Waitt, this volume). The late Holocene, prehistoric eruptive record is more complete, and shows that Augustine often erupted explosively, producing sometimes thick tephra falls, an apron of flowage deposits, and an edifice consisting of overlapping lava domes and short flows. In addition, repeated edifice failures and debris avalanches have marked the late Holocene record, with the most recent in 1883. Augustine has erupted historically in 1883, 1935, 1964, 1976, and 1986, each time producing andesitic through dacitic ash fall and pyroclastic flows.

Several lines of evidence have been used to argue that Augustine's subvolcanic plumbing system is immature and that it lacks a large, well-developed magma storage region, or "magma chamber." Recent eruptions have modest volumes (<0.5 km^3), thus involving small magma batches. Compositional heterogeneity is the norm and persisted throughout the 1986 eruption, suggesting that the eruption was not fed from a single magma storage region but instead by a system of small-volume dikes in the shallow subsurface, some of which contained residual magma from 1976 (Roman and others, 2005). Between eruptions, minimal edifice deformation and gas output have been observed (McGee and others, this volume; Power and others, 2006)

Despite the apparent absence of a large shallow magma body beneath Augustine, there are some indications of shallow-crustal magma storage and crystallization prior to previous eruptions. Seismicity prior to the 1976 eruption outlined a central, narrow plumbing system that reached from 8 km to the surface (Kienle and others, 1979). About half of Holocene eruptions produced magmas that contain hornblende, and Al-in-hornblende geobarometry from two Holocene fall units yields equilibrium pressures of 100 to 260 MPa, equivalent to depths between 3.5 and 9 km (Tappen and others, 2009). Melt inclusions in crystals within 1986 and prehistoric magmas contain wide ranges in both dissolved water and carbon dioxide, indicating crystallization at depths mostly between 8 km and several hundred meters bsl (Roman and others, 2005; Webster and others, this volume).

Sample Descriptions

Clasts within deposits of the 2006 eruption were initially separated into five major lithologic groups on the basis of hand-sample characteristics, primarily color and vesicularity (Vallance and others, this volume; fig. 2). Subsequent whole-rock analyses confirm the initial categories. The five lithologies are present in most deposits from the eruption, though in varying proportions. They are:

1. Low-silica andesite scoria (LSAS), almost exclusively erupted during the 2006 explosive phase, representing ~45 percent of the explosive-phase ejecta, with less than 3 percent appearing during the remainder of the eruption. LSAS clasts are moderately vesicular, with black to reddish-brown cores and olive-green to light-gray rinds.

2. High-silica andesite (HSA), most abundant in continuous-phase deposits but also present in explosive-phase ejecta. The most evolved whole-rock, matrix glass, and mineral compositions of 2006 ejecta belong to the HSA, which accounts for >5 to 30 percent of clasts within explosive-phase units, approximately 80 percent of continuous-phase deposits, and <10 percent of effusive phase deposits (Vallance and others, this volume). HSA mostly occurs as rounded, crystal-rich, slightly friable clasts that are light to dark gray, moderately vesicular, and often colored by oxidation.

3. Dense intermediate andesite (DIA), erupted during all eruptive phases but most prevalent in deposits of the continuous-phase. This lithology was originally identified in the field by its medium-grey color and makes up approximately 10 percent of explosive-phase ejecta and a third of continuous-phase ejecta (Vallance and others, this volume). We note, however, that some DIA clasts, especially in the explosive phase, may be accidental lithics of pre-2006 dome lavas. DIA is found as rounded to angular, medium to light gray, poorly to nonvesicular clasts, or as lava.

4. Dense low-silica andesite (DLSA), which composes the effusive-phase lava flows and is present throughout the eruption products in varying proportions as clasts in flow and fall deposits. DLSA makes up 8 to 25 percent of the deposits from the explosive and continuous phases and ~60 percent of effusive-phase deposits (Vallance and others, this volume). It is dark gray to black, poorly to nonvesicular, and commonly forms angular clasts, some of which have breadcrust rinds.

5. Banded clasts are any combination of the above colors and texture that show distinct to diffuse banding. They are found throughout the eruption but are most prevalent during the continuous phase.

In addition to these five major lithologies, crystal-rich, fine-grained gabbroic (FGGI) and quartz-rich inclusions were

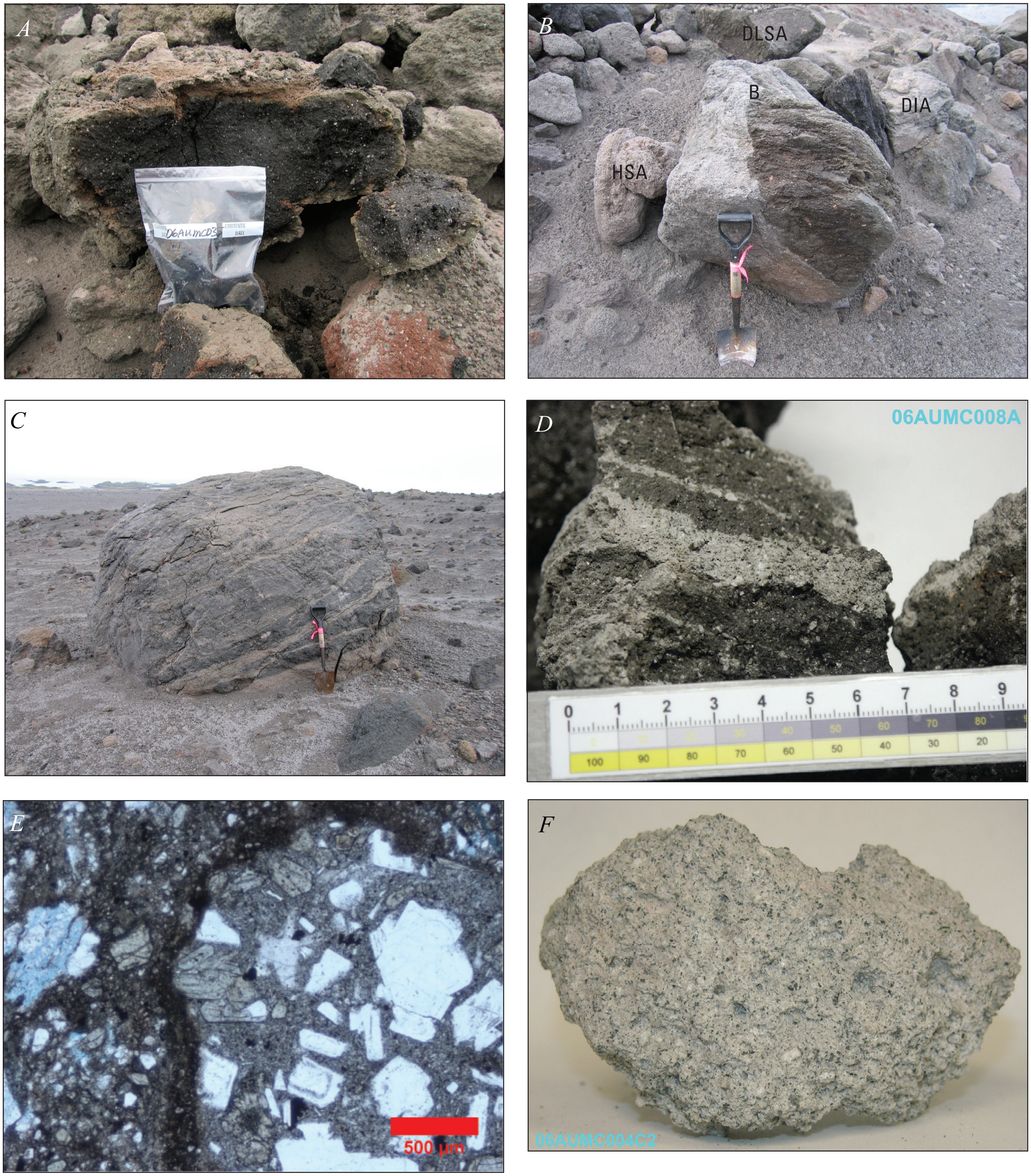

Figure 2. Photographs depicting typical occurrences and major lithologies of deposits from the 2006 Augustine eruption. *A,* Broken clast of low-silica andesite scoria with olive green rind and black interior, within an explosive-phase pyroclastic-flow deposit. Sample site 06AUMLC035. *B,* Continuous-phase pyroclastic-flow deposit containing high-silica andesite (HSA), dense intermediate andesite (DIA), dense low-silica andesite (DLSA), and banded (B) clasts. *C,* Large banded boulder found in Rocky Point pyroclastic-flow deposit from late in the explosive phase. *D,* Interior of banded clast 06AUMC008a, collected from an explosive-phase pyroclastic-flow deposit, showing distinct bands of high- and low-silica andesite. Scale is in centimeters. *E,* Transmitted-light photomicrograph showing crystal-rich and crystal-poor regions of sample 06AUMC007b from the January 13–14 low-silica andesite scoria. *F,* High-silica andesite sample 06AUMC004c2.

sampled from the continuous- and effusive-phase deposits (fig. 3). Fine-grained gabbroic inclusions are salt and pepper in color, nearly holocrystalline, and finely vesicular. They are almost exclusively found as inclusions within DLSA lavas of the effusive phase. Quartz-rich inclusions were found in continuous-phase deposits as light gray or salt-and-pepper bands or pods in larger andesite clasts.

Samples were collected by AVO scientists during the course of the eruption on January 12 and 24, February 8 and 20, and May 13 and after the eruption during August 2006. A geologic map of the 2006 deposits (Coombs and others, this volume) was used to determine sampling localities in order to collect samples from as many of the eruptive events as possible (fig. 1). For each eruptive unit, we collected samples of the multiple lithologies present in most deposits (table 1 and appendix 1). In addition to 2006 samples, we collected samples from a Pleistocene outcrop on the south flank of the island that contains coevally erupted hyaloclastite and pumice (Waitt, this volume), and some clasts from 1976 and 1986 pyroclastic flows for whole-rock analysis.

Analytical Methods

Major and trace element compositions of 70 samples from the 2006 eruption were determined at the Washington State University (WSU) Geoanalytical Laboratory using XRF and ICP-MS techniques (table 2 and appendix 3).[4] Samples were cleaned in deionized water, dried for several days at less than 100°C, partially crushed to pea-sized or smaller grains, and then sent to WSU for analysis. x-ray fluorescence and ICP-MS analyses were conducted following the methods outlined in Johnson and others (1999) and Knaack and others (1994), respectively. All intensity values were concatenated and reduced using a single calibration file to reduce interbatch analytical variations.

Petrographic analysis consisted of documentation of the groundmass and phenocryst types and textures and point-count analyses of thin sections. At least five thin sections for each of the five main lithologic types were counted for modal analyses. Point counts were conducted using an automated stage with a minimum of 1,000 points per slide, including void space. Normalized percentages were calculated after removing void counts.

Phenocryst, microlite, and groundmass-glass compositions were determined at the University of Alaska Fairbanks (UAF) Advanced Instrumentation Lab (AIL) using a Cameca SX-50 electron microprobe equipped with four wavelength-dispersive spectrometers and one energy-dispersive spectrometer. Phenocryst phases were analyzed for major elements using a 15-KeV, 10-nA focused beam and standard ZAF corrections. Glasses were analyzed using a 15-KeV,

---

[4] Note that tables 2 through 8 are at the back of this chapter.

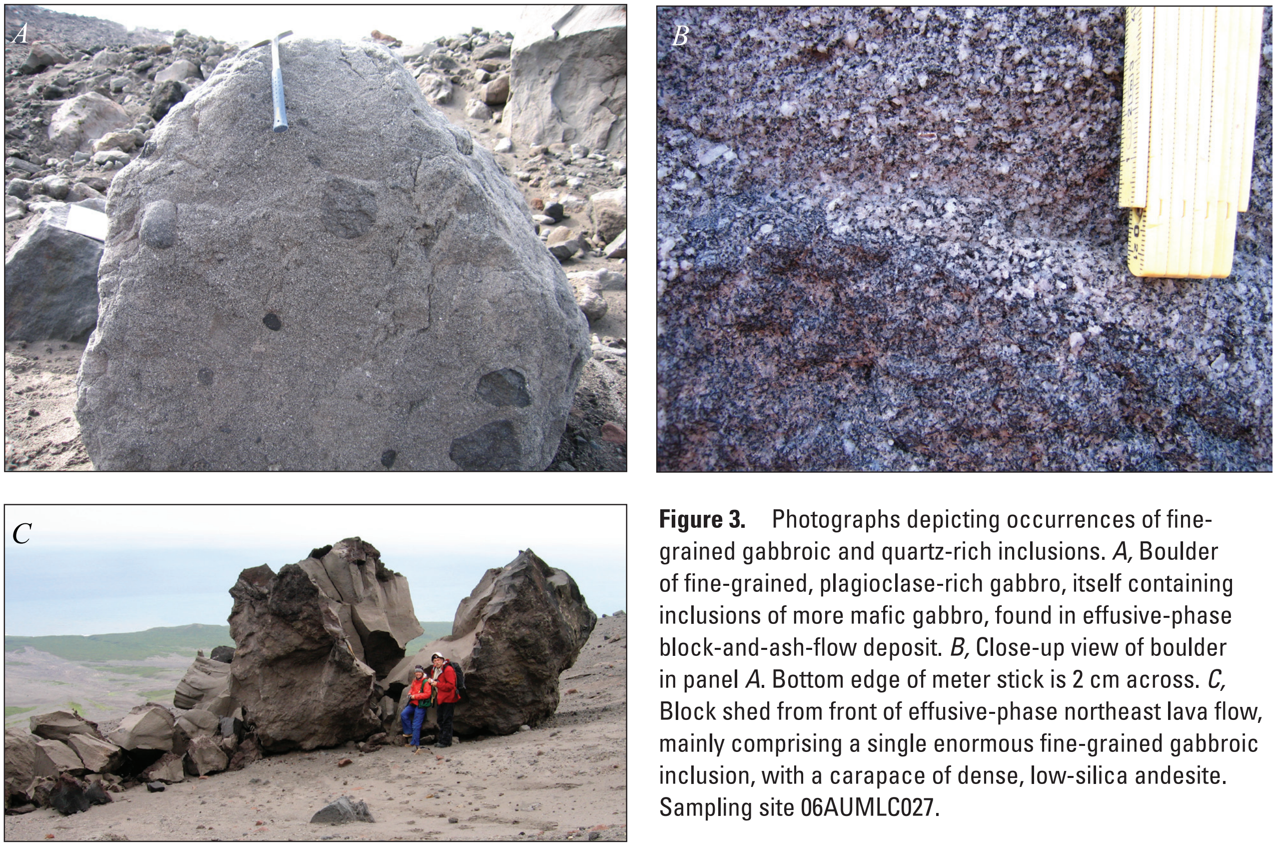

Figure 3. Photographs depicting occurrences of fine-grained gabbroic and quartz-rich inclusions. *A,* Boulder of fine-grained, plagioclase-rich gabbro, itself containing inclusions of more mafic gabbro, found in effusive-phase block-and-ash-flow deposit. *B,* Close-up view of boulder in panel *A*. Bottom edge of meter stick is 2 cm across. *C,* Block shed from front of effusive-phase northeast lava flow, mainly comprising a single enormous fine-grained gabbroic inclusion, with a carapace of dense, low-silica andesite. Sampling site 06AUMLC027.

Table 1. Samples of Augustine Volcano 2006 eruptive products used in this study, sorted by eruptive unit and lithologic type.

[Unit names are defined by Coombs and others (this volume). On our figure 1, Expf, Expc, and Expct are lumped into Expf and Cpf and Cpfw are lumped into Cpf for simplicity. In addition, the appendix contains new major and trace element data for 2 samples from the 1883(?) lava flow; 3 samples from 1964 pyroclastic flows; 5 samples from 1976 pyroclastic flows; 11 samples from 1986 pyroclastic flows; 5 samples from early Holocene pumice fall and bombs; 8 juvenile clasts from the late Pleistocene basalt/basaltic andesite hyaloclastite; 3 dense juvenile rhyolite clasts from within the hyaloclastite; and 3 rhyolite pumice clasts from the fall unit directly overlying the hyaloclastite. The prefix "06AU" has been removed from all sample names for brevity. (#) indicates that the sample was analyzed for major and trace elements]

Deposit dates	Phase	Unit	Low-silica andesite scoria	Dense low-silica andesite	Banded	Dense intermediate andesite	High Silica Andesite	Inclusion
Jan 13–14 (E5–8)	Explosive	Expct, Expf	MRT037c#	MRT037b# MRT037f# MRT037a		MRT037e#		MRT037d# (low-K)
Jan 13–14 (E3–8)			MC005a# MC005c.p3# MC005c.p4# MC005c.p5# MC008b.p1# MC008b.p2# KFB229a# MRT007b#	MC008b.p3# KFB229b# MRT008a#	MC005c.p1# MC008a.f# MC008a.m# MC005c.p2	MC008b.l1# MRT008b#	MC005c.p2# (pumice)	
Jan 17 (E9)		Expf	MC007c#			MRT006#		
Jan 21		Exd1		KB141b#	KB141a			
Jan 22–28		Exd2					JWV059a# KFB128a#	
Jan 27 (E10)		Expc		MLC259e# MLC225#				
		RPpf	MRT009b# MC011a#		MC004c3m# MC004c3 MRT009c		MC004a MC004c1# MC004c2#	
Jan 28–Feb 4	Continuous	Cpf			MC010p2# MC010p3m# MC010p3	MC009l1# MRT001b#	MC009p1# MC009p2# MC010p1#	NYE004# (high-Si) KFB160# (high-Si)
		Cpfw				MRT017a#	MRT017b#	
March 3–16	Effusive	Eflf		KB140B# MLC042b# MLC057#		MLC028#		MLC042a# (gabbroic)
		Efba	JFL001e# MRT032c#	JFL001d# JFL001f# JFL002# JFL005b# KB003# MC012b# MRT032a# NYE001#		JFL001b# JFL005a# KB002A# KB002B# KB002C# MRT032b#		MC012a# (gabbroic) MC013a# (gabbroic) MC027a# (gabbroic) NYE003# (gabbroic)

10-nA, 10-micron-wide defocused beam and a routine to minimize Na loss. Comenditic glass standard KN-18 was routinely analyzed during glass analyses to monitor instrument drift.

Fe-Ti oxide grains were separated from crushed samples of the major lithologies using a magnet. Grain mounts of the separated oxides were polished and touching ilmenite-titanomagnetite pairs without obvious disequilibrium textures or exsolution lamellae were analyzed by microprobe. Analyses consisted of core to rim transects, in 3-micron increments across each grain, with anomalously high Si analyses removed because of possible interference with glass. The analyses showed no significant change in composition from core to rim, so the values for each oxide were averaged. The pairs were subjected to the Bacon and Hirschman (1988) equilibrium test, and those found to be in equilibrium were run through QUILF (Andersen and others, 1993) to determine the temperature and oxygen fugacity (f_{O_2}). As discussed below, the high f_{O_2} of the magmas is outside of the calibration for the QUILF algorithm (Evans and others, 2006; Lattard and others, 2005); thus temperatures presented herein have been adjusted downward by 30°C (Rutherford and Devine, 1996).

Results

Petrography

Eruptive products of the 2006 eruption are typical of andesite and dacite produced by convergent-margin volcanoes worldwide: they are porphyritic, variably vesicular, and have glassy to microlite-rich groundmasses. The 2006 magmas contained phenocrysts of, in order of decreasing abundance, plagioclase, augite, orthopyroxene, Fe-Ti oxides, olivine, and rare amphibole, apatite, anhydrite, quartz, and biotite. (fig. 4; table 2). Amphibole is rare within all major lithologies. Apatite and anhydrite are present in less than 0.6 volume percent in all lithologies, and apatite exists mainly as inclusions within plagioclase. Biotite, quartz, significant anhydrite, and abundant amphibole are present only within the FGGI minor lithology. Plagioclase is the most abundant mineral phase by far, averaging from 27 to 32 volume percent in the major lithologies.

All rock types are phenocryst-rich, with LSAS, DLSA, DIA, and banded samples ranging from 36 to 40 volume percent phenocrysts in terms of average values (table 2), though we note that individual samples may lie outside this range (appendix 2). Two fine-grained gabbroic inclusions have an average of 74 volume percent phenocrysts.

Of the five major lithologies, high-silica andesite samples are the richest in phenocrysts. From point-count analysis of seven HSA samples, we found an average of 45 volume percent crystals, with a standard deviation of 7 volume percent. Interestingly, three replicate point-count analyses of a single HSA thin section yielded results of 40 to 57 volume percent, an unexpectedly high range (appendix 2). (Replicate analyses of LSAS and DLSA samples yielded ranges within a few volume percent.) In addition, we noted that hand specimens of HSA appeared particularly crystal-rich. To further assess HSA phenocryst content, we use a mass balance approach. If we perform a linear least squares, mass balance regression of the phenocryst compositions determined by electron microprobe (see section on Phase Descriptions and Compositions below), using their modal percentages from the point counts against the whole rock compositions to derive the volume percent of glass in the groundmass, we find that the point-count modes yield significant mismatches in Si, Mg, Fe, and Ca. In contrast, when glass content is reduced from 55 to 46 volume percent and other phenocrysts are increased proportionally, we obtain a better fit in the mass balance calculation. We suggest that the disparity between the point-count and mass balance methods for the high-silica andesite is a result of assigning groundmass glass to points where the glass may account for less than the total thickness of the thin section. Thus the actual crystallinity of the high-silica andesite magma is likely closer to 55 volume percent.

All lithologies are variably vesicular, even those described as relatively dense, and range from 16 to 45 volume percent porosity. Average vesicularities for the major lithologies are 37.3 volume percent for HSA, 38.7 volume percent for banded, 33.6 volume percent for LSAS, 22.1 volume percent for DIA, and 19.8 volume percent for DLSA (fig. 5, table 2). Void spaces are commonly irregularly shaped and variably sized, from sub-mm size to more than 10 mm.

Both DLSA and LSAS have dark gray to brown groundmasses, dominated by abundant microlites and containing very little residual glass (<1 volume percent by point counts; figs. 5, 6*A*, *B*). In contrast, HSA pumice clasts have groundmass composed almost wholly of clear, microlite-free glass that often forms finely stretched filaments (fig. 6*C*). These filaments and bubble voids are often stretched or aligned in one orientation. Based on normalized point-count totals, the HSA contains an average of 51.7 volume percent glass and 1.4 volume percent microlite-rich groundmass (fig. 5). The DIA and banded clasts contain a mix of both groundmass textures, averaging 10.6 and 37.8 volume percent glass and 51.5 and 37.8 volume percent microlite-rich groundmass in the DIA and banded clasts respectively.

The major lithologies, especially LSAS, all show some glomerophenocrystic plagioclase, pyroxene, olivine, or symplectite olivine. The FGGI minor lithology contains notable pervasive skeletal plagioclase crystals, with a more equigranular texture than that observed in the major lithologies. Quartz-rich inclusions are marked by polycrystalline plagioclase and quartz masses as large as several mm in diameter, surrounded by a microlitic groundmass of quartz, plagioclase, orthopyroxene, and glass. Patches of granophyric texture are present. Graphic textures in plagioclase, hornblende, orthopyroxene, and clinopyroxene are occasionally present in samples from the major lithologies.

Diffuse to sharp banding representing various stages of magma-mingling and hybridization is evident in Augustine deposits at all scales, from large boulders to micro-scale textures seen in thin section (fig. 2*B* to 2*E*). Heterogeneity is also observed from deposits from each phase of the eruption, in variations in glass color (tan to colorless), phenocryst abundances (appendix 2), and disequilibrium textures.

Whole-Rock Compositions

Systematic differences in whole-rock composition among the products of the 2006 eruption mirror the macroscopic differences first identified among lithologies in the field. Lavas and pyroclasts from the 2006 eruption range from 56.5 to 63.2 weight percent SiO_2, fully spanning the andesite range and extending slightly into both the basaltic-andesite and dacite fields (fig. 7; table 3). For simplicity we refer to them all as andesite. The samples range from 0.7 to 1.1 weight percent K_2O and straddle the low-K to medium-K boundary, which is low by comparison with other Aleutian arc lavas, but not with convergent margin lavas worldwide (Gill, 1981). Analyzed LSAS samples range from 56.5 to 58.7 weight percent SiO_2 and DLSA from 56.4 to 59.3 weight percent SiO_2. HSA samples span 62.2 to 63.3 weight percent SiO_2, though all but one sample cluster near 62.2 weight percent. DIA and banded samples fall between and partially overlap these ranges. Fine-grained gabbroic inclusions (FGGI) range from 54.5 to 57 weight percent SiO_2 and fall along a lower K_2O trend in comparison to other 2006 samples. A single sample, initially identified as HSA in the field, falls along this low-K trend as well and is termed "low-K HSA" (fig. 7). Two quartz-rich inclusions have 73 and 76.3 weight percent SiO_2 and 2.2 to 3.0 weight percent K_2O, which is much higher than other Augustine samples.

Major- and trace-element abundances in 2006 samples plot along linear trends on silica variation diagrams, except for inclusions and the low-K HSA sample (figs. 8, 9). For example, the R-squared value of a linear fit to the K_2O versus SiO_2 plot shown in fig. 7 is 0.99. Slight deviations from the linear trend exist at the mafic end in MgO and especially Cr. In Cr, the linear array appears to split from the most mafic LSAS towards increasing silica. Cr values for the majority of LSAS and about half of DLSA fall 10 to 20 ppm below the dominant array defined by HSA, DIA, banded, and some DLSA (fig. 9). At the silicic end, HSA samples have, for certain trace elements (for example, La and Nd), a larger and extend over a range that appears to fall outside the tight linear array formed by the rest of the 2006 rocks (fig. 9). Interestingly, the deviations appear to correlate with time

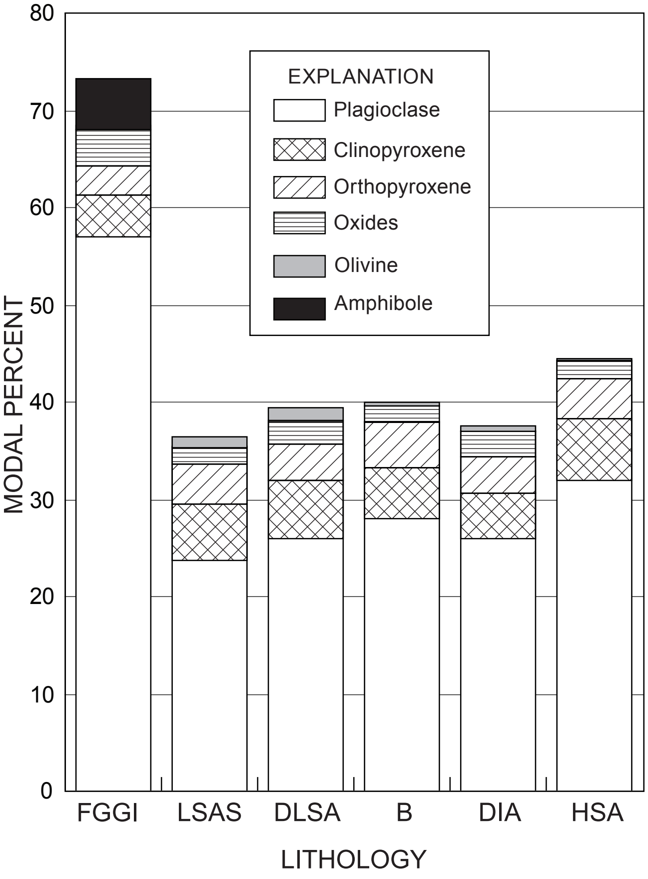

Figure 4. Modal percents of major and minor phenocryst phases in Augustine 2006 eruption deposits. HSA is high-silica andesite, DIA is dense intermediate andesite, B is banded, DLSA is dense low-silica andesite, LSAS is low-silica andesite scoria, and FGGI is fine-grained gabbroic inclusions. Modal percents are averages from point counts of at least 1,000 points per slide, normalized after removing void space counts. Groundmass percentages make up the balance to 100 percent. Oxides include all opaque minerals.

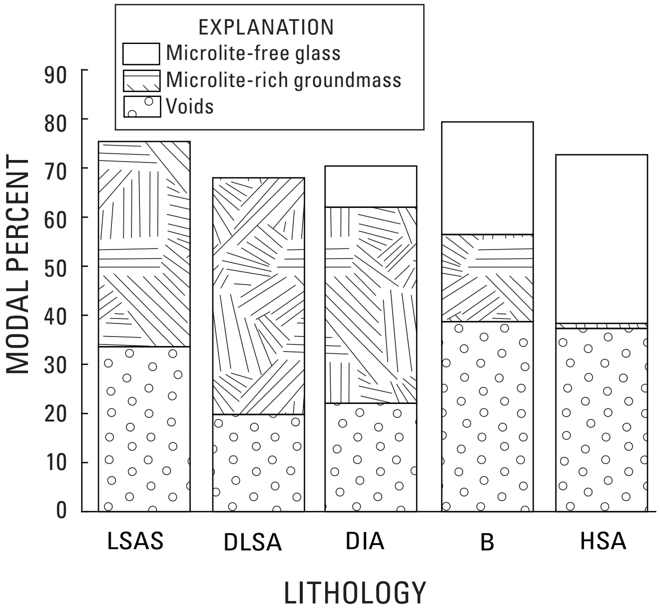

Figure 5. Average modal percentages of groundmass textures and void space (that is, vesicularity) for the five major lithologies from the Augustine 2006 eruption. Abbreviations as in figure 4.

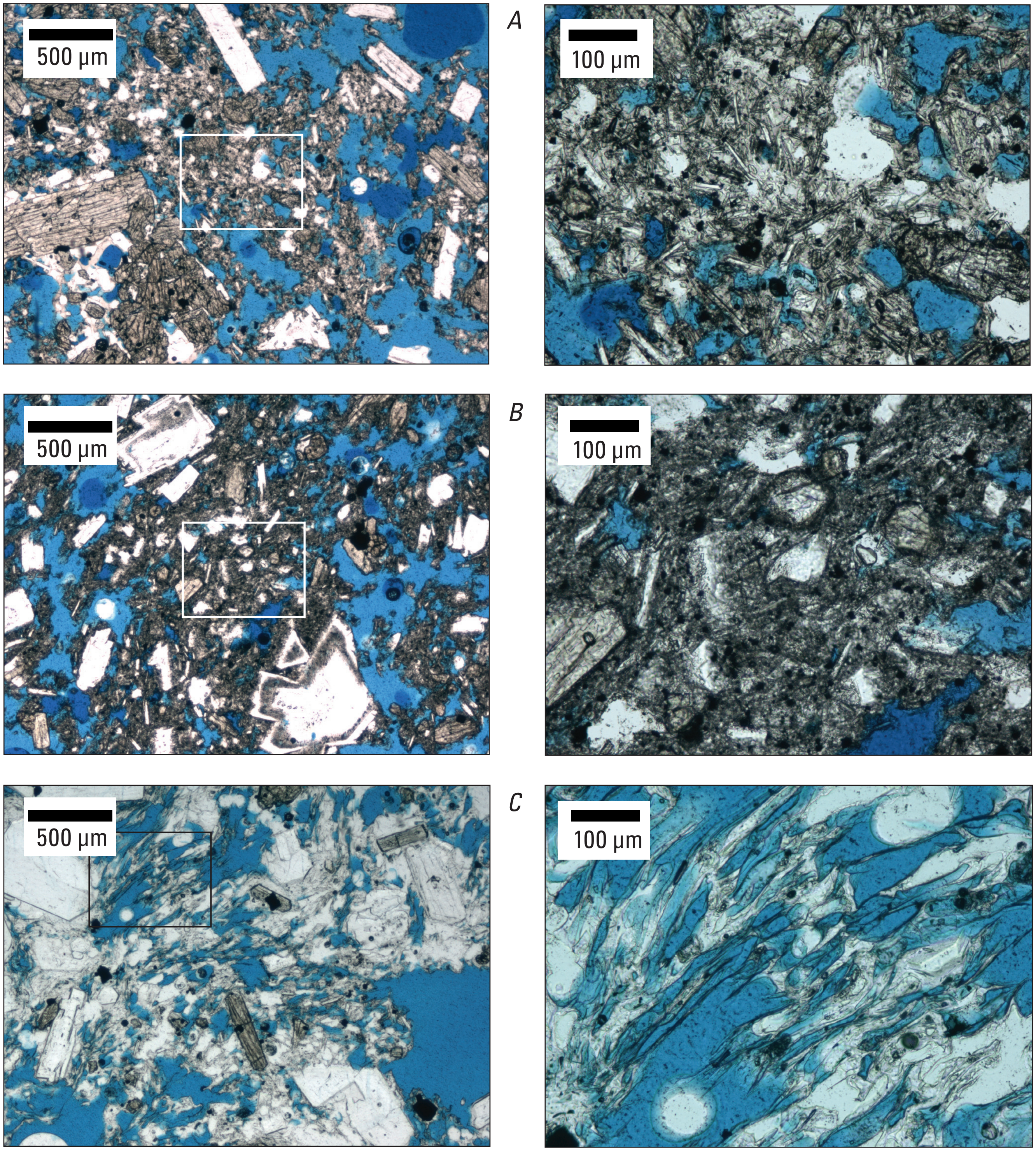

Figure 6. Transmitted-light photomicrographs showing groundmass textures of major Augustine 2006 lithologies. All samples have been impregnated with blue epoxy. Boxes in left-hand panels indicate regions that are enlarged in right-hand panels. *A,* Microlite-rich groundmass from sample 06AUMRT007b (low-silica andesite scoria) erupted during the explosive phase. *B,* Microlite-rich groundmass from sample 06AUMRT001b (dense low-silica andesite) erupted during the continuous phase. *C,* Nearly microlite-free clear glass from sample 06AUMC009p1 (high-silica andesite) erupted during the continuous phase.

of eruption: all explosive-phase low-silica andesites fall along the low-Cr trend, and all low-Nd high-silica andesites were erupted during the explosive phase.

To emphasize small trace-element differences within the 2006 ejecta suite, we have normalized their compositions to an average LSAS composition (fig. 10). This normalization scheme is preferred here because we focus on the changes across the 2006 eruption products only, rather than a broader comparison between different volcanic systems or across different tectonic settings. Normalization to the most primitive magma erupted allows us to look in greater detail at the relationships of the 2006 products to one another within the single eruption sequence. Trace element values for DLSA and LSAS samples are very similar (fig. 10*A, B*). HSA samples show elevated concentrations of large ion lithophiles (LILE), the U, Th, Pb group, and HFSE (Zr, Hf, Nb, Ta) and lower concentrations of compatible trace metals relative to the LSA samples. HREE (Eu through Lu) concentrations in the HSA are similar to those of LSAS and DLSA samples, whereas LREE (La through Sm) show a progressively greater enrichment with decreasing atomic number (fig. 10*C*). DIA and banded trace-element concentrations span a range bracketed by HSA and LSA (fig. 10*D*). Lower silica gabbroic inclusions show marginally higher concentrations of MREE and lower concentrations of LILE, HFSE, and Th, U, and Pb compared with LSA and HSA samples (fig. 10*E*). Gabbroic inclusions are also unusual in their lower concentrations of transition metals, despite their lower SiO_2 content. Two silicic inclusions are off the predominant range, and have very high concentrations of MREE, HREE, and some (but not all) of the LILE.

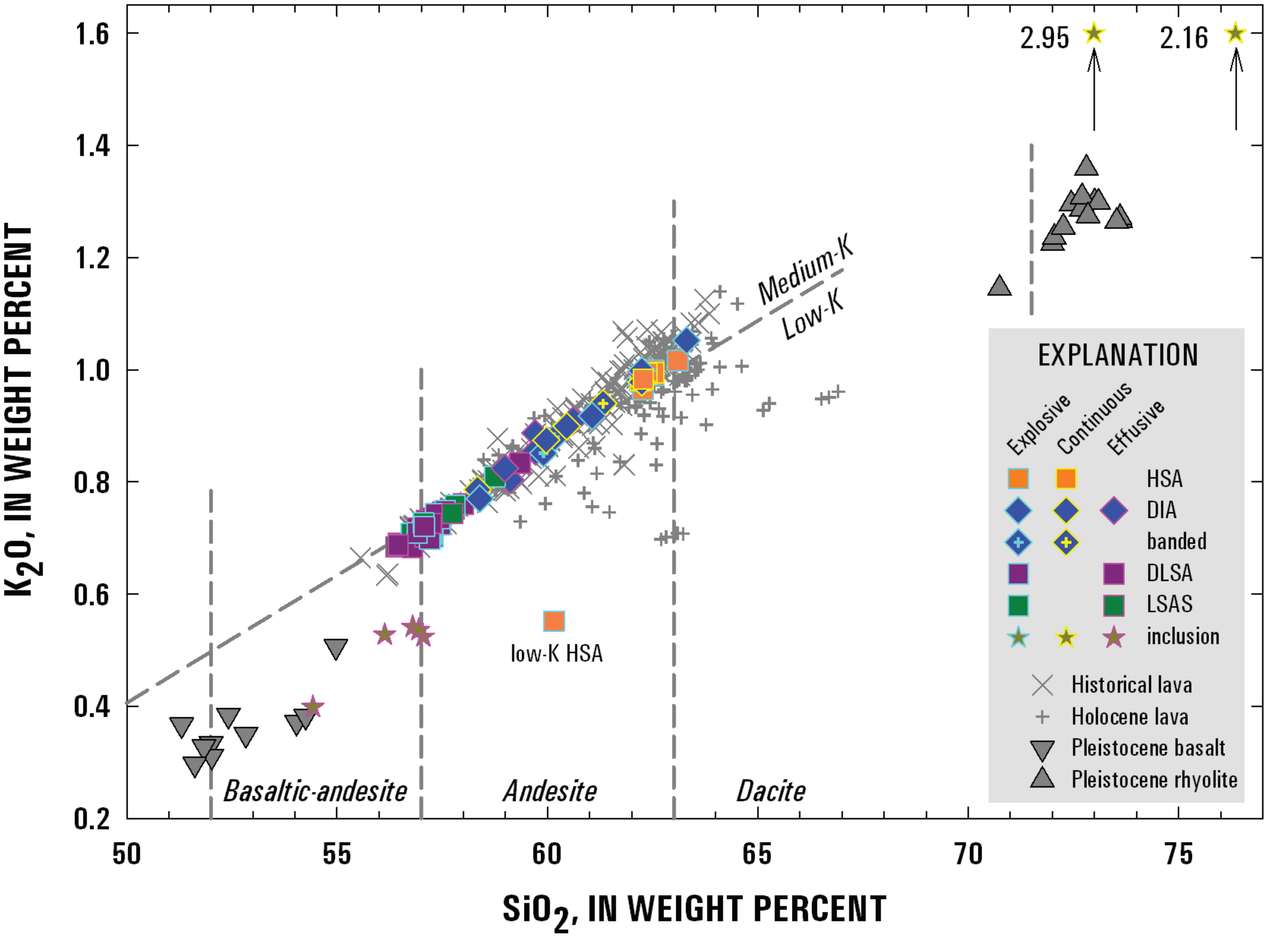

Figure 7. K_2O-silica variation diagram of Augustine whole-rock samples from Pleistocene to present. All 2006 data, and some of the pre-2006 historical, Holocene, Pleistocene basaltic rock, and Pleistocene rhyolite data are from this study; additional data are from Roman and others (2005), Daley (1986), Johnson and others (1996), C. Gardner (unpublished), C. Nye and J. Begét (unpublished), and K. Wallace (unpublished). Diagonal line shows boundary between low-K and medium-K andesites of Gill (1981). Vertical compositional boundaries from LeMaitre (1991).

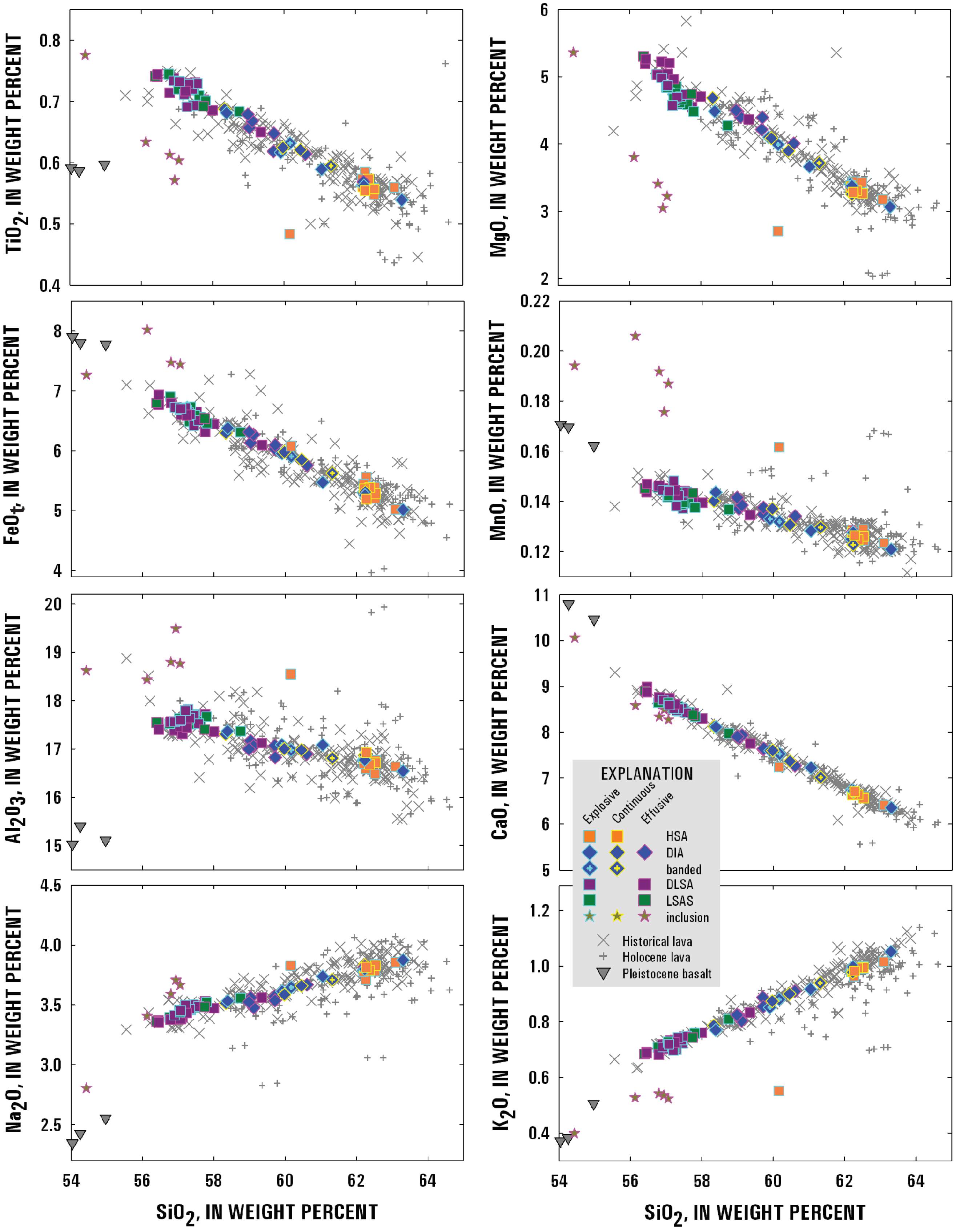

Figure 8. Major-element silica variation diagrams for Augustine 2006 samples (excluding quartz-rich inclusions). Data sources for pre-2006 samples are the same as for figure 7. FeO_t is total iron analyzed as FeO.

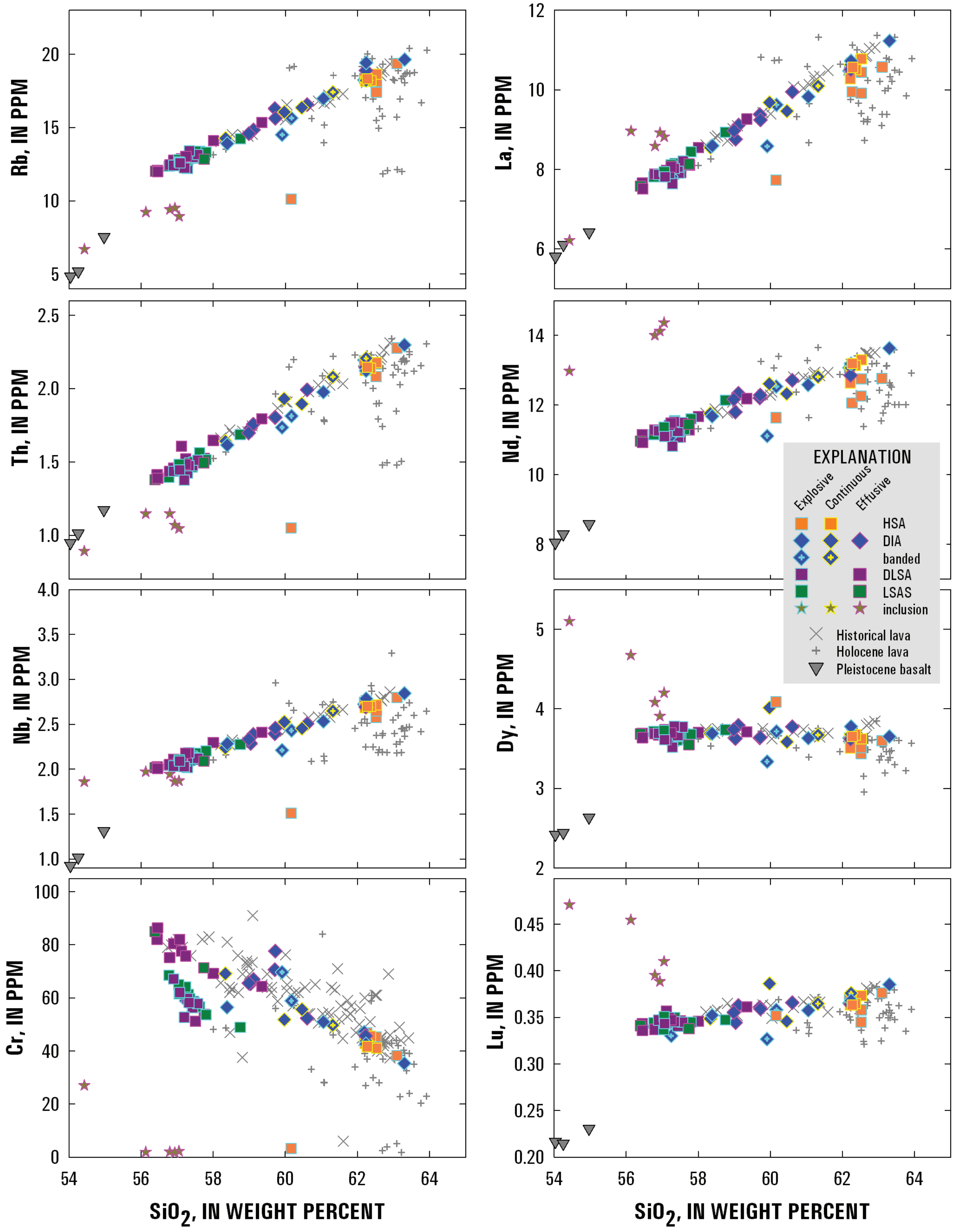

Figure 9. Trace-element silica variation diagrams for 2006 samples (excluding quartz-rich inclusions). Data sources for pre-2006 samples are the same as for figure 7.

Compositional Trends, Pleistocene to Present

The overwhelming majority of all analyzed samples from Augustine span 56 to 64 weight percent SiO_2, similar to the range of compositions produced in 2006 (fig. 7). Eruption products from 2006 yield trends on major and trace-element variation diagrams that broadly overlap those shown by products of Holocene and especially historical eruptions of the volcano, though 2006 samples are less dispersed about the linear trend than those erupted before 2006 (figs. 7 to 9).

In comparison with the 2006 eruptive products, other samples from historical eruptions are similar (figs. 7 to 9), yet tend to be slightly elevated in K_2O and Na_2O, especially at the high-silica end. Late Holocene (prehistoric) samples have compositions that are broadly similar to historical lavas, yet they extend to significantly lower middle and heavy REE abundances (fig. 10*F*).

The only known Augustine products to fall outside the basaltic-andesite-to-dacite spectrum are from the only Pleistocene outcrop on the island, which exposes rhyolitic pumice (71 to 74 weight percent SiO_2) and basaltic hyaloclastite (51 to 55 weight percent SiO_2), apparently erupted coevally (Plank and others, 2006; Waitt, this volume). Both mafic and silicic samples from this deposit fall along a lower K_2O trend than those from Holocene Augustine eruptions (fig. 7). Compared to typical Augustine products, the Pleistocene basalts have lower concentrations of all REE, LILE, and HFSE (fig. 10*F*). The rhyolites are higher in LILE, LREE, U, Th, and Pb, but their concentrations of MREE and HREE are dramatically lower than the andesites and are about as low as seen in the coerupted basalts.

Phase Descriptions and Compositions

Here we present an overview of the main phases found within rocks from the 2006 eruption. Phase compositions are illustrated in plots, and representative analyses are given in tables 3 to 6. The complete datasets for olivine, oxides, and pyroxenes are given in Tilman (2008). The full glass and plagioclase datasets are presented in electronic supplementary appendix 3 and 4, respectively.

Groundmass Glass

We analyzed matrix (groundmass) glass from most lithologies found within pyroclastic and lava flow deposits, as well as in tephra samples from January 13, 14 and 17 and the 1986 eruption (table 4; fig. 11). The high concentrations of plagioclase, pyroxene, and oxide microlites in the groundmasses, especially of the more mafic samples, made glass analysis difficult. During probe sessions, we identified glass pools within microlite-rich samples using a combination of backscattered electron images (BSE) and reflected light, but the results of some analyses indicate that the beam was at least partially on crystal(s) in addition to glass. Clearly anomalous analyses were deleted from the dataset presented here, though some analytical scatter is still likely the result of the electron beam hitting other phases. In contrast to the microlite-rich low-silica andesites, the groundmass of more silicic lithologies, comprising glass in the HSA pumice and lighter bands in banded clasts, is relatively microlite-poor, making it easier to find clean glass to analyze. This contrast resulted in an overrepresentation of silicic samples within our groundmass-glass dataset.

The entire glass dataset spans a range of SiO_2 contents from 66 to nearly 80 weight percent; matrix glasses from tephra and flow-deposit clasts span a similar range (fig. 11). All groundmass glass analyses represent melt that has evolved significantly away from the bulk rock compositions, reflecting the relatively crystal-rich nature of the 2006 eruption products. Within this range, however, the groundmass glass compositions show more than one simple trend, as a function of lithology and timing of deposition.

On an SiO_2-K_2O variation diagram, low-silica andesite scoria glasses from the explosive phase form a linear but discontinuous trend that includes dacitic (66 to 73 weight percent SiO_2) and rhyolitic (76 to 78 weight percent SiO_2) compositions (fig. 11). These glasses show a trend of steadily increasing K_2O with SiO_2, from ~1.5 to 3.0 weight percent K_2O between 66 and 78 weight percent SiO_2. Although "normal" groundmass glass within the low-silica andesite clasts shows a gap between 74 and 76.6 weight percent SiO_2, glass pools from within a plagioclase-rich clot in the LSAS span this range and fall along the same trend as other LSAS glasses. Dense low-silica andesite clasts have glass compositions similar to the low-silica end of the LSAS range.

Glasses from HSA clasts and the lighter portions of banded clasts all form a tight cluster on variation diagrams, with most of these glasses ranging from 74 to 77 weight percent SiO_2. Interestingly, these glasses have 1.5 to 2.6 weight percent K_2O, and fall slightly below the trend found in the low-silica andesite groundmass glass analyses (fig. 11). For other oxides, higher silica clasts generally fall along the same trend as the lower silica lithologies (not shown). The compositions of this group of samples do not vary with eruptive phase (table 4).

The few glass analyses from dense intermediate andesite clasts either fall into the low-silica end of the LSAS trend or in the HSA-dominated cluster.

The single low-K HSA clast contains rhyolitic glass with correspondingly low K_2O, from 1.1 to 1.6 weight percent (fig. 11). This sample also has the most silica-rich glasses analyzed, ranging from 76.7 to 79.7 weight percent. These glasses are not obviously different from other 2006 glasses in the abundances of other oxides. Groundmass glass from two fine-grained gabbroic inclusions trend toward these low values of K_2O, and partially overlap with HSA glasses (fig. 11).

Glass analyses from a distal tephra sample collected from an early explosion on January 13, 2006, follow the same trend as LSAS clasts. Lapilli clast samples from proximal tephras emplaced on January 13 through 17 were sorted according to lithologies assigned to flow samples (Wallace and others, this volume); glasses from these clasts fall along the same compositional trends as those from flow-deposit clasts (appendix 4).

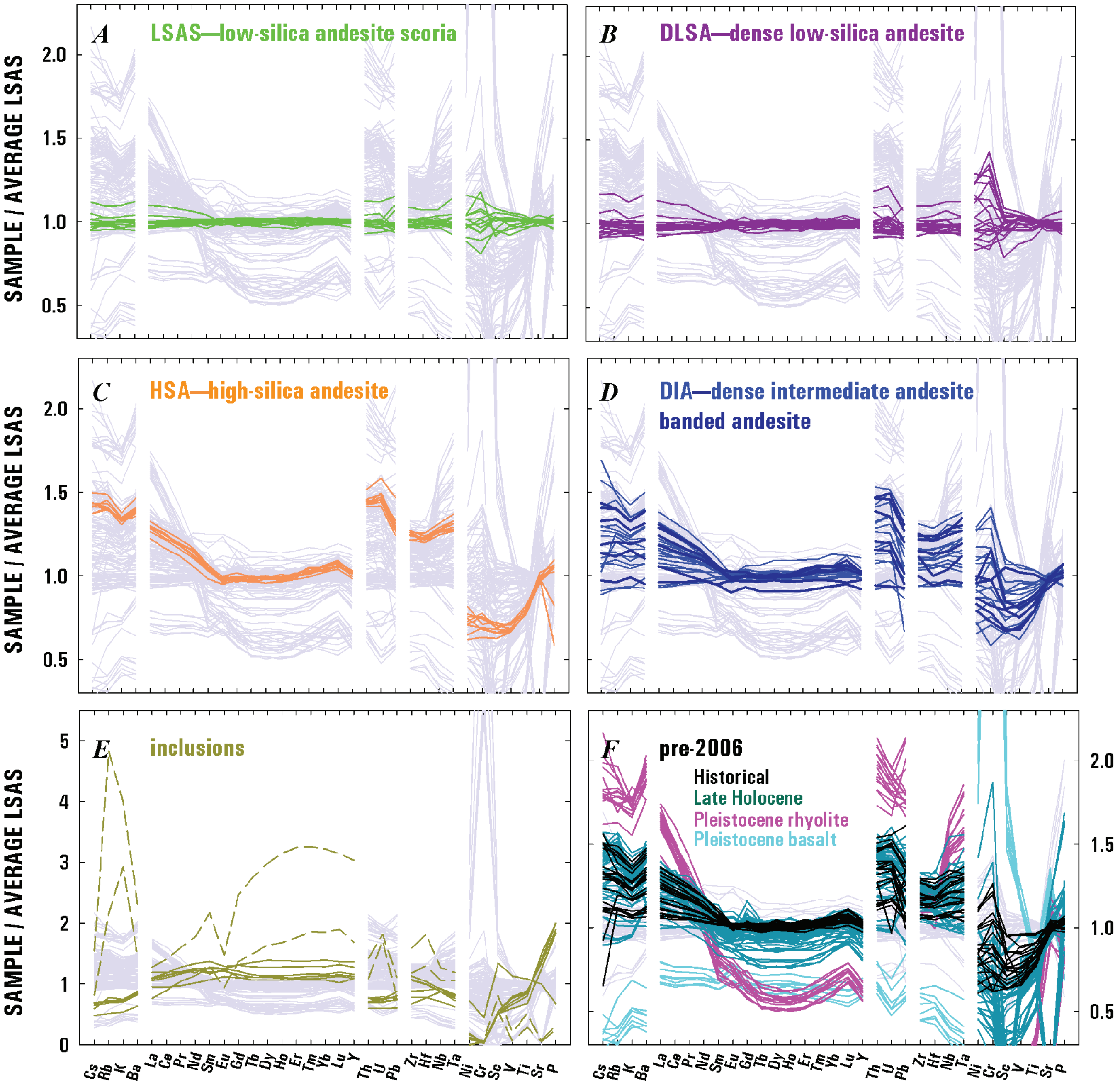

Figure 10. Incompatible-element variation diagrams showing trace-element abundances for 2006 and pre-2006 Augustine samples, normalized to the average composition of 2006 low-silica andesite scoria. Thin gray lines show the entire suite of measurements, and the colored lines in each panel show data highlighted for individual lithologies and ages. *A*, Low-silica andesite scoria. *B*, Dense low-silica andesite. *C*, High-silica andesite. *D*, Dense intermediate andesite and banded. *E*, Fine-grained gabbroic inclusions and low-K high-silica andesite (solid lines), and quartz-rich inclusions (dashed lines). *F*, Pre-2006 Augustine samples. Data are from this study, C. Nye and J. Begét (unpublished), and K. Wallace (unpublished).

Plagioclase

Plagioclase is the dominant mineral phase in the major lithologies with 24 to 32 volume percent phenocrysts and as much as 47 volume percent microlites in the groundmass (fig. 4; table 2). Phenocrysts are generally euhedral and tabular and range from 0.2 to 8.0 mm in size. In contrast, fine-grained gabbroic inclusions contain as much as 64 volume percent plagioclase. The FGGI phenocrysts have coarsely sieved interiors, showing extensive dissolution.

Five distinctive types of plagioclase phenocrysts are recognized in the major lithologies of the 2006 Augustine eruption on the basis of texture and composition. Type 1 plagioclases are texturally homogeneous, oscillatory zoned, have subtle compositional variations (fig. 12*A*), and are almost exclusively found within high-silica andesite pumices. They are optically clear with rare subtle dissolution surfaces, and contain almost no glass and mineral inclusions. Electron probe microanalysis (EPMA) profiles show fine oscillations superimposed on a weakly reverse compositional trend from An_{48} in the cores to An_{54} at the rims (fig. 12*A*). Type 2 plagioclases are oscillatory-zoned, with as much as 20 mole percent anorthite compositional variations across the zones (fig. 12*B*). Despite textural similarity to Type 1, Type 2 phenocrysts are characterized by larger chemical variations. Their EPMA profiles show abrupt jumps in An content corresponding to calcic zones at major dissolution surfaces. Each jump shows the same asymmetrical rim-ward pattern: an An_{48-54} plateau truncated by a dissolution surface, a sudden increase in An content as much as 80 mole percent, and a gradual return to the An_{48-54} plateau. Isolated glass inclusions and acicular microlites of ortho- and clinopyroxene are also abundant near dissolution surfaces. Large phenocrysts usually contain 2-3 major dissolution surfaces and associated jumps in An content. Type 2 plagioclases are present in all lithologies, although they are more common in high-silica andesite as compared to more mafic products of the 2006 eruption. Type 3 plagioclases are sub- to anhedral and are made up of oscillatory-zoned cores, surrounded by An_{70-90} rims with a distinctive texture formed by a network of profuse, interconnected inclusions of glass and microlites, commonly referred to as resorption rims, sieved texture, or “dusty zones” (Browne and others, 2006; Nakamura and Shimikata, 1998; Tsuchiyama, 1985). Type 3 cores are typically similar to those of Types 1 and 2, though larger Type 3 crystals may have more calcic cores. The resorption rims have the same principle characteristics as the calcic zones in Type 2 plagioclases, but they have higher An content (as much as 90 mole percent), more inclusions and are greater in width (fig. 12*C*). The proportions of glass and mineral inclusions in the resorption rims decrease conspicuously toward the boundary with the groundmass. Interestingly, glass inclusions

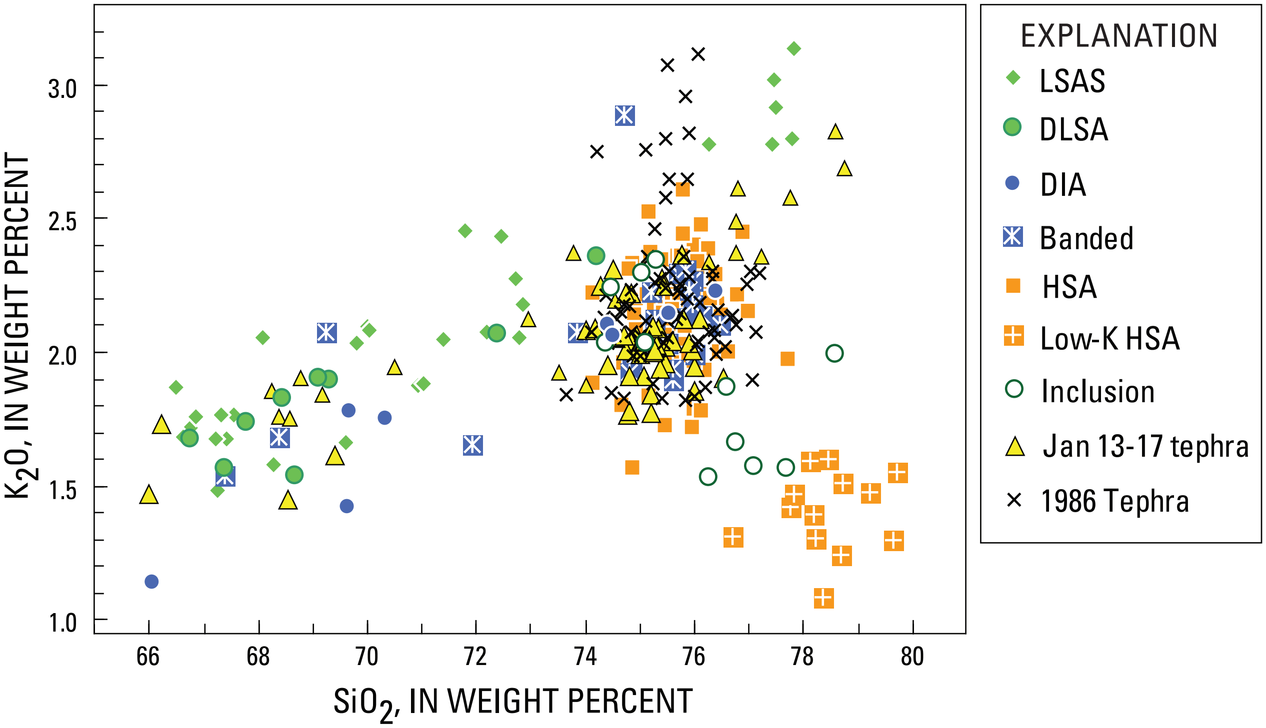

Figure 11. Groundmass-glass analyses from the Augustine 2006 lithologies, compared with select analyses from 2006 tephra fall deposits from the January 13–14 and January 17 explosions. Also plotted for comparison are analyses from 1986 tephras (P. Izbekov, unpublished data).

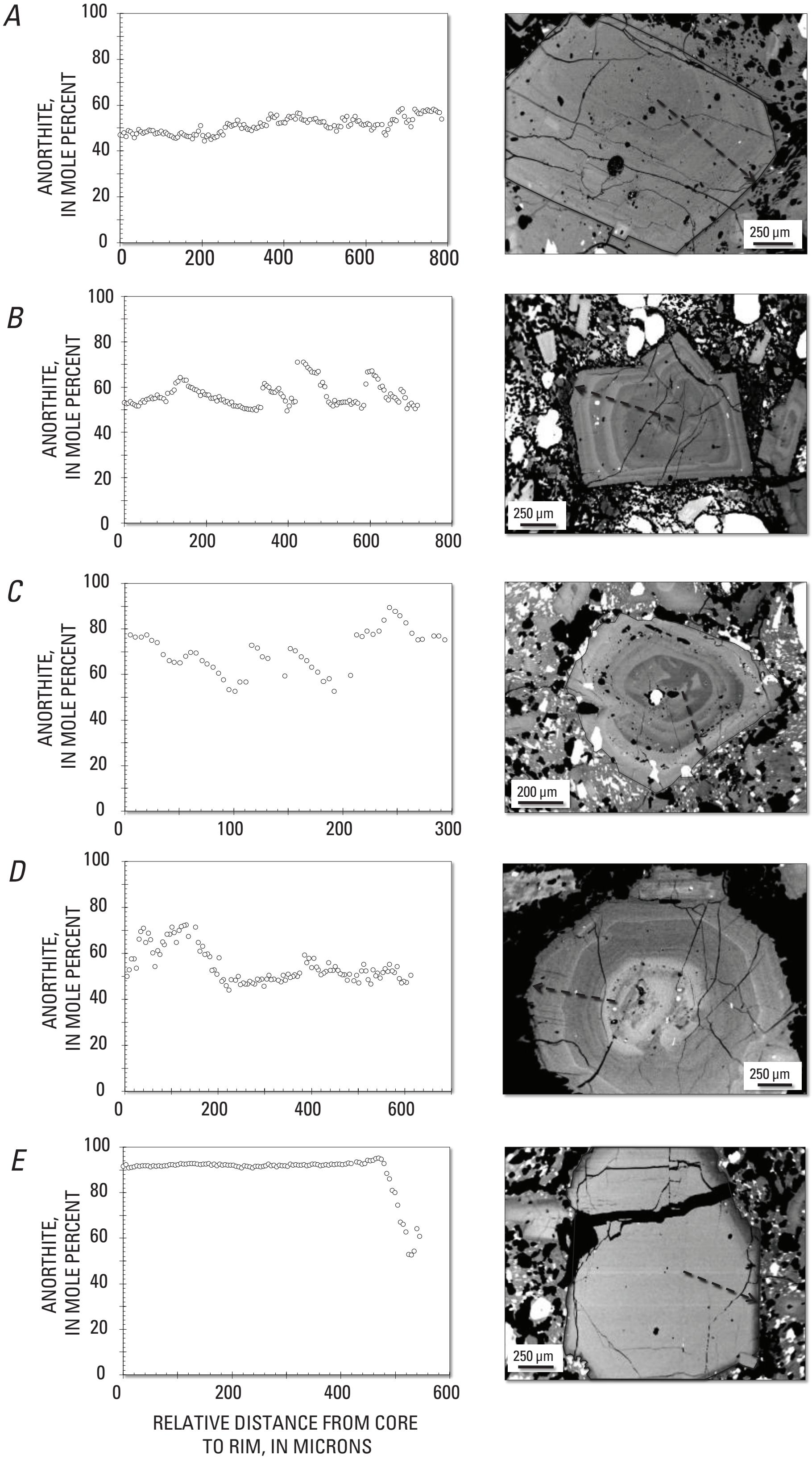

Figure 12. Back-scattered electron (BSE) images and corresponding profiles showing anorthite content of five major plagioclase phenocryst types identified in 2006 eruption deposits.

in the resorption rims are often vesicular. Type 3 plagioclases are present in all lithologies, although in high-silica andesite the resorption rim is surrounded by an oscillatory-zoned rim 10-150 microns wide, whereas in low-silica andesites the resorption rim contacts groundmass, with An$_{65-75}$ composition at the contact. Type 4 plagioclases are compositionally and texturally heterogeneous, with calcic cores surrounded by oscillatory-zoned rims (fig. 12*D*). The cores commonly contain inclusions of glass and microlites, as well as patches of An$_{48-54}$ plagioclase. The composition of cores reaches An$_{90}$ and overlaps with the composition of resorption rims in Type 3 plagioclases. Type 4 plagioclase crystals have oscillatory rims that overlap in composition with Type 1 phenocrysts. Type 4 plagioclases are found predominantly in high-silica andesite. Type 5 plagioclase phenocrysts consist of euhedral, compositionally and texturally homogeneous An$_{92-94}$ cores surrounded by oscillatory-zoned rims (fig. 12*E*). Type 5 plagioclases are rare, but found in all lithologies. Widths of the outermost oscillatory-zoned rims in high-silica andesites often exceed 150 to 200 micron, whereas in low-silica andesites they are significantly narrower (20–30 microns).

All major lithologies are characterized by similar ranges of phenocryst compositions of An$_{45-90}$, with a primary mode at ~An$_{54}$ (fig. 13). The second mode at >90 mole percent in compositions of DLSA phenocrysts is due to the large number of Type 5 plagioclase analyses (fig. 13*D*). Plagioclase microlites have the same composition as the outermost rims of phenocrysts in all lithologies. Composition of microlites in HSA and DIA are nearly the same (An$_{50-54}$ and An$_{50-55}$, respectively) and overlap with the composition of the Type 1 phenocrysts. Compositions of microlites in LSAS and DLSA are An$_{57-73}$ and An$_{64-77}$, respectively, which both overlap considerably with the composition of calcic zones in Type 2 plagioclases, as well as of resorption rims in Type 3 plagioclases. Textural and compositional characteristics of plagioclases from products of the 2006 eruption are the same as those in products of 1964, 1976, and 1986 eruptions. For example, Type 2 oscillatory-zoned plagioclases from all four eruptions show impressive similarity of their EPMA profiles characterized by the “plateau” composition at An$_{48-54}$ (fig. 14).

Pyroxenes

Although both are present in all lithologies, clinopyroxene (average 5.6 volume percent) is slightly more abundant than orthopyroxene (4.7 volume percent on average; fig. 4, table 2). Pyroxene phenocrysts are generally unzoned, although orthopyroxene is often rimmed with clinopyroxene, which is particularly common in LSA lithologies. Orthopyroxene phenocrysts from all lithologies have an average composition of Wo$_2$En$_{65}$Fs$_{32}$ (fig. 15, table 5). High-Ca pyroxene phenocrysts are predominantly augite to diopside, with an average composition Wo$_{44}$En$_{41}$Fs$_{14}$. Pyroxene phenocrysts are typically tabular and less than 1 mm in length, but some phenocrysts as large as 5 mm were observed, especially in low-silica andesites.

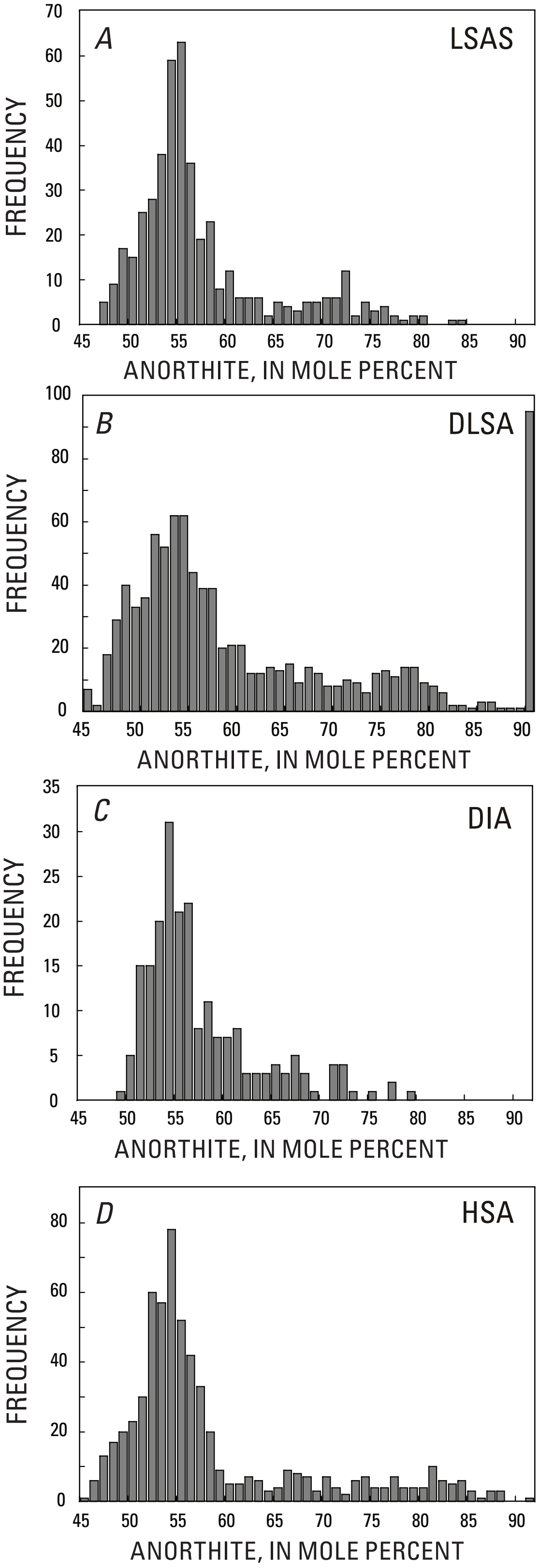

Figure 13. Histograms showing frequency versus anorthite content for spot analyses on plagioclase phenocrysts from the four major lithologies in 2006 eruption deposits. Abbreviations as in figure 4.

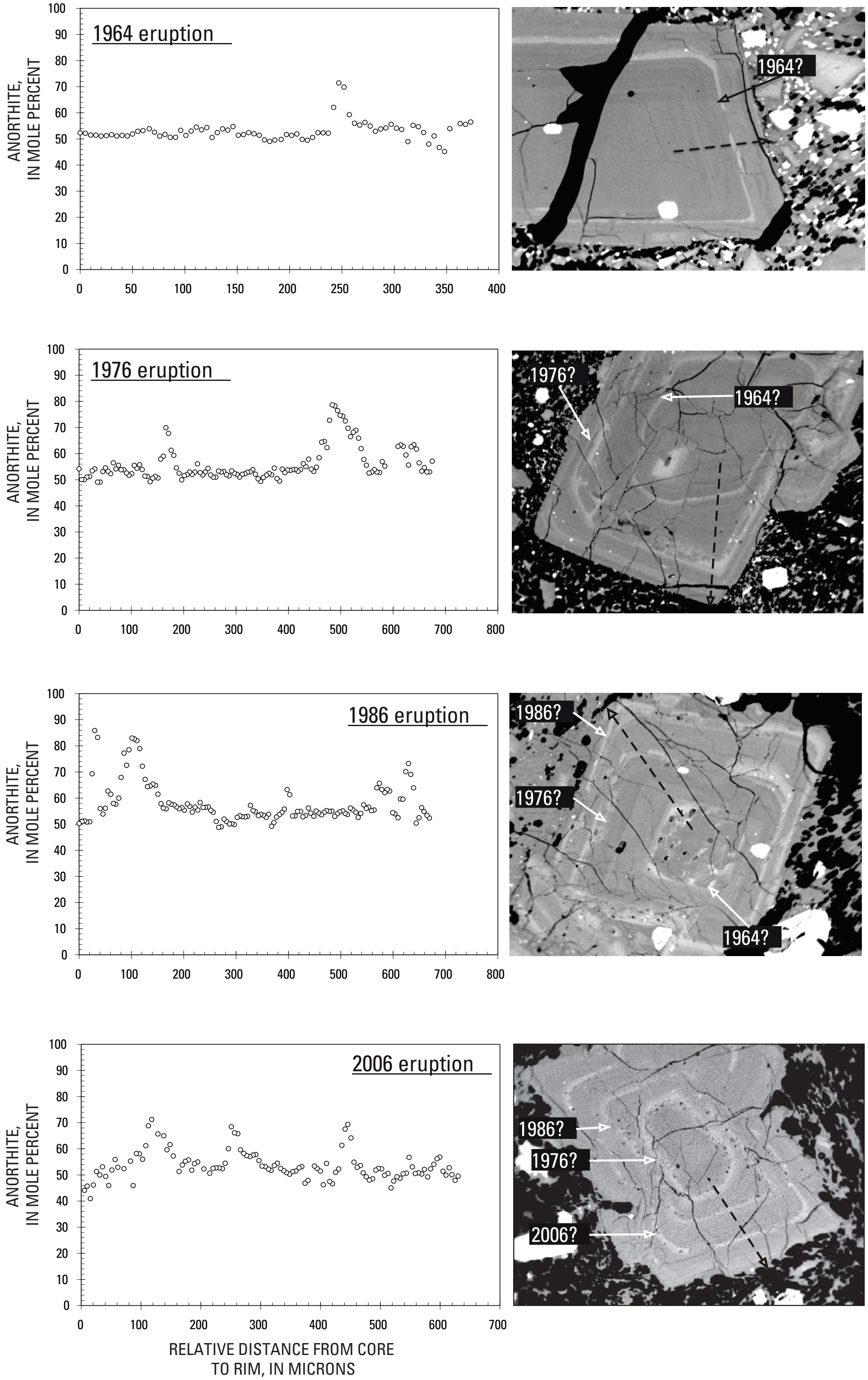

Figure 14. Back-scattered electron (BSE) images and anorthite-content profiles for representative plagioclase phenocrysts from the last four Augustine eruptions.

Orthopyroxene and clinopyroxene are both present in the 2006 deposits as microlites in the groundmass, and orthopyroxene is found in reaction rims on olivine. The compositions of the groundmass and rim pyroxenes are the same as the phenocrysts (fig. 15). Mg numbers range from 0.67 to 0.74 for orthopyroxene and 0.73 to 0.85 for clinopyroxene.

Fe-Ti Oxides and Geothermometry

All lithologies contain Fe-Ti oxides both in the groundmass and as inclusions in phenocrysts and reaction rims. Chromite is also present as inclusions in olivine phenocrysts. Fe-Ti oxides in the groundmass are commonly euhedral, less than 30 microns in width, and the pairs analyzed for this study are unzoned; often ilmenite and magnetite are present as touching pairs (fig. 16). Oxides present as inclusions in other minerals are almost always anhedral and are as large as 1 mm. DLSA clasts contain predominantly titanomagnetite, which often exhibits ilmenite exsolution lamellae. Ilmenite phenocrysts are rare in this lithology. The other lithologies also contain predominantly titanomagnetite, yet have more abundant ilmenite than DLSA.

Touching pairs in grain mounts used for geothermometry were groundmass grains as opposed to anhedral grains found as mineral inclusions. The f_{O_2} recorded by oxide pairs in 2006 Augustine magmas is approximately 2 log units above the Ni-NiO buffer (NNO), roughly equivalent to the rhenium-rhenium oxide (RRO) buffer (fig. 17). In investigating Mount Pinatubo magma, Rutherford and Devine (1996) experimentally confirmed that the QUILF algorithm overestimates temperatures by 30±5°C in magma with f_{O_2} near RRO

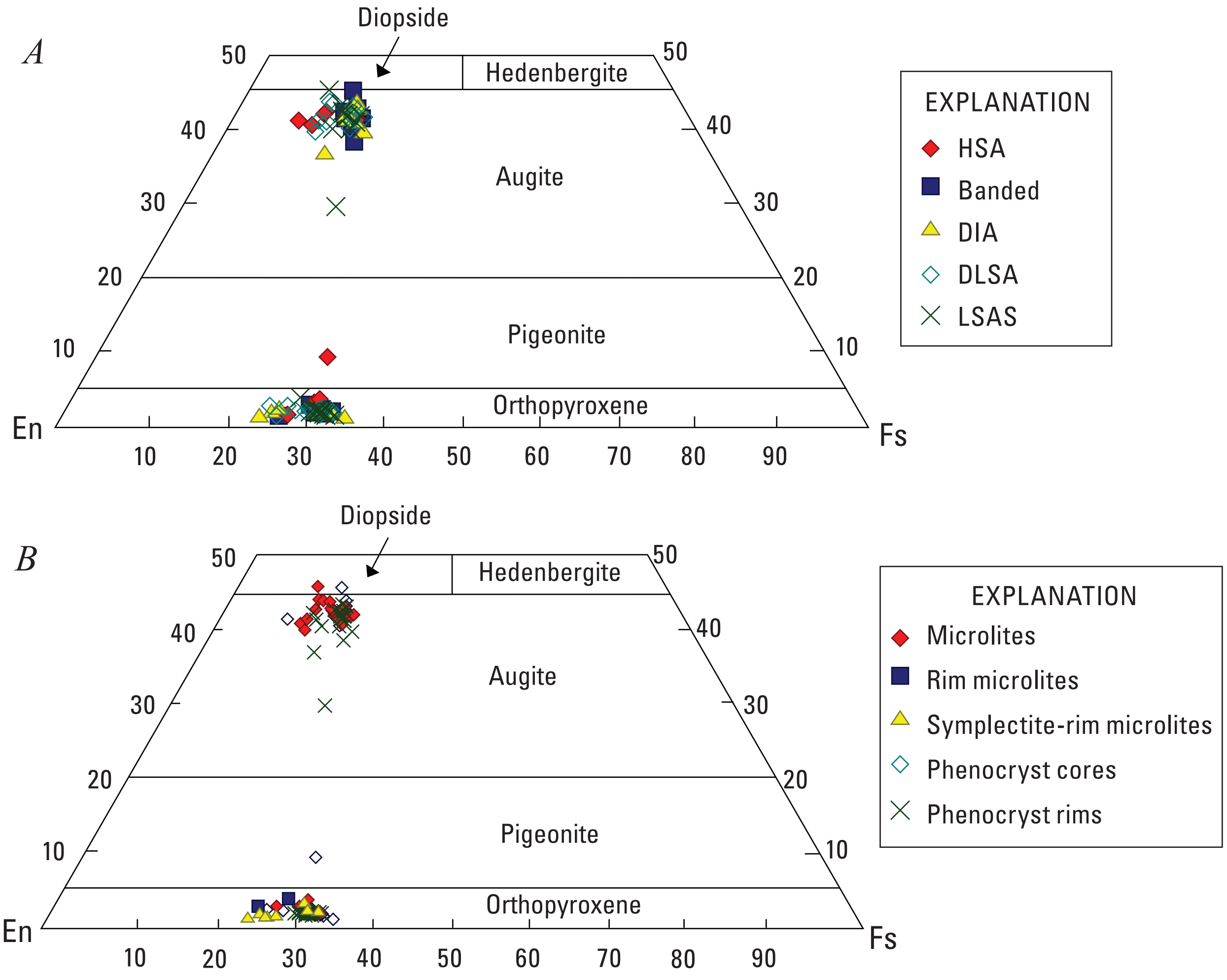

Figure 15. Classification diagram for pyroxene phenocrysts and microlites from the 2006 Augustine eruption. The apices of the ternary diagram represent 100 mol % of each pyroxene component as follows: En-enstatite, Fs-ferrosilite, and the top apex (not shown) represents wollastonite (Wo). Symbols represent single point analyses from rim and core of individual phenocrysts. Abbreviation of lithologic types as in figure 4: *A*, Pyroxenes sorted by lithology. *B*, Pyroxenes sorted by type. Rim pyroxene indicates pyroxenes found in the pyroxene-rimmed olivines. Symplectite pyroxene indicates pyroxenes found either in a symplectic olivine reaction rim or a symplectic pseudomorph.

because this is outside the limits of the calibration of Andersen and others (1993). Calculating the temperatures using other geothermometer algorithms (for example, Ghiorso and Evans, 2008), regardless of the method used to estimate the mol fractions of ulvospinel and ilmenite (for example, Stormer, 1983), all result in overestimations of the temperature, relative to the findings of Rutherford and Devine (1996). Thus, the temperature estimates included here have been decreased by 30°C from the original QUILF estimate.

Results using the QUILF algorithm (Andersen and others, 1993) indicate that LSAS was erupted at temperatures from 825 to 968°C (average of 904°C, one standard deviation of 47°C, n = 12) and HSA from 811 to 868°C (average of 838°C, one standard deviation of 14°C, n = 20; table 6 and fig. 17). Oxide pairs from banded and DIA clasts yield temperatures from 819 to 840°C and 829 to 853°C, respectively. A single oxide pair from a dense low-silica andesite sample yielded a temperature of 920°C. Oxide temperatures are consistent within each lithology type, but the HSA, banded, and DIA show a narrower range of temperatures, which are generally lower than those estimated for the low-silica andesites.

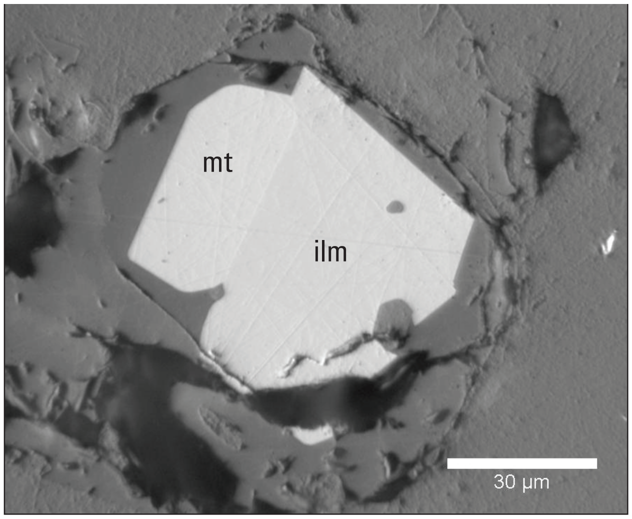

Figure 16. Back-scattered electron image of touching magnetite-ilmenite pair separated from groundmass of high-silica andesite sample 06AUMLC004c1.

Olivine

Olivine phenocrysts are present in all lithologies but are most abundant in the low-silica andesites, with 1.3 volume percent in DLSA and 1.0 volume percent in LSAS samples (fig. 4; table 2).

There are four main textural variations in the olivine phenocrysts. Type 1 are sub–to euhedral phenocrysts with no reaction rims (fig. 18*A*). They have core compositions that average 84 mole percent forsterite component (Fo_{84}) and are unzoned except for 5-10 micron, Fe-enriched (Fo_{73}) rims (table 7).

Type 2 olivines are sub- to anhedral phenocrysts that are resorbed and usually have thin (< 50 microns) reaction rims composed of orthopyroxene microlites (fig. 18*B*). Type 2 olivines are generally unzoned and have an average composition of Fo_{84}.

Type 3 olivines are subhedral with rims that consist of two concentric zones (fig. 18*C*). Inner rims can be as much as 500 microns thick, but average ~100 microns, and consist of fine-grained intergrowths of orthopyroxene and magnetite, commonly called a symplectite. This portion of the rim appears opaque in transmitted light, but the intergrowth texture is clearly visible in BSE images and x-ray maps. Outer rims are 50 microns thick, on average, and consist of orthopyroxene microlites. Some symplectite pseudomorphs after olivine are also present, and these are surrounded by orthopyroxene rims (fig. 18*D*). Orthopyroxenes in all rims have an average composition of $Wo_2En_{70}Fs_{28}$ (table 5), similar to the compositions of the phenocrysts and microlites. The titanomagnetite in the symplectite rims has approximately the same FeO, Al_2O_3, MnO, and MgO content and generally less TiO_2 and more Cr_2O_3 than in the titanomagnetite phenocrysts (table 6). Large (>600 micron) Type 3 olivines are normally zoned, with core compositions of ~Fo_{84} and rim compositions of ~Fo_{74}. Smaller Type 3 olivine crystals (<300 micron) are unzoned and have compositions that average Fo_{74}. Although HSA samples have the lowest percentages of olivine, those that are present are mostly Type 3.

Type 4 olivines are characterized by hopper and swallowtail habits (fig. 18*E* and 18*F*). They are often rimmed by thin jackets of orthopyroxene and occasionally by symplectite. Type 4 olivines are generally unzoned and have an average composition of Fo_{84}. They are most common in DLSA.

Amphibole

Amphibole is rare in all major lithologies and is unevenly distributed among different samples, with several grains in some thin sections and none in others, even within a single lithology. Rare amphibole phenocrysts in the low-silica and intermediate andesites have average lengths of 350 microns, are anhedral, and are typically surrounded by fine-grained reaction rims 40 to 100 microns thick (fig. 19*A*), composed of plagioclase, orthopyroxene, and oxides. In addition, pseudomorphs of amphibole, with the same mineralogy and texture as the reaction rims, are found in these lithologies, suggesting that amphiboles were once more abundant. Amphibole phenocrysts found in HSA clasts are sub- to euhedral, rarely surrounded by reaction rims, and larger than those in the more mafic rocks, with average lengths of ~600 microns (fig. 19*B*). Fine-grained gabbroic inclusions contain the highest modal abundances of amphibole, ranging to 10 volume percent. Amphiboles in this lithology are 0.6 to 2 mm in size, subhedral to anhedral, with plentiful reentrants and melt or plagioclase inclusions (fig. 19*C*). Analysis of a handful of grains from all lithologies yields compositions that straddle divisions between edenite, pargasite, hornblende, and tschermakite (table 8).

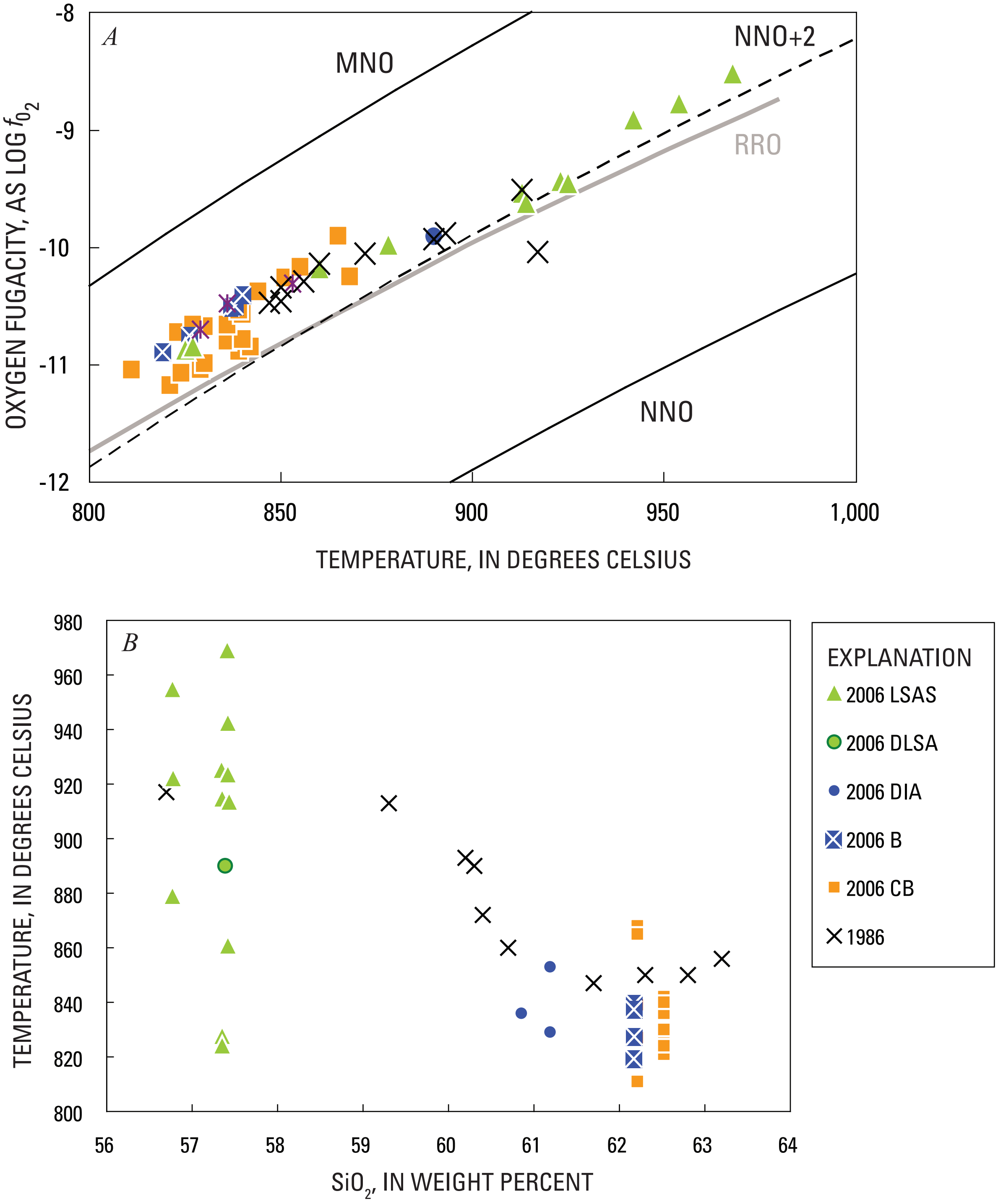

Figure 17. Temperature-composition relations of Augustine magmas and eruption products. *A*, Temperature and f_{O_2} for Augustine magmas as estimated from Fe-Ti oxide pairs. Rhenium-rhenium oxide (RRO) buffer was calculated using Pownceby and O'Neill's (1994) equation calibrated from 850-1250 K. *B*, Whole-rock SiO_2 content versus temperature. Abbreviations as in figure 4. 1986 data are taken from Roman and others (2005) and are averages of sample sets representing various rock types erupted during the explosive phase of the 1986 eruption. Temperature and oxygen fugacity for 2006 and 1986 samples calculated using QUILF (Andersen and others, 1993), with temperatures subsequently decreased by 30°C to account for overestimation at high oxygen fugacity (Rutherford and Devine, 1996).

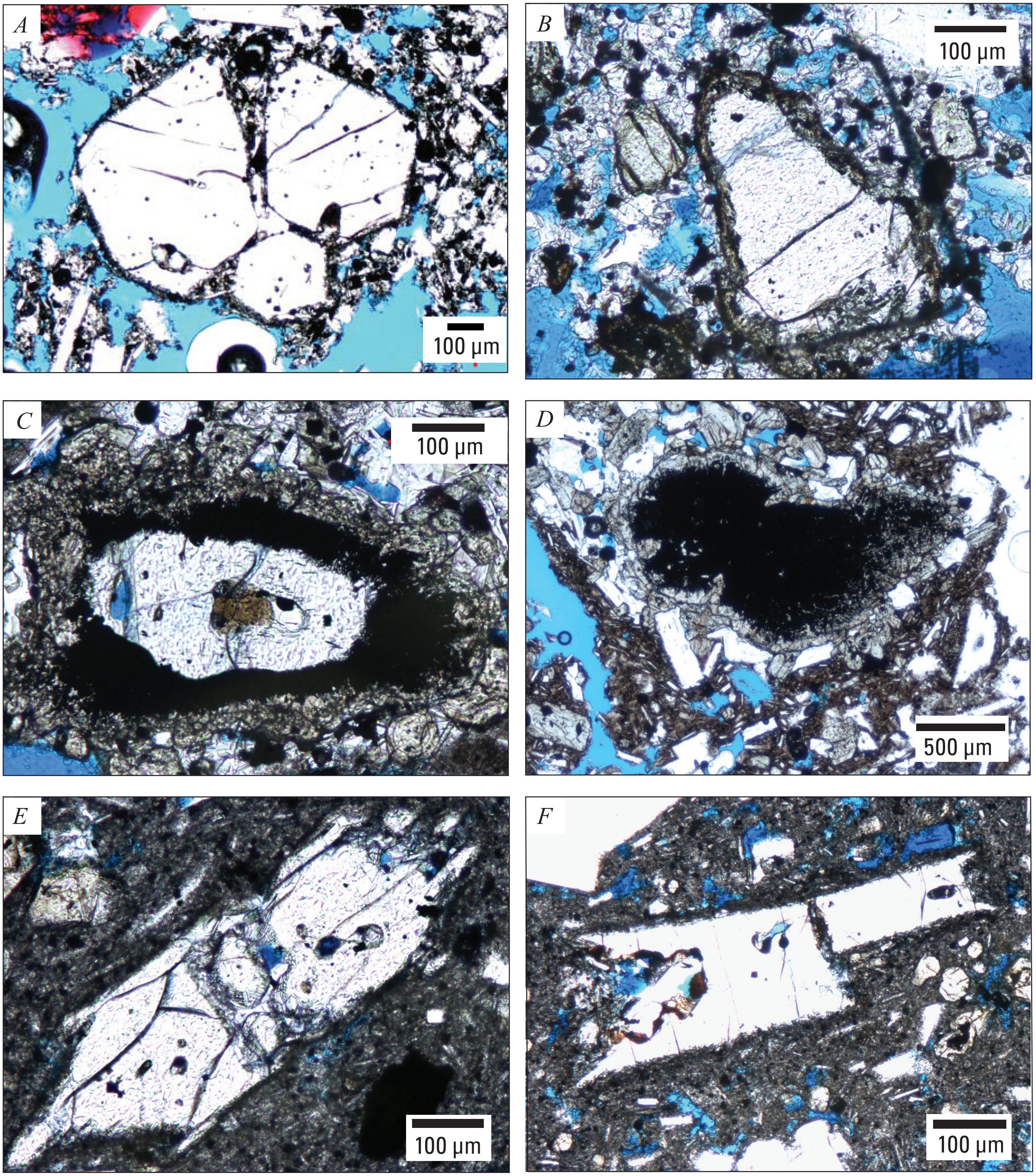

Figure 18. Olivine textures found in Augustine 2006 eruption deposits. All images are transmitted-light photomicrographs. *A*, Euhedral, unrimmed olivine from sample 06AUMC008a. *B*, Anhedral, pyroxene-rimmed olivine from sample 06AUKB002a. *C*, Symplectite-rimmed olivine from sample 06AUKB003. *D,* Symplectite olivine pseudomorph from sample 06AUMC008b.p3. *E*, Hopper olivine from sample 06AUKB003. *F,* Hopper olivine from sample 06AUMC005c.p3.

Accessory Minerals

Apatite is present throughout all lithologies, with the LSAand HSA containing greater modal abundances and the fine-grained gabbroic inclusions notably less (appendix 1). It consists of fine, needle-shaped crystals that are slightly green in plane polarized light. Crystals range in size from 6 to 200 microns and are most commonly found within larger plagioclase and clinopyroxene crystals, although some samples show fine apatite needles within the groundmass as well. Apatite inclusions are present in plagioclase with all textures, including "clean," melt-inclusion-rich, and coarsely sieved. Apatite needles in plagioclase, although not possessing a discernible orientation, preferentially occupy one or more oscillating zones within the plagioclase.

Anhydrite is a rare accessory mineral in these samples and is only found in a handful of thin sections and only within the banded, low-silica andesite scoria and fine-grained gabbroic intrusive lithologies. It is more abundant in the fine-grained gabbroic inclusions, but is still rare, with each thin section having only a couple of anhydrite crystals. Anhydrite was not found in samples collected after May 2006, but this is probably because of the extreme scarcity of anhydrite crystals and not a result of a change in crystal distribution. Primary

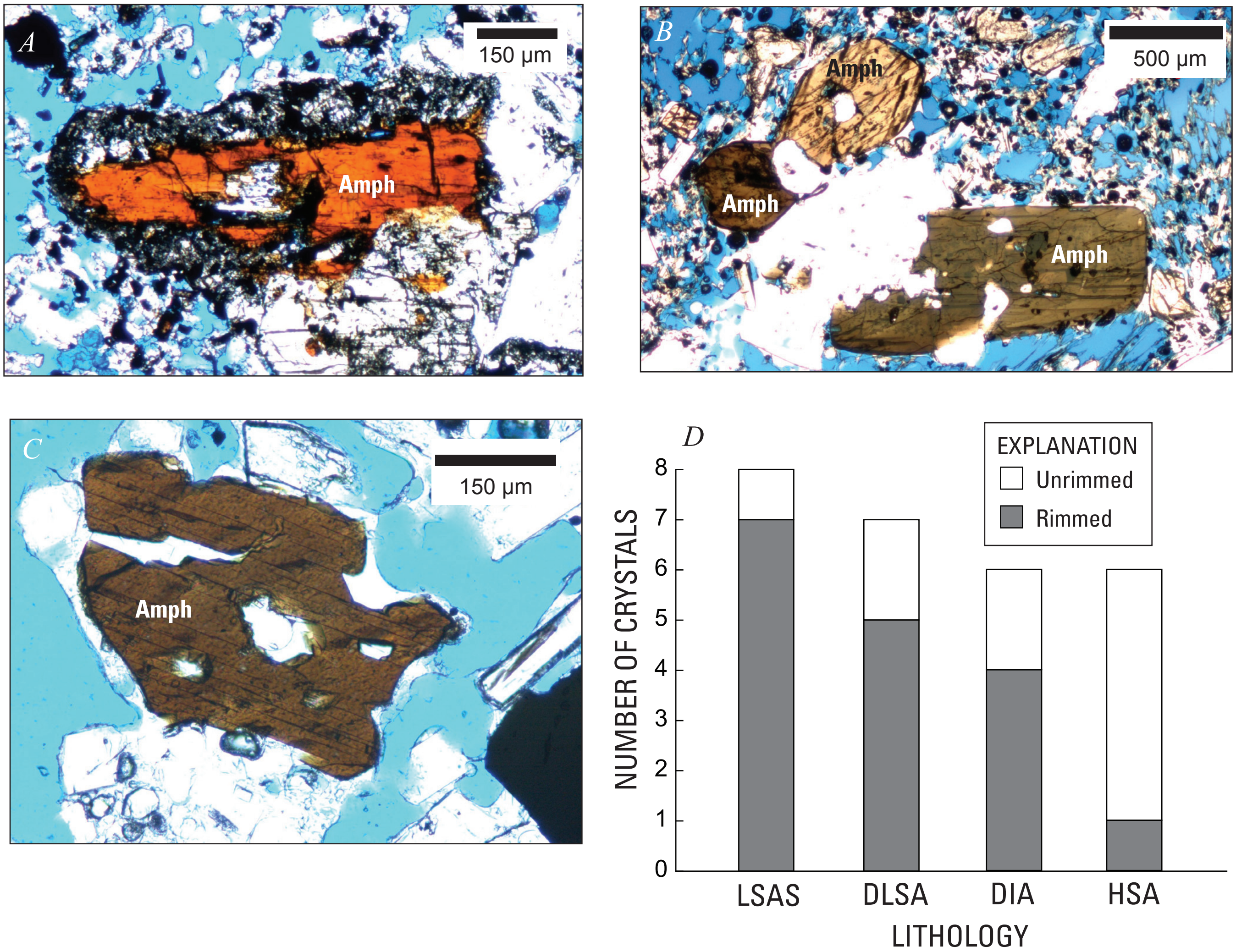

Figure 19. Transmitted-light photomicrographs and histogram of amphibole phenocrysts found in Augustine 2006 eruption deposits. *A*, Fine-grained reaction rim around amphibole phenocryst in DIA sample 06AUKB002a, collected from effusive-phase block-and-ash-flow deposit. *B*, Cluster of unrimmed, euhedral amphiboles from high-silica andesite sample 06AUMC004c, collected from Rocky Point pyroclastic-flow deposit. *C*, Resorbed phenocryst from gabbroic-inclusion sample 06AUMC013a, collected from effusive-phase block-and-ash-flow deposit. *D*, Histogram showing occurrence of rimmed and unrimmed amphibole in samples from the major lithologies of the 2006 eruption. Abbreviations are as in figure 4.

anhydrite crystals range from 200 to 600 microns long, are subrounded, and have a thin, dark-colored, fine-grained rim.

Discussion

Source and Origin of Erupted Magmas

The dominant geochemical signature of the 2006 Augustine magmas lies in the linear array of major oxides and trace elements, which is consistent with two-component magma mixing (figs. 7 to 10). The trends observed in the 2006 deposits mirror closely those observed from the historical Augustine eruptions and a significant proportion of Holocene magmas as well. The simplest explanation is that two-component mixing between the low-silica and high-silica andesites before and during the 2006 eruption creates the tight linear array in major and trace elements. However, complexities in petrogenesis of the LSA and HSA endmembers exist, and these will be discussed below.

High-Silica Andesite—Reinvigorated Resident of Shallow-Crustal Body

Several lines of evidence help place constraints on HSA storage conditions. Fe-Ti oxide geothermometry indicates that the high-silica andesite was stored at 838±14°C before eruption. Petrological results, including melt inclusion analyses (Webster and others, this volume), indicate that the HSA was stored at a depth of approximately 4 to 6 km below the surface. The presence of amphibole phenocrysts indicates that the magma resided at a depth equivalent to water pressures above amphibole stability. While the stability of amphibole has not been experimentally determined for this particular composition, we can look to other experimental studies on similar whole-rock compositions for comparison. Phase equilibrium experiments showed that amphibole was stable in the andesite (63.4 weight percent SiO_2) erupted in 1989–90 from Redoubt Volcano at pressures above 100 MPa from 850 to 875°C (Browne and Gardner, 2006). This is equivalent to depths equal to or greater than 3 to 4 km. The maximum dissolved water concentration measured in melt inclusions within high-silica andesite pyroxenes was 4 weight percent (with CO_2 below detection), equivalent to a pressure of 100 MPa (Webster and others, this volume).

Geophysical signals associated with the 2006 eruption are consistent with petrologic findings. Approximately 20 earthquakes, which occurred after the eruption in 2006 ended, were located beneath the summit at a depth of 4 km (Power and Lalla, this volume). One explanation for these post eruption events is that they occurred in response to pressure reduction after magma withdrawal and eruption from this depth. The majority of the high-silica andesite was erupted during the continuous phase, temporally coincident with a marked deflationary signal seen in the geodetic data. This signal has been modeled as being the result of a pressure decrease of a cylindrical body whose top is approximately 5 km below the surface (Cervelli and others, this volume).

It is likely that the HSA resided in this shallow-level reservoir for decades prior to eruption. The composition and phase assemblage of the 2006 high-silica andesite closely resemble those of the silicic end member of the 1976 and 1986 eruptions. For example, equilibrium plagioclase compositions in the host magma remained the same throughout the four most recent eruptions (1964, 1976, 1986, and 2006). This indicates relatively constant melt composition, temperature, and water pressure in the shallow-level host reservoir since at least 1964. For example, Type 2 oscillatory-zoned plagioclases from all four eruptions show impressive similarity of their EPMA profiles characterized by the “plateau” composition at $An_{48\text{-}54}$ (fig. 14). Increasing numbers of high-An “spikes” with each subsequent eruption suggest that some individual crystals may record multiple recharge events linked to these eruptions. Despite evidence for repeated recharge and magma mixing during each of these eruptions, the host magma has not changed significantly in composition. Also, the HSA phenocryst assemblage (table 2) shows less evidence of reaction and disequilibrium than the mixed, intermediate, and low-silica andesites. For example, fewer than than 10 percent of HSA plagioclases show visible resorption. This implies that if the shallow reservoir persists as a convecting liquid + crystal magma, then its volume must be large relative to newly arriving magma. On the other hand, if it persists as a largely solid crystal mush, then it is possible that during each eruption newly arrived magma “carves off” and mixes with only a portion of the mush.

Although the majority of chemical variations within the 2006 sample suite reflect two-component mixing, there is some deviation from the mixing trend for some trace elements, particularly the LREE. The 2006 HSA samples that diverge most from the mixing trend were erupted during the explosive phase and have LREE compositions similar to prehistoric Holocene lavas. They also diverge in composition from the pre-2006 historical lavas, which are similar to the majority of the 2006 lavas. If this difference is not simply an artifact of a limited dataset, then some of the HSA may be remobilized from a portion of the subvolcanic system, which is at least hundreds of years old. If material this old was erupted, we expect that it represents remobilized crystal mush and did not originate from a persistent liquid + crystal magma. This model is the best that fits both petrological and geophysical data available at this time.

Although the model for the HSA as derived from a crystal mush at 4 to 6 km fits the petrology and geophysical observations, the origins of the crystal mush itself are less well understood. It is tempting to assume that it is derived primarily by fractional crystallization of low-silica andesite remaining in the crust from previous eruptions. However, the trace-element data (fig. 9) argue against this in three ways. First, concentrations of REE heavier than Eu are the same as in the 2006 low-silica andesite. Crystallization at ~100 MPa in these andesites is dominated by plagioclase, and because REE are incompatible, plagioclase crystallization should result in increased REE concentrations in the melt. At other Aleutian volcanoes, crystallization through the andesite and dacite range produces such increases (for example, Finney and others, 2008; Jicha and Singer, 2006). Second, concentrations of other incompatible elements, such as LILE, HFSE, and HPE only increase by 30–50 percent , which is less than half of the increase in other Aleutian andesite systems. Third, Cr and Ni concentrations, although lower than in the LSA, are still much higher than almost all other Aleutian andesites (Nye and others, 2008) and too high to reflect extensive fractional crystallization. The crystals are expected to be relatively depleted in incompatible elements and enriched in compatible elements compared to their host liquids, and a mixture of mush-plus-liquid could have a bulk composition similar to these andesites. Other petrogenetic paths can be imagined, such as production of HSA much deeper, where the pyroxene/plagioclase ratio of precipitating crystals is much higher, but these are less plausible.

Low-Silica Andesite Scoria and Dense Low-Silica Andesite—Similar Heterogeneous Hybrid Magmas

The two low-silica andesites are very similar in terms of bulk-rock composition, mineralogy, and mineral texture, and for most elements form a tight geochemical group that anchors the mafic end of the mixing array that is the dominant geochemical feature of 2006 lavas. LSAS and DLSA both contain reacted crystals, and plagioclase shows the largest degrees of disequilibrium, with roughly 30 percent of plagioclase phenocrysts in the LSA having sieved textures typical of Type 3 plagioclases described above. Elsewhere in 2006 ejecta, these plagioclase phenocrysts are in apparent textural equilibrium only in the HSA samples. Equilibrium plagioclase in the low-silica andesites have An-rich cores and less calcic rims. The composition of microlites and outermost rims of phenocrysts varies from An_{57} to An_{77}, correlating with the large variability of matrix glass compositions (fig. 11). Most likely this is due to rapid crystallization in response to two simultaneous syneruptive processes: (1) decompression (degassing) crystallization and (2) assimilation of the colder host magma.

An important feature of the LSAS erupted in 2006 is the presence of chromite-bearing Fo_{84} olivine and $An_{92\text{-}94}$ plagioclase crystals. In combination with the strongly reacted plagioclase, those phases likely represent xenocrysts. Thus, the LSAS and DLSA are interpreted to be hybrid magmas, with strongly reacted plagioclase crystals representing xenocrysts derived from the LSA and with chromite-bearing olivine crystals and anorthite derived from a more mafic cryptic magma.

The range in temperatures recorded by Fe-Ti oxide microlites in the low-silica andesite scoria is consistent with a mixing origin for this magma. Temperatures range from 825°C, the temperature for the high-silica andesite body, to as high as ~970°C. Because small, unzoned groundmass crystals recorded these temperatures, we interpret the large temperature range to reflect postmixing conditions in the hybrid low-silica andesite magma. These grains either grew during or after mixing, or else they were small enough to undergo diffusive reequilibration. The highest temperature of 970°C may approach that of the injected, unerupted mafic end member.

The most significant, although still small, compositional differences between the dense and scoriaceous low-silica andesites are in Cr, Ni, and to a lesser extent Mg. The majority of LSAS samples, and about half of the DLSA samples have Cr concentrations of 50 to 70 ppm and fall below the dominant mixing array (fig. 9). The low-silica andesite, which anchors the mafic end of the mixing array, is dominantly DLSA and has 75 to 86 ppm Cr. The fact that many low-silica andesite samples fall below the mixing array, yet contain the signature reacted, An-poor, plagioclase crystals we infer to have been acquired during mixing, suggests that these low-Cr low-silica andesites acquired their low-Cr signatures after mixing. Point-count data are neither sufficiently precise nor numerous enough to rigorously constrain this model. However, they provide qualitative support, because the samples with the lowest whole-rock Cr have the lowest modal proportion of mafic phenocrysts and the highest Cr samples have the highest proportion. If the LSA was vertically heterogeneous as it tunneled through the HSA body (for example, Bergantz and Breidenthal, 2001), the top portion could have been relatively gas-rich and crystal-poor relative to the base, because of in-place phase segregation. The first-erupted, gas-rich and relatively crystal-poor LSA would thus have lower Cr, while the lower portion remained to further mix and degas in the HSA body and retained a higher proportion of its phenocrysts during segregation as the LSA dike tunneled through the HSA body.

Unerupted, Mafic End Member

If the low-silica andesites are hybrids, then it is axiomatic that a more mafic magma was present but did not erupt. Influxes of unerupted high-alumina basalt were also invoked to explain the spectrum of magmas erupted during the 1976 and 1986 eruptions, through mixing with a dacite to form the hybrid, low-silica andesites that were the most mafic composition erupted in both cases (Johnston, 1978; Roman and others, 2005). The most mafic magma erupted in 2006 closely resembles the low-silica andesites erupted in 1976 and 1986. We concur with the previous studies and suggest that similar processes were operating in 2006. However, no good candidates for the pure mafic mixing end member exist in the geologic record at Augustine. The only known basalt on Augustine, which erupted in the late Pleistocene, has major and trace element abundances that fall far off the mixing trend of the 2006 ejecta (figs. 7 to 10). Thus, there is no natural analog at Augustine for the replenishing basalt to use in models to constrain the proportion that hybridized to form the LSA. Projection of the 2006 trend to lower silica contents indicates overlap between potential end members and analyzed Aleutian magmas between ~49 and ~53 weight percent silica (not shown in our plots). We suggest that the mafic end member falls within this compositional range, and could perhaps be further constrained by systematic compositional analysis of plagioclase populations within the LSA.

Evidence from other eruptions also shows that the erupted mafic end member must itself be the hybrid result of mixing, such as Lassen 1915 (Clynne, 1999), Miyakejima 1983 (Kuritani and others, 2003), and Hokkaido-Komagatake 1929 (Takeuchi and Nakamura, 2001). Also, in 1996 at Karymsky Volcano in Kamchatka, basalt and andesite erupted simultaneously from two vents. The andesite contained calcic plagioclase that derived from the basalt, but no other signs of mixing, indicating that hybridization was complete and occurred within two months (Izbekov and others, 2002). A similar process at Augustine could have yielded andesite that shows little beyond xenocrysts to reveal its hybridized origin. Hildreth (2007) notes that in the Cascades basaltic lavas are rare, or unknown, at the major polygenetic centers, although common at surrounding monogenetic centers. He infers this basic observation to require that there are efficient filters, perhaps in the form of mush columns, beneath polygenetic volcanoes such as Augustine. In summary, mafic replenishing magmas that do not erupt in their pure form, without hybridization, seem to be the rule, rather than the exception.

Dense Intermediate Andesite and Banded Clasts—Products of Syneruptive Mixing

Compositions and mineral assemblages of DIA are intermediate between HSA and LSA, and discrete domains in banded clasts comprise both end members. The DIA resulted from relatively complete hybridization of the LSA and HSA, whereas banded clasts preserve macroscopic heterogeneity. Because the DIA is most prevalent in the continuous phase, it is likely that mixing was initiated just before the onset of the 2006 eruption and that during the interval between January 17 and 28 mixing between the HSA and LSA was ongoing. Presumably the mixed magma was nearly exhausted during the continuous phase because LSA was the dominant product of the effusive phase.

Fine-Grained Gabbroic and Quartz-Rich Inclusions—Chamber Rind and Frozen Interstitial Liquids?

The fine-grained gabbroic inclusions and low-K HSA samples are both low in incompatible elements (figs. 9, 10), suggesting that they are crystal residua. However, low Cr, Ni, and MgO, high Al_2O_3, and mineral modes from the point-count data all show that the inclusions are plagioclase dominated, suggesting that if they are crystal residua, they formed under conditions where plagioclase crystallization was favored over clinopyroxene. The dominance of plagioclase, coupled with the presence of amphibole, suggests crystallization at mid-crustal depths. The highly evolved, low-K matrix glasses in these lithologies indicate that perhaps any matrix melt that evolved during crystallization was stripped away and that they subsequently remelted to form the evolved, low-K glasses (fig. 11). Perhaps they represent cumulate material that was remelted/mobilized during heating and magma mixing accompanying replenishment. This agrees with Harris (1994), who recognized that magma plumbing beneath Augustine Volcano in 1986 was perhaps more complex than previous workers thought, suggesting the mixing of three distinct magmas: residual 1976 magma, newly injected mafic magma, and partially crystallized chamber ‘rind’ material.

Quartz-rich inclusions have mineralogy and trace-element abundances (fig. 10) radically different from the gabbroic inclusions and must have a different origin. They may be hypabyssal plutonic rocks entrained in and partially melted by young Augustine magmas. Subsequently, the new melt fraction crystallized upon cooling and/or transport to the surface, resulting in the vesicular, fine grained groundmass aggregate of quartz, feldspar, orthopyroxene, and glass. It is unknown from where in the subsurface plumbing system these inclusions were entrained, but their relative abundance in deposits of the continuous phase indicate that they had to have come from depths less than or equal to the high-silica andesite magma body. Differential movement between partial melts and relict crystals likely accounts for drastic alterations in bulk composition from that of the parent magma.

Magma Mixing Processes and Timing

Constraints from Plagioclase Phenocrysts

As discussed in the sections above, there is evidence that two-stage mixing took place before the 2006 eruption, creating the hybrid LSA (mixing event 1) and DIA (mixing event 2) magmas. One way to track magma mixing is through the abundant disequilibrium phenocryst textures observed in the 2006 samples. Perhaps the most complex array of disequilibrium textures is found in the plagioclase phenocrysts (table 9). Just before the mixing events, HSA magma contained Types 1, 2, and 4 plagioclase phenocrysts. Type 1 phenocrysts had uniform compositions of An_{40-50} and had grown entirely in the HSA with no evidence for disequilibrium. Type 2 plagioclases were similar, but more anorthitic spikes and associated resorption zones recorded previous rapid disequilibrium events. Type 4 phenocrysts had more calcic cores with thick overgrowths that suggested that they had been inherited from some previous, more mafic magma. The basaltic end member contained anorthitic, Type 5 plagioclase.

During mixing event 1, efficient mixing between the HSA and basalt formed the hybrid LSA. The new LSA thus contained crystals from both parents—Type 5 from the basalt

Table 9. Sources and mixing paths for plagioclase and olivine types from Augustine 2006 eruptive products.

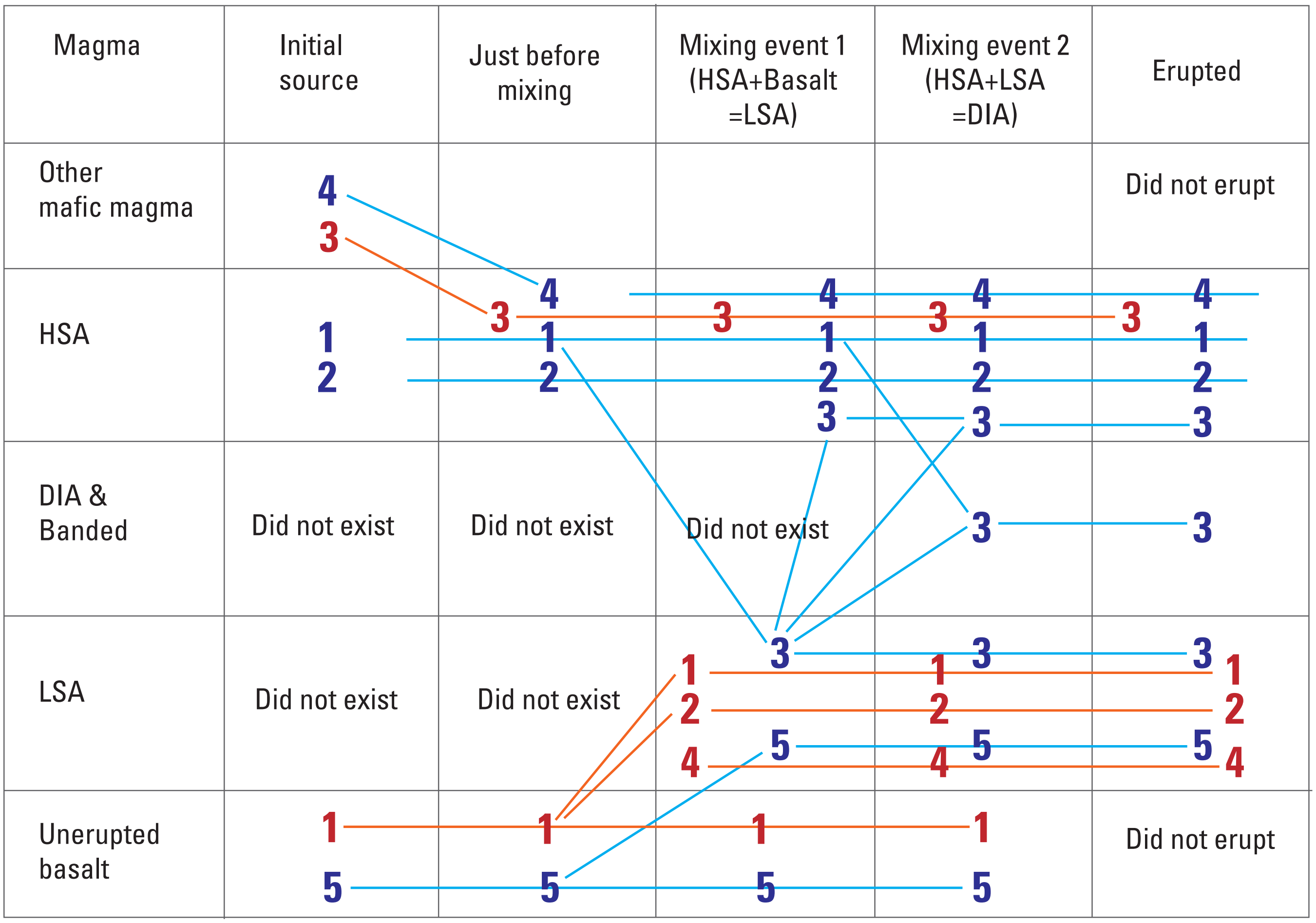

Magma	Initial source	Just before mixing	Mixing event 1 (HSA+Basalt =LSA)	Mixing event 2 (HSA+LSA =DIA)	Erupted
Other mafic magma	4 3				Did not erupt
HSA	1 2	4 3 1 2	3 4 1 2 3	3 4 1 2 3	3 4 1 2 3
DIA & Banded	Did not exist	Did not exist	Did not exist	3	3
LSA	Did not exist	Did not exist	3 1 2 5 4	3 1 2 5 4	3 1 2 5 4
Unerupted basalt	1 5	1 5	1 5	1 5	Did not erupt

Plagioclase
Type 1: Clean, relatively unzoned, $An_{40\text{-}50}$
Type 2: Clean, $An_{40\text{-}50}$ with spikes to An_{75}
Type 3: $An_{40\text{-}50}$ cores with dusty zones and An_{80} spikes
Type 4: An_{70} cores with unzoned $An_{40\text{-}50}$ rims
Type 5: $An_{92\text{-}94}$ cores and thin more sodic rims

Olivine
Type 1: No reaction rim, narrow zoning profile
Type 2: Thin px reaction rim
Type 3: Thick symplectite rim
Type 4: Hopper and swallowtail

and mostly Type 1 from the HSA. These Type 1 crystals, and Types 2 and 4 to a lesser extent, underwent heating and chemical disequilibrium in their new host, leading to dissolution (sieved) zones around the relatively sodic cores. These became Type 3 plagioclase. Some Type 3 plagioclase likely mixed directly back into the HSA during this time period.

During mixing event 2, high-silica andesite and low-silica andesite mixed to form DIA and banded lithologies. This likely occurred predominantly between the end of the explosive phase (January 17) and the beginning of the continuous phase (January 28). The newly formed intermediate andesite incorporated mostly Type 3 plagioclase from the LSA and Type 1 plagioclase from the HSA, the latter of which likely underwent resorption in the somewhat hotter intermediate magma, creating additional Type 3 plagioclase. During this time, some Type 3 plagioclase mixed back into the HSA, as evidenced by some Type 3 crystals with sodic overgrowths that were found in HSA samples.

The clean, sodic rims on Type 3 plagioclase can be used to estimate timing between mixing events and eruption. Rims range in thickness from 10 to 150 microns. Recent estimates of rim growth rates on anorthite seed crystals in rhyodacitic melt range from 3×10^{-10} cm/s to 60×10^{-10} cm/s (Larsen, 2005). These rates yield times of 2 to 40 days for a 10 micron rim and 30 to 560 days for a 150 micron rim. This time range likely encompasses both mixing events described above.

Olivine Reaction Rims and Magma Mixing Time Scales

Another clue about the timing of magma mixing relative to eruption may be found in olivine phenocrysts. Type 3 olivines have pyroxene-magnetite symplectite rims as much as 500 microns thick. These crystals are strongly normally zoned, with Fo_{84} cores and Fo_{74} rims. The wide zoning pattern and thick rims suggest that these have been present and reacting in their current host for long periods of time, probably years to decades (Tilman, 2008). We suggest that these crystals were inherited by the HSA from a mafic magma not related to the 2006 eruption, much like Type 4 plagioclase (table 9). Type 3 olivines are also present in samples from the 1986 eruption and were noted by Johnston (1978) in samples from the 1976 eruption, indicating residence in the HSA mush for at least 30 years. Type 2 olivines have much narrower, pyroxene-only rims and range from Fo_{87} to Fo_{80}, with much narrower zonation in the olivine towards the rim, if present. Similar thin rims of orthopyroxene have been shown to form on olivine xenocrysts when they are introduced into a more silicic magma during magma mixing events (Coombs and Gardner, 2004). Rims on Type 2 olivine in the 2006 rocks range from 10 to 40 microns. The rim growth rate calibrated by Coombs and Gardner (2004) is parabolic, and thus by squaring the average rim width, a linear rate of rim growth with time for a similar melt composition and temperature yields 1.02 micron^2/hr. Applying this rate to the Augustine olivine rims indicates that the olivine crystals were introduced into a new host 4 to 64 days before eruptive quenching. A potentially important difference between their experiments and the Augustine magmas, however, is f_{O_2}. The Coombs and Gardner (2004) experiments were run at an oxygen fugacity of ~Ni-NiO, whereas the 2006 Augustine magmas had an oxygen fugacity of closer to Re-ReO_2 (RRO). Tilman (2008) ran a series of two experiments at this f_{O_2} and obtained a faster rim growth rate. While these results are preliminary, they suggest even shorter times between mixing and eruption, of approximately 12 days for a 40 micron rim. The short duration required to form the thin pyroxene rims from the experiments indicates that they could have formed either during mixing event 1, as olivine was transferred from basalt to andesite, or during mixing event 2, as olivine passed from low-silica andesite to intermediate or high-silica andesite.

Type 4 olivines, with hopper morphologies, are extremely rare in the HSA and uncommon in the mixed and mingled banded and dense intermediate andesite samples. They are similar to hopper olivines observed in the 1976 and 1986 deposits (Harris, 1994; Johnston, 1978). Because many of the hopper grains have a resorption surface that is surrounded by pyroxene growth, the hopper olivines probably grew before mixing event 2. The hopper shape reflects rapid cooling (Faure and others, 2003), and perhaps those olivines originated during mixing event 1 as a result of cooling of the replenishing basalt when it mixed with the cooler HSA (table 9). Following this, mixing event 2 resulted in resorption and pyroxene rim formation during introduction to the HSA.

Groundmass Evolution and Amphibole Reactions During Ascent, Heating, and Cooling

Because of the extreme variations in eruptive style and flux between the three phases of the 2006 eruption (Coombs and others, this volume), one might expect the eruptive products to reflect variations in ascent rate as well. Each discrete Vulcanian blast of the explosive phase was the result of sudden conduit depressurization, emptying the conduit catastrophically of roughly 2×10^6 m^3 of magma until equilibrium was reestablished (Coombs and others, this volume). The continuous phase saw steady ascent of magma from ~5 km depth to the surface. Magma that fed the lava flows of the effusive phase was presumably more degassed and ascended more slowly. Many recent studies have shown that the ascent history of magma will strongly affect the growth of microlites in the groundmass, because decompression drives water from the melt and stabilizes solid phases (for example, Cashman and Blundy, 2000; Geschwind and Rutherford, 1995; Hammer and others, 1999; Hammer and Rutherford, 2002). As microlites grow in the groundmass, the residual melt, and quenched glass, become more evolved. Thus, as a result of the changing ascent rates noted above for the 2006 eruption, we expect to see differences in microlite growth reflected in the groundmass glasses (fig. 11).

In addition to the speed and continuity of the ascent path, magma composition and temperature will affect microlite growth. For example, groundmass microlite content increased systematically with decreasing silica content in andesites and dacites from the 1953 to 1974 eruption of Trident Volcano, even in eruptive units with identical ascent paths (Coombs and others, 2000). Each phase of the 2006 Augustine eruption produced nearly the full range of magmatic compositions, though in widely varying proportions (Vallance and others, this volume). To test whether variations in microlite content and groundmass glass composition are functions of bulk composition, ascent rate, or both, we look at glass compositions and qualitatively at groundmass crystallinity in samples of all lithologies from all three phases.

Groundmass Glasses in the LSA

Low-silica andesite scoria contains microlite-rich groundmass and residual glass that varies widely in composition (fig. 11). This large range exists despite a relatively constant bulk-rock composition and phenocryst assemblage, indicating that the compositional variations reflect changes in microlite content. January 13 tephra follows a similar pattern, and thus these glasses probably evolved the same way. Could the compositional range of the LSAS and early tephra glasses reflect magma mixing instead of late-stage decompression crystallization? If this were the case, one would expect the evolved end of this trend to overlap with matrix glasses from the silicic endmember of the eruption, represented by HSA and the light colored regions in the banded clasts. Instead, the HSA and related samples have glasses that cluster at a lower silica content than the most evolved LSAS and have K_2O contents that place them slightly below the LSAS trend. This suggests that the LSAS matrix-glass trend is not the result of mixing of melt phases between the two end members and that instead the groundmass glass trend is driven by decompression-induced crystallization.

The most evolved LSAS and tephra glasses range to 78.7 weight percent SiO_2, and some quartz was detected in the groundmass using semiquantitative EPMA. The highly evolved melt in the presence of quartz resulted from extensive groundmass crystallization and equilibration at very shallow depths (Cashman and Blundy, 2000). Plotting these evolved glass compositions on a projected quartz-albite-anorthoclase ternary diagram yields equilibration pressures of 25 MPa, equivalent to a depth of about 1 km. Interestingly, one-atmosphere experiments on natural Augustine pumice consistently yielded melt silica contents of 76±1 weight percent (Brugger and others, 2003). Those authors suggest that such magmas only reach more silicic groundmass melt compositions during high degrees of effective undercooling. This is likely the case at Augustine. The wide range in groundmass glass composition in LSAS samples could have resulted from magma parcels being evacuated from a variety of pressures/depths within the conduit during a single explosion (for example, Clarke and others, 2007).

Low-Silica Andesite Amphibole Reaction Rims

Very few amphibole phenocrysts were found in the LSAS, but those that were identified invariably have reaction rims, indicating breakdown of this hydrous phase at some pressure lower than its stability field, either during slow ascent or during a stalling-out period on its way to the surface (Rutherford and Hill, 1993). We suggest that LSAS amphibole reaction rims grew as this magma slowly broke its way to the surface before the eruption (see section A Magmatic Model for Augustine 2006, below). Applying rates of amphibole breakdown determined experimentally in dacites from Redoubt and Mount St Helens, we can estimate a time scale over which the rims likely formed in the Augustine magma, with a few caveats. The average bulk composition of the LSA is lower in silica content than either the Redoubt or St. Helens dacites, while the groundmass glasses range from similar (>76 weight percent) to lower in SiO_2 (~66 weight percent; Browne and Gardner, 2006; Rutherford and Hill, 1993). The temperatures of the LSA are generally hotter than those used in the Redoubt amphibole breakdown experiments ($840^{o}C$; Browne and Gardner, 2006), while those employed by Rutherford and Hill are more similar to the average temperatures of all LSA oxides analyzed (860 to $900^{o}C$, fig. 17). Because temperature appears to have a great influence on amphibole reaction rates during decompression (Browne and Gardner, 2006), it is probably more appropriate here to apply the rates constrained by Rutherford and Hill (1993), despite the differences in bulk and groundmass glass compositions. Thus, the 40-to-100-micron thick rims observed in the LSA indicate that this magma spent ~20 to 57 days outside the amphibole stability field, at shallower depths than about 4 km. Given the first signs of phreatic explosions starting on December 10, and the first explosive phase of the eruption January 12, the range of thicknesses observed in the amphibole breakdown rims indicate initiation of ascent of the LSA magma sometime near mid-November 2005, which correlates very well with geodetic observations as described below.

Alternatively, rimmed amphibole crystals found in low-silica andesite may have derived from another magma, perhaps the high-silica andesite. If this was the case, reaction rims may have formed as the amphibole underwent heating (Browne and Gardner, 2006). Additional analyses of amphibole compositions would further constrain this possibility.

Groundmass Glass Compositions in the HSA

In contrast to the LSA, the high-silica andesite groundmass is nearly microlite-free and has very consistent groundmass glass compositions, for both the explosive and continuous phases. This is true even for HSA samples found in the same deposit as LSAS with microlite-choked groundmass. The HSA did not undergo extensive decompression-induced crystallization during ascent. Because HSA clasts erupted coevally with LSAS, these parcels of magma must have had the same ascent histories. The lack of microlite growth in the HSA is likely to the result of a combination of a more silicic starting composition, which would increase viscosity and inhibit crystal nucleation and growth, and the fact that HSA was likely heated immediately before eruption by mixing, slightly “superheating” the melt phase.

A Magmatic Model for Augustine 2006

Here we combine our petrologic data and conclusions with other geophysical and geologic evidence to construct a model of magma storage, mixing, and movement before and during the 2006 Augustine eruption. In addition to explaining the observations and events of 2006, any feasible model should also address the consistency in eruptive style and composition of the last several Augustine eruptions, which suggests a common, repeatable mechanism.

Several months before the beginning of the eruption, volatile-rich basalt rose through a hot, ductile mid-crustal pathway and intersected the crystal-rich HSA body, probably at a depth of 4–6 km bsl (fig. 20*A*). Evidence from melt inclusion analyses from 2006, 1986, and prehistoric samples (Webster and others, this volume) indicate maximum entrapment pressures of 160 to 200 MPa in rhyolitic inclusions in plagioclase, which indicates maximum depths of about 6 to 8 km for the HSA body, including the estimate from 1986 inclusions. Ascent of the basalt was not detected seismically, but small volcano-tectonic earthquakes began near sea level directly below Augustine’s summit in late April 2005 (Jacobs and McNutt, this volume; Power and Lalla, this volume), and a similarly located weak inflationary source was detected by continuous GPS starting in the summer of 2005 (Cervelli and others, this volume; Cervelli and others, 2006). This zone of geophysical unrest coincides with a region of low to medium seismic velocities interpreted to be dome material overlying sediments interlaced with dikes and sills; these sit atop zeolitized sedimentary strata below 0.9 km bsl (Kienle and others, 1979). We suggest that the shallow unrest resulted from pressurization of the volcanic edifice by gases exsolved from the basalt as it ascended, intersected the HSA, cooled, and crystallized. The total volume change for a modeled point source near sea level is roughly 2×10^5 m^3 (Cervelli and others, 2006), about 2.5 orders of magnitude less than the total erupted volume in 2006 (Coombs and others, this volume).

The introduction of wet basalt into the HSA body first partially reheated the HSA body, lowering its crystal content. The rate of heating of a silicic magma body by a newly introduced hotter body will depend on their size and geometry, but it can take hundreds of days to heat the silicic magma by tens of degrees (Snyder, 2000). Next, the basalt and a newly rejuvenated portion of the HSA body hybridized to form the erupted LSA. This process was likely aided by vesiculation of the basalt as it cooled and crystallized (Huppert and others, 1982; Thomas and others, 1993), causing density instability and convective overturn. The heating of the HSA and hybridization were probably coeval. The homogeneous composition of the LSA indicates that hybridization was thorough, and if it began at the onset of geophysical unrest, it was quick, taking 6 months or less.

A portion of the hybrid LSA then rose through the upper, crystal-rich portion of the HSA body. Whether it took the form of a dike or diapir is unknown and depends on the crystallinity (and thus rigidity) of the HSA body. The LSA then propagated as a dike into the dacite-porphyry crust above the HSA body and ascended toward the surface during the late precursory phase (fig. 20*B*). The LSA was apparently able to initiate dike formation because of its lower viscosity, whereas the crystal-rich HSA was not able to do so. This scenario of a newly arrived, less viscous magma creating a pathway for a resident, crystal-rich magma was proposed by Pallister and others (1996) for the eruption of Mount Pinatubo. Since then, this model has also been applied to the eruption of the Yunokuchi Pumice, Akagi, Japan (Umino and Horio, 1998) and the 1929 eruption of Komagatake volcano, Japan (Takeuchi and Nakamura, 2001). At Komagatake, it was shown that dike propagation of a less viscous mixed andesite magma could occur at a chamber overpressure of only 8 MPa, whereas unrealistically high overpressures would have been required to propagate a dike of the more viscous, crystal-rich silicic magma resident in the chamber.

The exact timing of LSA dike initiation is not known, but GPS data place some constraints on the dike's movement. Edifice-inflation rates increased on November 18, 2005, and GPS data are consistent with propagation of a small dike from 1.25 km depth to the surface between November 18 and January 11 (Cervelli and others, 2006; fig. 20*B*). The upward movement of such a dike at greater depths would not be detected by the Augustine GPS network (P. Cervelli, oral communication, 2008), so it is not known exactly when the dike started its ascent from the HSA body. Modeled dike ascent rates are not constant, and they slow from 100 m/hour around November 25. An offset occurred in the GPS time series on November 17, at a similar time as the appearance of new cracks at the summit of Augustine. This event could point towards the initiation of the rise of the dike just before the edifice inflation rate accelerated on November 18. If we also compare with the preliminary estimates of LSA ascent timescale from the amphibole reaction rims described above, rise of the LSA dike from a depth of ~4 km starting November 17 would indicate that the quickest rising magma would reach the surface around December 7, which is close to the time of the first of the observed phreatic explosions, and the slowest would reach the surface the week of January 12, marking the onset of the explosive phase of the eruption.

Phreatic explosions, increased SO_2 output, and heating of the edifice in December 2005 (McGee and others, this volume; Power and others, 2006; Wessels and others, this volume) all suggest that significant gas had accumulated at the tip of the LSA dike and that some made it to the surface ahead of the LSA magma. A strong swarm of VT earthquakes on January 10–11 likely recorded the final opening of the dike to the surface, but two explosions on January 11 contained little or no juvenile magma (Wallace and others, this volume), and deformation recorded by a summit GPS station continued unabated through these events, suggesting that not much magma was evacuated from the edifice (Cervelli and others, this volume).

LSA magma likely reached the surface on January 12 in the form of a small ephemeral lava dome, recorded by drumbeat earthquakes that signify lava effusion (Power and Lalla, this volume). Vulcanian blasts on January 13, 14, and 17 each drained the conduit to a depth of roughly 2 km below the surface (Coombs and others, this volume; fig. 20C), and produced dominantly LSA deposits, but including a small percentage of HSA as well (Vallance and others, this volume). In between explosions, the conduit refilled with LSA and minor amounts of HSA from the top of the rejuvenated magma body. Explosions were driven by overpressure in the conduit that developed below a degassed lava/magma cap, similar to those seen at Soufriere Hills Volcano, Montserrat (Druitt and others, 2002). The range in LSA groundmass glass compositions indicates that some LSA underwent extensive decompression-driven groundmass crystallization before eruption, likely during storage in the shallow portions of the conduit before explosive release. The continuation of the inflationary trend throughout January indicated that gas pressurization in the shallow subsurface continued throughout this period (Cervelli and others, this volume).

The presence of some HSA in explosive-phase deposits indicates that mixing occurred during the upward passage of the LSA through the HSA body, and/or some HSA was drawn into the dike during LSA ascent. Interestingly, the final, effusive phase of the 2006 eruption was also dominated by LSA,

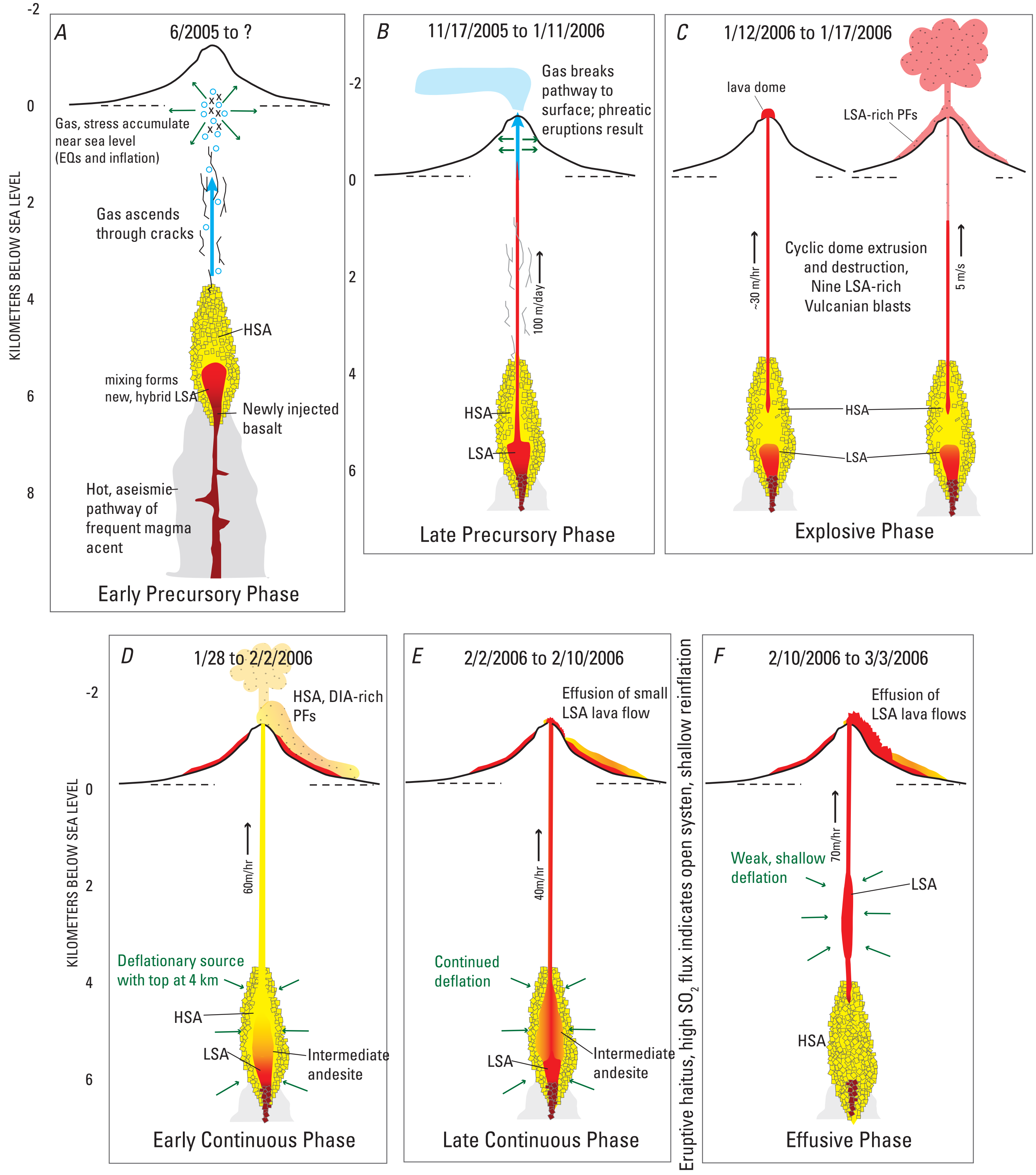

Figure 20. Schematic depiction of magma configuration and events for six time periods before and during the 2006 eruption. HSA is high-silica andesite, DIA is dense intermediate andesite, LSA is low-silica andesite, PF denotes pyroclastic flows.

indicating that in this case, not all of the hybrid andesite was erupted during the initial phase, but that instead some remained at the base of the HSA magma body. It is also clear that during the period between January 17 and 27, continued mixing between LSA and HSA created the more thoroughly mixed intermediate andesite that erupted during the continuous phase.

Slow effusion of a lava dome occurred from January 17 through 27. An explosion on January 27 destroyed this new dome and produced the largest single deposit of the 2006 eruption: about 20 million m^3 of predominantly HSA formed the Rocky Point pyroclastic flow (Coombs and others, this volume; Vallance and others, this volume). This event marked a distinct shift in the dominant composition of erupted material, likely coinciding with exhaustion of the LSA "slug" that made its way through the resident HSA and initially drove the eruption. Whereas earlier explosions were fed only from the conduit, the January 27 explosive event undoubtedly tapped the resident magma body. This is consistent with the fact that for the first time during the eruption, GPS signals record a deep deflation (>4 km depth) that begins around January 27 and continues through February 10 (Cervelli and others, this volume).

Following the explosive eruption of HSA on January 27, ascent and effusion of predominantly HSA occurred for the next several days (Coombs and others, this volume; fig. 20*D*). Little or no LSA was erupted during this interval, but HSA was accompanied by effusion of banded and DIA magmas (Vallance and others, this volume). We interpret this interval as the evacuation of the rejuvenated portion of the resident HSA body through an open conduit from ~5 km to the surface. Ascent rates were high enough for the groundmass to remain microlite-free, though this could also have resulted from the recent heating of the HSA by the LSA.

During the waning of the continuous phase, mass flux continued to be quite high as the north lava flow effused (fig. 20*E*). Eruptable HSA had been exhausted and mostly intermediate andesite was erupted. The deflationary trend overlaps this period, as well as the earlier continuous phase.

During the eruptive pause from February 10 to March 3, high SO_2 emission rates suggested that the system was open and that relatively shallow magma was degassing (McGee and others, this volume). Weak, shallow inflation during this period (Cervelli and others, this volume) is interpreted to have been caused by magma accumulation, somewhere between the HSA body and the surface. This relatively degassed, dense LSA must have been present at the base of the HSA magma body and ascended after the HSA was exhausted.

During the effusive phase, from March 3 through 16, degassed LSA ascended and erupted in the form of two lava flows and a new summit dome (fig. 20*F*). The DLSA brought with it numerous inclusions of fine-grained gabbro, chunks of crystallized portions of the plumbing system.

The 2006 Augustine Eruption in Context

The range in whole-rock compositions of deposits from the 2006 eruption matches that of the historical and most Holocene samples, essentially spanning the andesite range (fig. 7). Basalt and rhyolite erupted coevally in the late Pleistocene but have not erupted since (Waitt and Begét, 2009; J.E. Begét, oral communication). Those rocks fall along a lower K trend compared to historical lavas, including those from 2006. Prehistoric Holocene lavas span a limited SiO_2 range but fall along an intermediate K trend relative to Pleistocene and historical samples. Similarly, many trace-element arrays formed by 2006 and other historical magmas on variation diagrams are elevated in relation to those formed by the Pleistocene basalt and rhyolite. Similar temporal systematics (that is, progressive increase in highly incompatible elements at a given SiO_2 level) have been seen at nearby Redoubt volcano (Begét and Nye, 1994). The differences between the Pleistocene basalt and rhyolite and modern lavas mean that these exact compositions are not appropriate for modeling the modern Augustine magmatic system. However, they do suggest that similar magmas may exist in the modern Augustine system, even if they have not erupted during the Holocene.

Holocene Augustine lavas have high concentrations of compatible transition metals (Mg, Cr, Ni, Fe), and high molar Mg/(Mg+Fe) (Mg#) and dramatically low concentrations of all incompatible trace elements (including LIL, U, Th, Pb, REE, and HFSE) relative to other Aleutian lavas of similar SiO_2 content (fig. 21). Augustine magmas do not follow the liquid line of descent typical of most Aleutian volcanoes where basaltic parental magmas evolve to andesite and dacite accompanied by a steady increase in incompatible elements and decrease in compatible transition metals. Within the andesite range at Augustine the most highly incompatible elements only increase by about 50 percent, and MREE and HREE have constant concentrations (fig. 10). Over similar SiO_2 ranges at other Aleutian volcanoes all incompatible elements (including HREE) increase, with the most incompatible increasing by 200–300 percent (for example, Aniakchak; Dreher and others, 2005; C.J. Nye and others, unpublished data). There are several possible reasons for the low rate of increase of incompatible elements at Augustine, including (a) high crystal/liquid distribution coefficients associated with the high silica content of the groundmass; (b) high effective bulk partition coefficients during crystallization at high pressure, where the ratio of pyroxene ± amphibole to plagioclase is higher; (c) whole-rock concentrations of incompatible elements reflecting a large amount of crystal accumulation; or (d) these magmas being primitive high-Mg# andesites (Kelemen and others, 2003 and 2004), rather than highly evolved fractionates. Possibilities (c) and (d) are also at least qualitatively consistent with the high concentrations of compatible elements in these lavas.

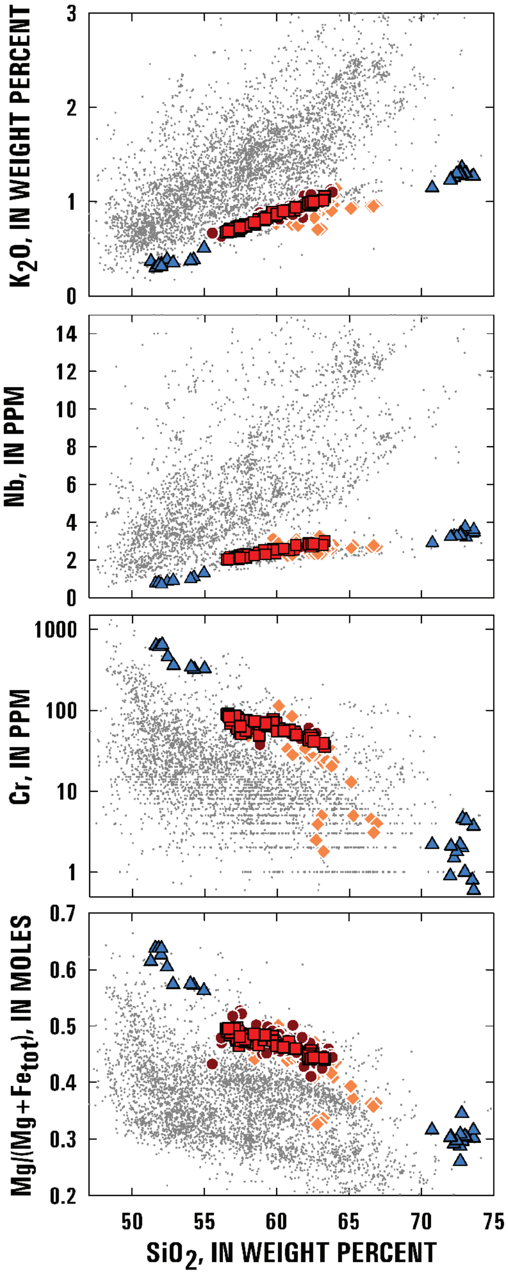

Figure 21. Comparison of Augustine magmas with other Aleutian arc magmas. Augustine magmas are different from the majority of Aleutian magmas in having relatively high Mg# (molar Mg/(Mg+Fe)) and compatible transition metals Cr (shown), as well as Ni and Mg (not shown), as well as low concentrations of incompatible elements, such as K and Nb (shown). The low concentrations of incompatible elements reflect relatively less enrichment with increasing silica in addition to lower-than-average initial concentrations of many incompatible elements. Colored symbols are Augustine lavas (red squares, 2006; dark red circles, pre-2006 historical; orange diamonds, prehistoric late Holocene; blue triangles, late Pleistocene). Gray dots are all other Aleutian analyses from the open literature and unpublished Alaska Volcano Observatory analyses.

It is beyond the scope of this paper to evaluate the above hypotheses. It is our intention instead to point out that Augustine magmas are quite distinct from typical Aleutian magmas, particularly those from the central arc. Trace element concentrations in minerals would be useful in constraining the mineral/melt distribution coefficients during crystallization, thus further constraining petrogenesis. Emphasis on phenocryst mineralogy and petrology in this study shows that especially the low-silica magmas, which erupted, are hybrids requiring the presence of an even lower-silica magma. Thus possibility (d), that these are simply primitive andesites, appears too simple an explanation.

Acknowledgments

It takes an observatory to document an eruption and our understanding of the 2006 eruption of Augustine would not be nearly as complete without the efforts of the entire staff of the Alaska Volcano Observatory. In addition, we thank Jim Webster, Charlie Mandeville, Peter Cervelli, John Power, and Jeff Freymueller for insightful discussion regarding the Augustine magmatic system. Charlie Bacon, Brandon Browne, and Jeff Freymueller provided critical reviews that helped to improve the manuscript. This work was funded by the U.S. Geological Survey's Volcano Hazards Program.

References Cited

Brugger, C.R., Johnston, D.A., and Cashman, K.V., 2003, Phase relations in silicic systems at one-atmosphere pressure: Contributions to Mineralogy and Petrology, v. 146, p. 356–369.

Cashman, K.V., and Blundy, J., 2000, Degassing and crystallization of ascending andesite and dacite: Philosophical Transactions of the Royal Society, v. 358, p. 1487–1513.

Cervelli, P.F., Fournier, T.J., Freymueller, J.T., Power, J.A., Lisowski, M., and Pauk, B.A., 2010, Geodetic constraints on magma movement and withdrawal during the 2006 eruption of Augustine Volcano, *in* Power, J.A., Coombs, M.L., and Freymueller, J.T., eds., The 2006 eruption of Augustine Volcano, Alaska: U.S. Geological Survey Professional Paper 1769 (this volume).

Cervelli, P.F., Fournier, T., Freymueller, J.T., and Power, J.A., 2006, Ground deformation associated with the precursory unrest and early phases of the January 2006 eruption of Augustine Volcano, Alaska: Geophysical Research Letters, doi: 10.1027/2006GL027219.

Clarke, A.B., Stephens, S., Teasdale, R., Sparks, R.S.J., and Diller, K., 2007, Petrologic constraints on the decompression history of magma prior to Vulcanian explosions at the Soufriere Hills Volcano, Montserrat: Journal of Volcanology and Geothermal Research, v. 161, p. 261–274.

Clynne, M.A., 1999, A complex magma mixing origin for rocks erupted in 1915, Lassen Peak, California: Journal of Petrology, v. 40, p. 105–132.

Coombs, M.L., and Gardner, J.E., 2004, Reaction rim growth on olivine in silicic melts—implications for magma mixing: American Mineralogist, v. 89, no. 5–6, p. 748–759.

Coombs, M.L., Eichelberger, J.C., and Rutherford, M.J., 2000, Magma storage and mixing conditions for the 1953-1974 eruptions of Southwest Trident volcano, Katmai National Park, Alaska: Contributions to Mineralogy and Petrology, v. 140, no. 1, p. 99–118.

Coombs, M.L., Bull, K.F., Vallance, J.W., Schneider, D.J., Thoms, E.E., Wessels, R.L., and McGimsey, R.G., 2010, Timing, distribution, and volume of proximal products of the 2006 eruption of Augustine Volcano, *in* Power, J.A., Coombs, M.L., and Freymueller, J.T., eds., The 2006 eruption of Augustine Volcano, Alaska: U.S. Geological Survey Professional Paper 1769 (this volume).

Costa, F., and Chakraborty, S., 2004, Decadal time gaps between mafic intrusion and silicic eruption obtained from chemical zoning patterns in olivine: Earth and Planetary Science Letters, v. 227, p. 517–530.

Daley, E.E., 1986, Petrology, geochemistry, and the evolution of magmas from Augustine Volcano, Alaska: University of Alaska Fairbanks, unpublished M.S. thesis, 103 p.

Detterman, R.L., and Reed, B.L., 1980, Stratigraphy, structure, and economic geology of the Iliamna Quadrangle, Alaska: U.S. Geological Survey Bulletin, 1368-B, 86 p.

Dreher, S.T., Eichelberger, J.C., and Larsen, J.F., 2005, The petrology and geochemistry of the Aniakchak caldera-forming ignimbrite, Aleutian Arc, Alaska: Journal of Petrology, v. 46, p. 1747–1768.

Druitt, T.H., Young, S.R., Baptie, B., Bonadonna, C., Calder, E.S., Clarke, A.B., Cole, P.D., Harford, C.L., Herd, R.A., Luckett, R., Ryan, G., and Voight, B., 2002, Episodes of cyclic Vulcanian explosive activity with fountain collapse at Soufriere Hills Volcano, Montserrat, *in* Druitt, T.H., and Kokelaar, B.P., eds., The eruption of Soufriere Hills Volcano, Montserrat, from 1995 to 1999: London, The Geological Society, p. 281–306.

Evans, B.W., Scaillet, B., and Kuehner, S.M., 2006, Experimental determination of coexisting iron-titanium oxides in the systems FeTiAlO, FeTiAlMgO, FeTiAlMnO, and FeTiAlMgMnO at 800 and 900°C, 1–4 kbar, and relatively high oxygen fugacity: Contributions to Mineralogy and Petrology, v. 152, p. 149–167.

Faure, F., Trolliard, G., Nicollet, C., and Montel, J.-M., 2003, A developmental model of olivine morphology as a function of the cooling rate and the degree of undercooling: Contributions to Mineralogy and Petrology, v. 145, p. 251–263.

Finney, B., Turner, S., Hawkesworth, C., Larsen, J.F., MNye, C., George, R., Bindeman, I., and Eichelberger, J.C., 2008, Magmatic differentiation at an island-arc caldera—Okmok Volcano, Aleutian Islands, Alaska: Journal of Petrology, v. 49, no. 857–884.

Geschwind, C.H., and Rutherford, M.J., 1995, Crystallization of microlites during magma ascent—The fluid mechanics of the 108086 eruptions at Mount St. Helens: Bulletin of Volcanology, v. 57, p. 356–370.

Ghiorso, M.S., and Evans, B.W., 2008, Thermodynamics of rhombohedral oxide solid solutions and a revision of the Fe-Ti two-oxide geothermometer and oxygen-barometer: American Journal of Science, v. 308, p. 957–1039.

Gill, J.B., 1981, Orogenic andesites and plate tectonics: Springer-Verlag, Berlin, 370 p.

Hammer, J.E., and Rutherford, M.J., 2002, An experimental study of the kinetics of decompression-induced crystallization in silicic melt: Journal of Geophysical Research, v. 107, p. 148–227.

Hammer, J.E., Cashman, K.V., Hoblitt, R.P., and Newman, S., 1999, Degassing and microlite crystallization during preclimactic events of the 1991 eruption of Mount Pinatubo, Philippines: Bulletin of Volcanology, v. 60, p. 335–380.

Harris, G.W., 1994, The petrology and petrography of lava from the 1986 eruption of Augustine volcano: University of Alaska Fairbanks unpublished M.S. thesis, Fairbanks, AK, 131 p.

Hildreth, E.W., 2007, Quaternary Magmatism in the Cascades—Geologic Perspectives: U.S. Geological Survey Professional Paper 1744, 136 p.

Huppert, H.E., Sparks, R.S.J., and Turner, J.S., 1982, Effects of volatiles on mixing in calc-alkaline magma systems: Nature, v. 297, p. 554–557.

Izbekov, P., Eichelberger, J.C., Patino, L.C., Vogel, T.A., and Ivanov, B.V., 2002, Calcic cores of plagioclase phenocrysts in andesite from Karymsky volcano—evidence for rapid introduction by basaltic replenishment: Geology, v. 30, p. 799–802.

Jacobs, K.M., and McNutt, S.R., 2010, Using seismic *b*-values to interpret seismicity rates and physical processes during the preeruptive earthquake swarm at Augustine Volcano 2005–2006, *in* Power, J.A., Coombs, M.L., and Freymueller, J.T., eds., The 2006 eruption of Augustine Volcano, Alaska: U.S. Geological Survey Professional Paper 1769 (this volume).

Jicha, B.R., and Singer, B.S., 2006, Volcanic history and magmatic evolution of Seguam Island, Aleutian Island arc, Alaska: Geological Soceity of America Bulletin, v. 118, p. 805–822.

Johnson, K.E., Strong, D.F., Harmon, R.S., Richardson, J. M., and Moorbath, S., 1996, Isotope and trace element geochemistry of Augustine volcano, Alaska—implications for magmatic evolution: Journal of Petrology, v. 37, p. 95–115.

Johnson, D.M., Hooper, P.R., and Conrey, R.M., 1999, XRF analysis of rocks and minerals for major and trace elements on a single low dilution Li-tetraborate fused bead: Advances in x-ray Analysis, v. 41, p. 843–867.

Johnston, D.A., 1978, Volatiles, magma mixing, and the mechanism of eruption at Augustine volcano, Alaska: University of Washington Ph.D. dissertation, 187 p., 20 plates.

Kelemen, P.B., Yogodzinski, G.M., and Scholl, D.W., 2003, Along strike variation in the Aleutian Island arc—genesis of high Mg# andesite and implications for continental crust, *in* Eiler, J., ed., Inside the Subduction Factory, American Geophysical Union Monograph 138, p. 1–54.

Kelemen, P.B., Hanghoj, K., and Greene, A.R., 2004, One view of the geochemistry of subduction-related magmatic arcs, with an emphasis on primitive andesite and the lower crust, *in* Rudnick, R.L., ed., The crust: Elsevier Ltd., p. 593–659.

Kienle, J., and Swanson, S.E., 1983, Volcanism in the eastern Aleutian Arc—late Quaternary and Holocene centers, tectonic setting and petrology: Journal of Volcanology and Geothermal Research, v. 17, no. 1-4, p. 393–432.

Kienle, J., Lalla, D.J., Pearson, C.F., and Barrett, S. A., 1979, Search for shallow magma accumulations at Augustine volcano: University of Alaska Fairbanks Geophysical Institute Final Report to U.S. Dept. of Energy, Washington D.C. 157 p.

Knaack, C., Cornelius, S.B., and Hooper, P.R., 1994, Trace element analyses of rocks and minerals by ICP-MS: Open File Report, Department of Geology, Washington State University [http://www.wsu.edu/~geolab/].

Kuritani, T., Yokoyama, T., Kobayashi, K., and Nakamura, E., 2003, Shift and rotation of composition trends by magma mixing—1983 eruption at Miyakejima Volcano, Japan: Journal of Petrology, v. 44, p. 1895–1916.

Larsen, J.F., 2005, Experimental study of plagioclase rim growth around anorthite seed crystals in rhyodacitic melt: American Mineralogist, v. 90, p. 417–427.

Lattard, D., Sauerzapf, U., and Kasemann, M., 2005, New calibration data for the Fe-Ti oxide thermo-oxybarometers from experiments in the Fe-Ti-O system at 1 bar, 1,000–1,300°C and a large range of oxygen fugacities: Contributions to Mineralogy and Petrology, v. 149, p. 735–754.

LeMaitre, R.W., 1991, A classification of igneous rocks and glossary of terms: Oxford, Blackwell Scientific Publications, 193 p.

McGee, K.A., Doukas, M.P., McGimsey, R.G., Neal, C.A., and Wessels, R.L., 2010, Emission of SO_2, CO_2 and H_2S from Augustine Volcano, 2002–2008, *in* Power, J.A., Coombs, M.L., and Freymueller, J.T., eds., The 2006 eruption of Augustine Volcano, Alaska: U.S. Geological Survey Professional Paper 1769 (this volume).

Murphy, M.D., Sparks, R.S.J., Barclay, J., Carroll, M.R., and Brewer, T.S., 2000, Remobilization of andesite magma by intrusion of mafic magma at the Soufriere Hills Volcano, Montserrat, West Indies: Journal of Petrology, v. 41, p. 21–42.

Nakamura, M., 1995, Continuous mixing of crystal mush and replenished magma in the ongoing Unzen eruption: Geology, v. 23, p. 807–810.

Nakamura, M., and Shimikata, S., 1998, Kinetic constraints on the mode of magma mixing and ascent in the 1991 Unzen eruption: Earth and Planetary Science Letters, v. 161, p. 119–133.

Nye, C., Coombs, M.L., Larsen, J.F., Izbekov, P., Tilman, M., and Cameron, C., 2008, Augustine Volcano—Mg-, Cr-, and Ni-rich; LILE, REE, and HFSE-poor: Geochimica et Cosmochimica Acta, v. 72, p. A692.

Pallister, J.S., Hoblitt, R.P., Meeker, G.P., Knight, R.J., and Siems, D.F., 1996, Magma mixing at Mount Pinatubo—petrographic and chemical evidence from the 1991 deposits, *in* Newhall, C.G., and Punonhbayan, R., eds., Fire and mud—eruptions and lahars of Mount Pinatubo: Seattle, University of Washington Press, p. 687–731.

Plank, T., Zimmer, M.M., Hauri, E.H., and Nye, C.J., 2006, The Augustine basalt: Eos (American Geophysical Union Transactions), Fall Meeting Supplement, v. 87, abs. V42B-06.

Power, J.A., 1988, Seismicity associated with the 1986 eruption of Augustine Volcano, Alaska: University of Alaska Fairbanks, unpublished M.S. thesis, 142 p.

Power, J.A., and Lalla, D.J., 2010, Seismic observations of Augustine Volcano, 1970–2007, *in* Power, J.A., Coombs, M.L., and Freymueller, J.T., eds., The 2006 eruption of Augustine Volcano, Alaska: U.S. Geological Survey Professional Paper 1769 (this volume).

Power, J.A., Nye, C.J., Coombs, M.L., Wessels, R.L., Cervelli, P.F., Dehn, J., Wallace, K.L., Freymueller, J.T., and Doukas, M.P., 2006, The reawakening of Alaska's Augustine Volcano: Eos (American Geophysical Union Transactions), v. 87, no. 37, p. 373, 377.

Pownceby, M.I., and O'Neill, H.St.C 1994, Thermodynamic data from redox reactions at high temperatures. IV. Calibration of the Re-ReO_2 oxygen buffer from EMF and NiO+Ni-Pd redox sensor measurements: Contributions to Mineralogy and Petrology, v. 118, p. 130–137.

Roman, D.C., Cashman, K.V., Gardner, C.A., Wallace, P., and Donovan, J., 2005, Storage and interaction of compositionally heterogeneous magmas from the 1986 eruption of Augustine Volcano, Alaska: Bulletin of Volcanology, v. 68, p. 240–254.

Rutherford, M.J., and Devine, J.D., 1996, Preeruption pressure-temperature conditions and volatiles in the 1991 dacitic magma of Mount Pinatubo, *in* Newhall, C.G., and Punongbayan, R.S., eds., Fire and Mud—eruptions and lahars of Mount Pinatubo, Philippines: Seattle, University of Washington Press, p. 751–766.

Rutherford, M.J., and Hill, P.M., 1993, Magma ascent rates from amphibole breakdown—an experimental study applied to the 1980-1986 Mount St. Helens eruptions: Journal of Geophysical Research, v. 98, p. 19667–19685.

Snyder, D., 2000, Thermal effects of the intrusion of basaltic magma into a more silicic magma chamber and implications for eruption triggering: Earth and Planetary Science Letters, v. 175, p. 257–273.

Stormer, J.C., 1983, The effects of recalculation on estimates of temperature and oxygen fugacity from analyses of multicomponent iron-titanium oxides: American Mineralogist, v. 68, p. 586–594.

Syracuse, E.M., and Abers, G.A., 2006, Global compilation of variations in slab depth beneath arc volcanoes and implications: Geochemistry, Geophysics, Geosystems, v. 7, no. 5, p. Q05017, doi:05010.01029/02005GC001045.

Takeuchi, S., and Nakamura, M., 2001, Role of precursory less-viscous mixed magma in the eruption of phenocryst-rich magma—evidence from the Hokkaido-Komagatake 1929 eruption: Bulletin of Volcanology, v. 63, p. 365–376.

Tappen, C.M., Webster, J.D., Mandeville, C.W., and Roderick, D., 2009, Petrology and geochemistry of prehistoric pumice fall eruptions (2100–1000 a.B.P.) at Mt. St. Augustine Volcano, Alaska: Journal of Volcanology and Geothermal Research, v. 183, p. 42–62.

Thomas, N., Tait, S., and Koyaguchi, T., 1993, Mixing of stratified liquids by the motion of gas bubbles—application to magma mixing: Earth and Planetary Science Letters, v. 115, p. 161–175.

Tilman, M.R., 2008, An investigation of symplectite-rimmed olivine and magmatic processes during the 2006 eruption of Augustine Volcano, Alaska: University of Alaska Fairbanks, unpublished M.S. thesis, 166 p.

Tsuchiyama, A., 1985, Dissolution kinetics of plagioclase in the melt of the system diopside-albite-anorthite and origin of dusty plagioclase in andesites: Contributions to Mineralogy and Petrology, v. 89, p. 1–16.

Umino, S., and Horio, A., 1998, Multistage magma mixing revealed in phenocryst zoning of the Yunokuchi Pumice, Akagi Volcano, Japan: Journal of Petrology, v. 39, p. 101–124.

Vallance, J.W., Bull, K.F., and Coombs, M.L., 2010, Pyroclastic flows, lahars, and mixed avalanches generated during the 2006 eruption of Augustine Volcano, *in* Power, J.A., Coombs, M.L., and Freymueller, J.T., eds., The 2006 eruption of Augustine Volcano, Alaska: U.S. Geological Survey Professional Paper 1769 (this volume).

Waitt, R.B., and Begét, J.E., 2009, Volcanic processes and geology of Augustine Volcano, Alaska: U.S. Geological Survey Professional Paper 1762, 78 p., 2 map plates [http://pubs.usgs.gov/pp/1762/].

Waitt, R.B., 2010, Ejecta and landslides from Augustine Volcano before 2006, *in* Power, J.A., Coombs, M.L., and Freymueller, J.T., eds., The 2006 eruption of Augustine Volcano, Alaska: U.S. Geological Survey Professional Paper 1769 (this volume).

Wallace, K.L., Neal, C.A., and McGimsey, R.G., 2010, Timing, distribution, and character of tephra fall from the 2005–2006 eruption of Augustine Volcano, *in* Power, J.A., Coombs, M.L., and Freymueller, J.T., eds., The 2006 eruption of Augustine Volcano, Alaska: U.S. Geological Survey Professional Paper 1769 (this volume).

Waythomas, C.F., and Waitt, R.B., 1998, Preliminary volcano-hazard assessment for Augustine Volcano, Alaska: U.S. Geological Survey Open-File Report 98-0106, 39 p., 1 plate, scale unknown.

Webster, J.D., Mandeville, C.W., Goldoff, B., Coombs, M.L., and Tappen, C., 2010, Augustine Volcano—The influence of volatile components in magmas erupted A.D. 2006 to 2,100 years before present, *in* Power, J.A., Coombs, M.L., and Freymueller, J.T., eds., The 2006 eruption of Augustine Volcano, Alaska: U.S. Geological Survey Professional Paper 1769 (this volume).

Wessels, R.L., Coombs, M.L., Schneider, D.J., Dehn, J., and Ramsey, M.S., 2010, High-resolution satellite and airborne thermal infrared imaging of the 2006 eruption of Augustine Volcano, *in* Power, J.A., Coombs, M.L., and Freymueller, J.T., eds., The 2006 eruption of Augustine Volcano, Alaska: U.S. Geological Survey Professional Paper 1769 (this volume).

Tables 2–8

Table 2. Summary of modal abundances for Augustine 2006 lithologies as determined by point counting.

[Each value is average of n samples within each lithology, in volume percent; one standard deviation is given in parentheses. All values, except for void space, are calculated on a void-free basis. At least, 1,000 points were counted for all samples. LSAS, low-silica andesite scoria; DLSA, dense low-silica andesite; DIA, dense intermediate andesite; FGGI, fine-grained gabbroic inclusions. n.p., not present]

	LSAS	**DLSA**	**DIA**	**Banded**	**HSA**	**FGGI**
Plagioclase	23.7 (3.1)	25.9 (3.4)	25.9 (7.0)	28.1 (6.2)	31.9 (5.2)	56.9 (10.6)
Clinopyroxene	5.8 (3.1)	6.1 (2.3)	4.8 (2.9)	5.2 (1.5)	6.4 (3.2)	4.3 (3.6)
Orthopyroxene	4.0 (1.4)	3.7 (1.0)	3.6 (1.8)	4.7 (1.3)	4.1 (1.5)	3.1 (0.2)
Opaques	1.8 (0.9)	2.4 (1.8)	2.6 (3.0)	1.6 (0.7)	1.8 (0.5)	3.8 (0.7)
Olivine	1.1 (0.9)	1.3 (0.4)	0.6 (0.5)	0.3 (0.3)	0.2 (0.2)	n.p.
Amphibole	n.p.	0.0 (0.1)	n.p.	0.0 (0.1)	0.1 (0.1)	6.1 (5.2)
Apatite	n.p.	n.p.	n.p.	0.0 (0.1)	0.0 (0.1)	n.p.
Anhydrite	0.0 (0.1)	n.p.	n.p.	0.0 (0.1)	n.p.	0.0 (0.1)
Total phenocrysts	36.7 (4.9)	39.5 (3.4)	37.7 (10.4)	40.0 (6.5)	44.8 (7.2)	73.6 (11.9)
Crystalline groundmass	63.1 (5.0)	60.2 (3.7)	51.5 (29.3)	21.6 (24.7)	1.2 (1.5)	0.1 (0.1)
Glass	0.1 (0.2)	0.0 (0.1)	10.7 (23.4)	38.3 (26.0)	53.9 (6.5)	26.3 (12.0)
Voids	33.4 (5.3)	19.8 (4.0)	22.1 (3.4)	38.7 (9.5)	37.4 (7.9)	29.8 (2.9)
n	12	7	5	8	7	2

Table 3. Representative whole-rock compositions of Augustine 2006 eruptive products.

[The prefix “06AU” has been truncated from all sample IDs. Total iron (FeO_t) as FeO]

Phase	**Explosive**				**Continuous**		**Effusive**		
Map unit	**ExPfc**	**RPpf**	**ExPfc**	**RPpf**	**Cpf**	**Cpf**	**EfLf**	**Efba**	**EfLf**
Lithology	**DLSA**	**LSAS**	**DIA**	**HSA**	**DIA**	**HSA**	**DLSA**	**DIA**	**DIA**
Sample ID	**MRT037f**	**MRT009b**	**MRT037e**	**MC004c1**	**MRT017a**	**MRT017b**	**MLC057**	**KB002C**	**MLC028**
Major elements measured by XRF in weight percent normalized to 100. LOI not determined. Total is original analytical total.									
SiO_2	57.07	57.20	58.39	62.52	59.97	62.27	57.07	59.11	62.23
TiO_2	0.732	0.711	0.682	0.558	0.625	0.555	0.729	0.668	0.569
Al_2O_3	17.59	17.79	17.37	16.48	17.00	16.92	17.46	17.05	16.77
FeO_t	6.70	6.71	6.38	5.39	5.98	5.19	6.60	6.27	5.26
MnO	0.144	0.148	0.144	0.129	0.137	0.126	0.143	0.139	0.128
MgO	4.87	4.57	4.49	3.43	4.09	3.28	5.04	4.40	3.37
CaO	8.59	8.52	8.11	6.58	7.60	6.71	8.74	7.94	6.73
Na_2O	3.45	3.50	3.53	3.78	3.59	3.81	3.38	3.48	3.82
K_2O	0.720	0.697	0.770	0.999	0.875	0.983	0.702	0.804	0.996
P_2O_5	0.125	0.141	0.134	0.137	0.133	0.139	0.127	0.134	0.134
Total	98.76	99.13	99.05	100.34	98.60	99.43	98.42	99.73	98.66
Trace elements measured by XRF, in ppm.									
Ni	28.6	24.3	26.0	19.9	26.5	18.7	35.9	32.2	20.6
Cr	62.0	52.7	56.5	45.3	51.8	41.7	82.0	67.0	45.7
Sc	26.4	23.2	23.0	17.7	21.3	17.3	26.6	23.0	17.5
V	204	194	186	134	164	131	203	179	139
Ba	306	303	340	457	386	443	301	356	435
Rb	12.5	12.6	13.8	19.4	16.0	19.6	12.6	14.5	19.7
Sr	324	342	328	321	320	329	319	318	323
Zr	86	86	91	114	102	107	85	96	107
Y	20.9	20.6	21.1	20.9	22.8	20.3	20.1	19.6	21.0
Nb	2.2	1.5	2.3	3.0	2.7	1.9	1.2	2.1	2.0
Ga	17.3	18.2	17.3	14.9	17.1	15.3	16.4	17.2	17.5
Cu	36.3	35.2	33.7	24.3	31.5	17.3	18.2	25.2	22.5
Zn	65.7	63.7	64.7	60.1	61.2	58.1	61.0	57.1	56.4
Trace elements measured by ICPMS, in ppm.									
La	7.81	7.90	8.60	9.92	9.68	10.56	7.83	9.12	10.51
Ce	17.40	17.57	18.94	21.22	21.11	22.66	17.40	20.07	22.50
Pr	2.474	2.503	2.653	2.860	2.893	3.024	2.485	2.802	3.021
Nd	11.10	11.41	11.68	12.26	12.61	13.19	11.14	12.34	12.85
Sm	2.900	3.034	3.106	3.042	3.205	3.198	2.945	3.211	3.184
Eu	1.003	1.019	1.012	0.903	1.006	1.001	1.001	1.020	0.965
Gd	3.306	3.349	3.309	3.072	3.505	3.366	3.301	3.439	3.285
Tb	0.576	0.580	0.579	0.539	0.614	0.573	0.575	0.590	0.576
Dy	3.614	3.697	3.691	3.438	4.016	3.653	3.737	3.794	3.621
Ho	0.766	0.776	0.770	0.718	0.852	0.765	0.767	0.799	0.763
Er	2.141	2.202	2.210	2.067	2.414	2.166	2.145	2.278	2.205
Tm	0.328	0.332	0.335	0.319	0.362	0.340	0.329	0.351	0.332
Yb	2.111	2.152	2.165	2.084	2.394	2.180	2.128	2.244	2.204
Lu	0.344	0.350	0.352	0.345	0.386	0.363	0.344	0.363	0.364

Table 3. Representative whole-rock compositions of Augustine 2006 eruptive products.—Continued

[The prefix “06AU” has been truncated from all sample IDs. Total iron (FeO_t) as FeO]

Phase	Explosive				Continuous		Effusive		
Map unit	ExPfc	RPpf	ExPfc	RPpf	Cpf	Cpf	EfLf	Efba	EfLf
Lithology	DLSA	LSAS	DIA	HSA	DIA	HSA	DLSA	DIA	DIA
Sample ID	MRT037f	MRT009b	MRT037e	MC004c1	MRT017a	MRT017b	MLC057	KB002C	MLC028
Trace elements measured by ICPMS, in ppm.									
Ba	305	296	337	415	381	439	299	356	440
Th	1.446	1.376	1.615	2.082	1.930	2.144	1.454	1.757	2.143
Nb	2.088	2.028	2.286	2.576	2.526	2.702	2.056	2.387	2.693
Y	19.87	20.42	20.17	19.20	22.24	20.32	19.60	20.71	20.47
Hf	2.388	2.303	2.560	2.837	2.742	2.937	2.341	2.676	2.998
Ta	0.145	0.147	0.159	0.187	0.180	0.193	0.145	0.168	0.192
U	0.582	0.561	0.661	0.847	0.796	0.886	0.585	0.732	0.909
Pb	1.897	1.855	2.125	2.503	2.352	2.686	2.037	1.351	2.648
Rb	12.59	12.25	13.91	17.40	16.07	18.32	12.42	14.83	18.90
Cs	0.284	0.267	0.314	0.415	0.362	0.400	0.272	0.332	0.412
Sr	319	337	325	288	316	327	313	318	322
Sc	24.35	23.39	22.28	15.65	20.16	16.31	25.20	22.71	16.39
Zr	80.8	81.9	87.1	98.8	97.6	103.6	80.2	92.7	104.0

Table 4. Groundmass glass average compositions of Augustine 2006 eruptive products by lithology and sample.

[Sample lithology acronyms are as noted in text. FeO_t—All Fe analyzed as FeO. Analyses reported are normalized to 100% volatile-free. Original totals are reported. n denotes the total number of analyses averaged to give the reported glass compositions. Numbers in parentheses are the standard deviations from the averaged analyses (n total from each thin section)]

Sample-	06AUMC005c	06AUMRT037c	06AUMC007c	06AUMRT009b	06AUMRT037b	06AUMC008a
	LSAS	LSAS	LSAS	DLSA	DLSA	Banded
SiO_2	71.16 (1.57)	77.38 (0.52)	67.48 (1.02)	70.04 (2.07)	68.98 (2.70)	69.25
TiO_2	0.97 (0.29)	0.37 (0.05)	1.17 (0.19)	1.13 (0.12)	0.65 (0.28)	1.33
Al_2O_3	13.72 (0.92)	11.90 (0.28)	14.33 (0.37)	13.77 (0.72)	15.16 (1.30)	13.88
FeO_t	4.03 (0.46)	1.71 (0.19)	5.38 (0.66)	4.04 (0.31)	3.54 (0.69)	4.04
MnO	0.12 (0.07)	0.07 (0.08)	0.17 (0.10)	0.01 (0.00)	0.05 (0.03)	0.07
MgO	0.90 (0.11)	0.37 (0.05)	1.40 (0.21)	0.74 (0.12)	0.64 (0.19)	0.57
CaO	3.13 (0.49)	1.30 (0.18)	4.05 (0.25)	3.37 (0.89)	4.14 (1.07)	3.39
Na_2O	3.37 (0.42)	3.90 (0.12)	3.65 (0.23)	4.21 (0.57)	4.65 (0.59)	4.65
K_2O	2.06 (0.24)	2.90 (0.14)	1.76 (0.18)	1.93 (0.13)	1.80 (0.30)	2.08
P_2O_5	0.23 (0.08)	0.02 (0.04)	0.30 (0.05)	0.46 (0.36)	0.19 (0.08)	0.36
Cl	0.30 (0.08)	0.07 (0.02)	0.31 (0.03)	0.29 (0.03)	0.20 (0.07)	0.38
Totals	99.15	100.18	100.02	100.30	98.53	98.56
n	13	6	11	3	6	1

Table 4. Groundmass glass average compositions of Augustine 2006 eruptive products by lithology and sample.—Continued

[Sample lithology acronyms are as noted in text. FeO_t—All Fe analyzed as FeO. Analyses reported are normalized to 100% volatile-free. Original totals are reported. n denotes the total number of analyses averaged to give the reported glass compositions. Numbers in parentheses are the standard deviations from the averaged analyses (n total from each thin section)]

Sample	06AUMC005c	06AUMRT017a	06AUMRT037e	06AUKFB128	06AUMC004a	06AUMRT017b
	Banded	DIA	DIA	HSA	HSA	HSA
SiO_2	75.54 (0.61)	72.07 (3.65)	69.68	75.70 (0.42)	75.73 (0.68)	75.52 (0.51)
TiO_2	0.38 (0.13)	0.39 (0.12)	0.26	0.43 (0.19)	0.45 (0.18)	0.33 (0.13)
Al_2O_3	12.57 (0.29)	14.23 (1.78)	15.49	12.86 (0.16)	12.85 (0.39)	12.96 (0.34)
FeO_t	1.89 (0.16)	2.52 (0.72)	2.90	1.91 (0.11)	2.05 (0.18)	2.02 (0.16)
MnO	0.07 (0.07)	0.16 (0.08)	0.09	0.05 (0.04)	0.08 (0.08)	0.06 (0.03)
MgO	0.46 (0.13)	0.84 (0.49)	0.58	0.41 (0.04)	0.42 (0.06)	0.41 (0.04)
CaO	2.08 (0.24)	3.51 (1.18)	3.83	2.10 (0.13)	2.08 (0.06)	2.11 (0.17)
Na_2O	4.46 (0.33)	4.08 (0.95)	4.79	4.10 (0.19)	3.83 (0.38)	4.16 (0.16)
K_2O	2.10 (0.13)	1.83 (0.39)	1.78	2.12 (0.10)	2.16 (0.22)	2.07 (0.13)
P_2O_5	0.07 (0.04)	0.12 (0.07)	0.18	0.07 (0.05)	0.08 (0.03)	0.09 (0.03)
Cl	0.39 (0.07)	0.27 (0.07)	0.43	0.25 (0.07)	0.26 (0.06)	0.28 (0.07)
Totals	99.82	99.95	100.12	99.51	99.42	99.21
n	19	7	1	30	52	9

Sample	06AUKFB128	06AUMC004a	06AUMRT017b	06AUMC009p1
	HSA	HSA	HSA	HSA
SiO_2	75.70 (0.42)	75.73 (0.68)	75.52 (0.51)	75.34 (0.25)
TiO_2	0.43 (0.19)	0.45 (0.18)	0.33 (0.13)	0.28 (0.15)
Al_2O_3	12.86 (0.16)	12.85 (0.39)	12.96 (0.34)	12.80 (0.26)
FeO_t	1.91 (0.11)	2.05 (0.18)	2.02 (0.16)	1.83 (0.09)
MnO	0.05 (0.04)	0.08 (0.08)	0.06 (0.03)	0.09 (0.06)
MgO	0.41 (0.04)	0.42 (0.06)	0.41 (0.04)	0.36 (0.03)
CaO	2.10 (0.13)	2.08 (0.06)	2.11 (0.17)	2.03 (0.14)
Na_2O	4.10 (0.19)	3.83 (0.38)	4.16 (0.16)	4.69 (0.20)
K_2O	2.12 (0.10)	2.16 (0.22)	2.07 (0.13)	2.07 (0.06)
P_2O_5	0.07 (0.05)	0.08 (0.03)	0.09 (0.03)	0.09 (0.05)
Cl	0.25 (0.07)	0.26 (0.06)	0.28 (0.07)	0.42 (0.07)
Totals	99.51	99.42	99.21	99.50
n	30	52	9	5

Table 5. Representative pyroxene phenocryst compositions

[Acronyms of sample lithologies are as noted in the text. FeO_t – All Fe analyzed as FeO. Mole fractions of the wollastonite (Wo), enstatite (En), and ferrosilite (Fs) pyroxene quadrilateral components. Mg# is molar Mg /(Mg+Fe). n is the number of individual analyses averaged to provide representative data. Numbers in parentheses are standard deviations about the average representative analyses]

[Core compositions]

	LSAS Opx	**LSAS Cpx**	**DLSA Opx**	**DLSA Cpx**	**DIA Opx**	**DIA Cpx**
SiO_2	53.29 (0.72)	52.39 (0.57)	53.33 (0.10)	51.64 (0.26)	52.69 (0.36)	52.10 (0.18)
TiO_2	0.12 (0.03)	0.29 (0.14)	0.16 (0.03)	0.33 (0.13)	0.14 (0.03)	0.26 (0.08)
Al_2O_3	0.80 (0.16)	1.46 (0.45)	0.85 (0.03)	1.78 (0.22)	1.36 (0.70)	1.26 (0.16)
FeO_t	19.81 (0.15)	9.16 (0.64)	20.22 (0.45)	9.01 (0.10)	19.45 (2.43)	8.92 (0.28)
MnO	0.71 (0.05)	0.40 (0.16)	0.76 (0.04)	0.35 (0.09)	0.77 (0.36)	0.52 (0.03)
MgO	23.95 (0.36)	14.76 (0.27)	24.32 (0.23)	14.77 (0.13)	24.46 (1.61)	14.56 (0.20)
CaO	1.05 (0.11)	21.93 (0.27)	1.16 (0.25)	21.39 (1.36)	0.99 (0.34)	23.10 (0.15)
Na_2O	0.04 (0.01)	0.35 (0.06)	0.04 (0.05)	0.35 (0.06)	0.02 (0.03)	0.36 (0.02)
Totals	99.76	100.74	100.84	99.61	99.89	101.05
Wo	2	43	2	43	2	45
En	66	41	66	41	67	40
Fs	32	15	32	15	31	15
Mg #	0.68	0.74	0.68	0.75	0.69	0.75
n	5	3	3	2	3	2

	Banded Opx	**Banded Cpx**	**HSA Opx**	**HSA Cpx**
SiO_2	53.57 (0.39)	51.27 (2.74)	52.68 (0.83)	51.54
TiO_2	0.17 (0.02)	0.63 (0.63)	0.20 (0.04)	0.48
Al_2O_3	0.73 (0.13)	3.29 (3.17)	0.94 (0.15)	4.27
FeO_t	20.01 (0.49)	8.44 (0.72)	19.69 (1.34)	5
MnO	0.71 (0.04)	0.33 (0.13)	0.74 (0.18)	0.05
MgO	24.06 (0.24)	14.60 (0.85)	23.45 (0.79)	16.43
CaO	1.07 (0.09)	22.16 (0.30)	2.33 (2.38)	20.58
Na_2O	0.02 (0.02)	0.28 (0.04)	0.04 (0.06)	0.2
Totals	100.33	101.00	100.06	98.54
Wo	2	45	5	43.11
En	66	41	64	47.88
Fs	32	14	31	8.28
Mg #	0.68	0.76	0.68	0.85
n	4	4	3	1

Table 5. Representative pyroxene phenocryst compositions.—Continued

[Acronyms of sample lithologies are as noted in the text. FeO_t—All Fe analyzed as FeO. Mole fractions of the wollastonite (Wo), enstatite (En), and ferrosilite (Fs) pyroxene quadrilateral components. Mg# is molar Mg /(Mg+Fe). n is the number of individual analyses averaged to provide representative data. Numbers in parentheses are standard deviations about the average representative analyses]

[Rim compositions]

	LSAS Opx rim	LSAS Cpx rim 1	LSAS Cpx rim 2	DLSA Opx rim 1	DLSA Opx rim 2	DLSA Cpx rim	DIA Opx rim 1
SiO_2	53.75 (0.49)	50.44 (1.14)	53.96	53.04 (0.04)	49.06	51.48 (0.15)	53.21 (0.35)
TiO_2	0.15 (0.04)	0.75 (0.21)	0.18	0.16 (0.04)	0.75	0.30 (0.10)	0.16 (0.00)
Al_2O_3	0.84 (0.07)	4.41 (1.15)	1.49	0.80 (0.07)	5.11	1.62 (0.19)	0.79 (0.01)
FeO_t	19.49 (0.61)	8.52 (0.98)	19.07	19.31 (0.81)	7.03	9.15 (0.15)	20.32 (0.64)
MnO	0.65 (0.02)	0.12 (0.04)	0.61	0.67 (0.05)	0.17	0.37 (0.01)	0.78 (0.04)
MgO	24.18 (0.15)	15.06 (0.62)	23.95	24.40 (0.55)	15.28	14.97 (0.11)	24.37 (0.59)
CaO	1.06 (0.06)	20.40 (0.11)	1.26	1.10 (0.01)	20.52	21.94 (0.13)	1.07 (0.14)
Na_2O	0.01 (0.01)	0.24 (0.06)	0.23	0.03 (0.02)	0.27	0.35 (0.01)	0.01 (0.01)
Totals	100.13	99.92	100.75	99.48	98.2	100.15	100.70
Wo	2	42	3	2	42.87	43	2
En	67	43	66	67	44.42	41	66
Fs	31	14	31	31	11.67	15	32
Mg #	0.69	0.76	0.69	0.69	0.79	0.75	0.68
n	5	2	1	2	1	2	2

	DIA Opx rim 2	DIA Cpx rim	Banded Opx rim 1	Banded Opx rim 2	Banded Cpx rim	HSA Opx rim 1	HSA Opx rim 2	HSA Cpx rim
SiO_2	51.99	51.71 (0.74)	53.41 (0.74)	52.33	51.68 (1.70)	53.47 (0.23)	52.86	50.88
TiO_2	0.35	0.68 (0.01)	0.16 (0.03)	0.36	0.51 (0.34)	0.18 (0.02)	0.24	0.42
Al_2O_3	2.17	2.26 (0.39)	0.78 (0.19)	1.25	2.56 (1.44)	0.74 (0.06)	1.35	3.7
FeO_t	8.88	9.84 (0.74)	20.46 (0.35)	8.16	9.36 (0.57)	19.96 (0.22)	9.00	6.78
MnO	0.25	0.37 (0.13)	0.65 (0.05)	0.37	0.26 (0.06)	0.75 (0.15)	0.36	0.21
MgO	17.43	14.55 (0.07)	24.09 (0.45)	15.01	14.79 (0.40)	24.22 (0.11)	14.96	15.96
CaO	19.84	20.80 (0.37)	1.16 (0.11)	22.23	21.55 (1.22)	1.08 (0.10)	21.91	22.04
Na_2O	0.28	0.36 (0.03)	0.00 (0.00)	0.33	0.34 (0.05)	0.03 (0.04)	0.32	0.22
Totals	101.19	100.57	100.73	100.04	101.04	100.41	101.00	100.22
Wo	38	42	2	44.15	43	2	43.32	44.02
En	47	41	66	41.49	41	66	41.18	44.36
Fs	14	16	32	13.16	15	32	14.37	10.82
Mg #	0.78	0.73	0.68	0.77	0.74	0.69	0.75	0.81
n	1	2	3	1	4	2	1	1

Table 6. Representative Fe-Ti oxide pair analyses, temperatures, and oxygen fugacities from Augustine 2006 eruptive products.

[All analyses are averages of multiple points on individual grains; 1 standard deviation is in parentheses. Four select pairs from each lithology were chosen to represent the range of compositions, temperatures, and oxygen fugacities calculated from the oxide probe data. FeO_t is total Fe calculated to FeO. n is the number of analyses per grain. Temperature and oxygen fugacity (f_{O_2}) calculated using QUILF (Andersen and others, 1993) and then decreased by 30 degrees °C because the QUILF algorithm overestimates temperatures by 30 °C in magma with oxygen fugacity RRO (Rutherford and Devine, 1996)]

[HSA lithology]

	06AUMC010p1		**06AUMC010p1**		**06AUMC010p1**		**06AUMC010p1**		**06AUMC005cp1**		**06AUMC005cp1**		**06AUMC005cp1**		**06AUMC005cp1**	
	HSA		**HSA**		**HSA**		**HSA**		**Banded**		**Banded**		**Banded**		**Banded**	
Ti-magnetite																
	Pair 2a		Pair 3		Pair 5		Pair 8		Pair 1a		Pair 2		Pair 4		Pair 5	
TiO_2	8.05	(0.30)	7.12	(0.49)	7.54	(0.47)	7.68	(0.67)	7.28	(0.53)	7.34	(0.45)	7.37	(0.22)	7.28	(0.53)
Al_2O_3	2.36	(0.14)	2.19	(0.09)	2.07	(0.06)	2.00	(0.10)	2.00	(0.09)	2.04	(0.07)	1.99	(0.08)	2.00	(0.09)
FeO_t	81.17	(0.97)	82.08	(0.92)	80.12	(0.75)	82.87	(1.62)	82.17	(2.15)	81.26	(1.30)	82.57	(0.45)	82.17	(2.15)
MnO	0.42	(0.11)	0.47	(0.07)	0.41	(0.08)	0.45	(0.10)	0.43	(0.11)	0.42	(0.11)	0.40	(0.11)	0.43	(0.11)
MgO	1.95	(0.09)	1.80	(1.80)	1.72	(0.06)	1.70	(0.05)	1.59	(0.04)	1.61	(0.04)	1.55	(0.05)	1.59	(0.04)
Cr_2O_3	0.24	(0.05)	0.28	(0.07)	0.28	(0.04)	0.24	(0.06)	0.27	(0.03)	0.29	(0.04)	0.27	(0.05)	0.27	(0.03)
SiO_2	0.07	(0.01)	0.11	(0.11)	0.11	(0.04)	0.08	(0.02)	0.08	(0.04)	0.05	(0.03)	0.04	(0.05)	0.08	(0.04)
Total	94.26		94.05		92.31		95.02		98.32		93.01		94.19		92.47	
n	4		7		9		11		15		9		9		11	
Ilmenite																
TiO_2	35.15	(1.95)	33.58	(3.44)	33.19	(2.15)	31.14	(1.74)	34.03	(1.65)	33.22	(2.48)	32.75	(1.97)	34.03	(1.65)
Al_2O_3	0.43	(0.02)	0.40	(0.121)	0.39	(0.39)	0.40	(0.04)	0.36	(0.04)	0.37	(0.03)	0.37	(0.04)	0.36	(0.04)
FeO_t	59.23	(1.12)	59.18	(1.41)	58.35	(0.52	60.69	(1.28)	58.66	(1.47)	60.86	(0.94)	60.02	(0.36)	58.66	(1.47)
MnO	0.26	(0.06)	0.33	(0.05)	0.27	(0.03)	0.28	(0.05)	0.27	(0.08)	0.29	(0.11)	0.27	(0.10)	0.27	(0.08)
MgO	2.03	(0.03)	1.92	(0.11)	1.79	(0.04)	1.60	(0.05)	1.77	(0.07)	1.58	(0.08)	1.63	(0.04)	1.77	(0.07)
Cr_2O_3	0.12	(0.06)	0.10	(0.05)	0.09	(0.03)	0.11	(0.07)	0.08	(0.07)	0.12	(0.05)	0.10	(0.04)	0.08	(0.07)
SiO_2	0.01	(0.02)	0.03	(0.04)	0.01	(0.01)	0.07	(0.07)	0.04	(0.04)	0.04	(0.09)	0.01	(0.02)	0.04	(0.04)
Total	97.23		95.54		94.09		94.28		95.21		96.48		95.14		94.13	
n	3		7		6		8		5		11		13		5	
T (°C)	840		823		839		855		826		837		838		840	
log f_{O_2}	-10.57		-10.72		-10.53		-10.16		-10.75		-10.51		-10.50		-10.40	

Table 6. Representative Fe-Ti oxide pair analyses, temperatures, and oxygen fugacities from Augustine 2006 eruptive products.—Continued

[All analyses are averages of multiple points on individual grains; 1 standard deviation is in parentheses. Four select pairs from each lithology were chosen to represent the range of compositions, temperatures, and oxygen fugacities calculated from the oxide probe data. FeO_t is total Fe calculated to FeO. n is the number of analyses per grain. Temperature and oxygen fugacity (f_{O_2}) calculated using QUILF (Andersen and others, 1993) and then decreased by 30 degrees °C because the QUILF algorithm overestimates temperatures by 30 °C in magma with oxygen fugacity RRO (Rutherford and Devine, 1996)]

[DIA and DLA lithologies]

	06AUMRT006		06AUMRT006		06AUJFL001b		06AUMRT009b		06AUMC008bp1		06AUMC008bp1		06AUMC008bp1		06AUMC005cp5	
	DIA		DIA		DIA		DLSA		LSAS		LSAS		LSAS		LSAS	
Ti-magnetite	DIA Pair 1		Pair 3		Pair 1		Pair 1		Pair 1		Pair 3		Pair 6		Pair 4	
TiO_2	8.31	(1.00)	7.54	(0.75)	7.22	(0.43)	10.19	(0.93)	7.73	(0.35)	8.01	(1.06)	11.33	(1.57)	10.40	(1.15)
Al_2O_3	2.18	(0.08)	1.88	(0.21)	2.06	(0.08)	2.11	(0.06)	1.92	(0.10)	2.25	(0.06)	3.20	(0.27)	3.33	(0.13)
FeO_t	81.39	(1.20)	81.22	(0.63)	82.52	(0.79)	80.05	(1.27)	81.72	(1.23)	81.55	(0.95)	76.54	(0.65)	78.72	(0.65)
MnO	0.42	(0.13)	0.43	(0.08)	0.43	(0.07)	0.43	(0.07)	0.40	(0.40)	0.43	(0.09)	0.41	(0.07)	0.36	(0.07)
MgO	2.09	(0.09)	1.94	(0.14)	1.73	(0.04)	2.55	(0.09)	2.00	(0.05)	2.09	(0.08)	2.77	(0.25)	3.05	(0.13)
Cr_2O_3	0.27	(0.04)	0.22	(0.02)	0.30	(0.06)	0.30	(0.04)	0.29	(0.05)	0.31	(0.07)	0.12	(0.02)	0.18	(0.07)
SiO_2	0.29	(0.06)	0.50	(0.36)	0.51	(0.19)	0.27	(0.07)	0.05	(0.02)	0.04	(0.04)	0.11	(0.03)	0.13	(0.20)
Total	94.96		93.72		94.77		95.90		94.10		94.69		94.48		96.16	
n	15		6		14		14		11		5		5		6	
Ilmenite																
TiO_2	34.11	(1.95)	34.88	(2.01)	32.29	(2.06)	35.36	(1.54)	36.38	(2.68)	36.34	(1.25)	36.01	(0.73)	30.82	(5.10)
Al_2O_3	0.44	(0.04)	0.36	(0.04)	0.38	(0.05)	0.52	(0.08)	0.49	(0.21)	0.41	(0.04)	0.63	(0.03)	0.91	(0.51)
FeO_t	59.86	(0.97)	59.37	(0.91)	60.45	(1.20)	58.37	(1.13)	57.60	(2.23)	57.46	(0.66)	59.34	(0.48)	60.62	(3.68)
MnO	0.26	(0.08)	0.28	(0.07)	0.24	(0.10)	0.25	(0.04)	0.26	(0.10)	0.32	(0.06)	0.18	(0.07)	0.23	(0.12)
MgO	2.05	(0.08)	1.96	(0.06)	1.77	(0.14)	2.37	(0.16)	2.41	(0.14)	2.20	(0.09)	2.56	(0.05)	2.95	(0.33)
Cr_2O_3	0.11	(0.04)	0.10	(0.06)	0.11	(0.04)	0.12	(0.03)	0.06	(0.05)	0.11	(0.06)	0.12	(0.02)	0.12	(0.04)
SiO_2	0.12	(0.16)	0.18	(0.11)	0.46	(0.24)	0.17	(0.05)	0.05	(0.08)	0.02	(0.02)	0.01	(0.01)	0.03	(0.02)
Total	96.95		97.12		95.70		97.17		97.24		96.86		98.85		95.68	
n	13		13		16		7		9		6		4		4	
T (°C)	853		829		836		890		825		827		925		968	
log f_{0_2}	-10.31		-10.70		-10.48		-9.91		-10.87		-10.84		-9.45		-8.51	

Table 7. Representative olivine analyses from Augustine 2006 eruptive products.

[Each analysis is representative of one point from core or rim of olivine crystal. Relative error is less than 1 % on each analysis. Texture refers to symplectite rimmed (Symplectite), euhedral unrimmed (Euhedral), pyroxene rimmed (Px rimmed), and hopper (Hopper) olivine respectively. FeO_t is total Fe calculated as Fe^{2+}. Fo is mole percent forsterite content. Mg# is mols Mg divided by total mols of Mg, Fe^{2+}, and Fe^{3+}]

	HSA		**Banded**		**Banded**		**DIA**		**DIA**	
Sample ID	06AUMRT017b		06AUMRT037a		06AUMC008a		06AUJFL001b		06AUJFL001b	
Texture	Symplectite		Symplectite		Euhedral		Symplectite		Px rimmed	
	Core	Rim	Core	Rim	Core	Rim	Core	Rim	Core	Rim
SiO_2	39.22	38.25	38.42	37.75	39.24	39.40	39.64	38.06	40.42	40.26
TiO_2	0.03	0.01	0.02	0.00	0.04	0.04	0.02	0.05	0.01	0.01
Cr_2O_3	0.01	0.02	0.00	0.00	0.03	0.11	0.01	0.00	0.00	0.05
FeOt	17.33	22.01	20.74	21.18	15.09	14.80	20.20	23.05	13.70	13.71
MnO	0.37	0.36	0.36	0.46	0.20	0.22	0.44	0.50	0.27	0.05
MgO	44.54	40.58	39.68	40.12	43.70	43.36	40.14	38.78	46.97	46.28
CaO	0.13	0.05	0.06	0.09	0.15	0.11	0.07	0.06	0.16	0.18
Total	101.78	101.48	99.44	99.76	98.45	98.05	100.54	100.68	101.76	100.62
Fo	81.77	76.38	77.02	76.76	83.58	83.73	77.60	74.58	85.70	85.71
Mg#	0.82	0.77	0.77	0.77	0.84	0.84	0.78	0.75	0.86	0.86

	DLSA		**DLSA**		**DLSA**		**LSAS**		**LSAS**	
Sample ID	06AUMRT032a		06AUMRT032a		06AUMC008bp3		06AUJFL001e		06AUMC008bp1	
Texture	Euhedral		Hopper		Symplectite		Px rimmed		Euhedral	
	Core	Rim	Core	Rim	Core	Rim	Core	Rim	Core	Rim
SiO_2	40.31	41.00	39.13	38.73	40.21	39.42	39.24	38.45	39.81	38.91
TiO_2	0.00	0.00	0.03	0.00	0.00	0.02	0.02	0.00	0.10	0.02
Cr_2O_3	0.03	0.03	0.03	0.04	0.00	0.03	0.01	0.03	0.04	0.05
FeOt	13.06	13.22	16.02	19.17	21.45	20.41	14.42	15.16	15.76	18.74
MnO	0.12	0.23	0.27	0.39	0.45	0.30	0.28	0.18	0.20	0.37
MgO	46.89	46.04	45.73	43.14	37.97	38.30	46.47	45.30	43.20	40.49
CaO	0.18	0.18	0.17	0.15	0.05	0.06	0.16	0.16	0.17	0.19
Total	100.89	100.98	101.60	101.87	100.14	98.54	100.82	99.49	99.29	98.77
Fo	86.38	85.92	83.34	79.72	75.54	76.72	84.92	84.03	82.82	79.07
Mg#	0.86	0.86	0.84	0.80	0.76	0.77	0.85	0.84	0.83	0.79

Table 8. Representative amphibole phenocryst compositions from Augustine 2006 eruptive products.

[Sample lithology acronyms are as noted in the text. One standard deviation is in parentheses. FeO_t is total Fe calculated as Fe^{2+}. Compositions are averages of n points on a single phenocryst]

	06AUMC004cp1	**06aujfl001b**	**06aumrt032b**	**06aumrt037e**	**06aumrt037c**	**06aumc013a**
	HSA	DIA	DIA	DIA	LSAS	FGGI
SiO_2	45.52 (0.61)	42.74 (0.42)	45.84 (0.22)	45.90	44.28 (0.17)	45.00 (0.80)
TiO_2	2.03 (0.48)	2.10 (0.63)	1.48 (0.33)	1.81	1.44 (0.12)	1.52 (0.62)
Al_2O_3	8.15 (0.17)	12.09 (0.19)	8.63 (0.11)	9.21	9.31 (0.21)	9.26 (0.52)
FeO_t	11.63 (0.28)	10.97 (0.36)	12.64 (0.38)	12.70	13.00 (0.33)	12.08 (0.41)
MnO	0.25 (0.04)	0.18 (0.06)	0.37 (0.14)	0.37	0.44 (0.09)	0.38 (0.11)
MgO	15.68 (0.15)	14.89 (0.07)	14.91 (0.18)	14.91	14.77 (0.29)	15.14 (0.29)
CaO	11.83 (0.63)	12.17 (0.56)	12.86 (0.38)	12.29	11.15 (0.85)	12.75 (0.10)
K_2O	0.15 (0.02)	0.24 (0.01)	0.12 (0.02)	0.22	0.17 (0.03)	0.11 (0.04)
Na_2O	1.77 (0.21)	2.30 (0.19)	1.64 (0.05)	1.74	1.78 (0.07)	1.79 (0.15)
Cl	0.06 (0.04)	0.05 (0.04)	0.07 (0.4)	0.06	0.06 (0.01)	0.08 (0.02)
Total	97.08 (1.09)	97.73 (0.72)	98.56 (0.82)	99.22	96.38 (1.61)	98.10 (0.69)
n	4	5	4	1	3	4

Appendixes 1–5. Additional Descriptions and Compositional Data for Samples Used in This Study

Appendix 1. Samples of Augustine Volcano 2006 eruptive products used in this study, sorted by eruptive unit and lithologic type.

[This appendix appears only in the digital version of this work—in the DVD-ROM that accompanies the printed volume and as a separate file accompanying this chapter on the Web at http://pubs.usgs.gov/pp/1769]

This table lists samples of Augustine Volcano 2006 eruptive products used in this study. The samples are sorted by eruptive unit and lithologic type.

Appendix 2. Modal Mineralogy and Point Count Data for the Augustine Eruptive Lithologies.

[This appendix appears only in the digital version of this work—in the DVD-ROM that accompanies the printed volume and as a separate file accompanying this chapter on the Web at http://pubs.usgs.gov/pp/1769]

This table presents the modal mineralogy data, determined from 1,000 point counts from thin sections of each lithology. These data form the basis for the average modal mineralogy data presented in table 2 and figure 4.

Appendix 3. Augustine Whole-Rock Geochemical Analyses.

[This appendix appears only in the digital version of this work—in the DVD-ROM that accompanies the printed volume and as a separate file accompanying this chapter on the Web at http://pubs.usgs.gov/pp/1769]

This appendix includes data collected by the Washington State University Geoanalytical Laboratory for the Alaska Volcano Observatory. The data include analyses from 2006 Augustine eruptive products, as well as pre-2006 historical, and early Holocene and Pleistocene samples.

Appendix 4. Groundmass Glass Electron Microprobe Analyses from Augustine 2006 Samples used in this Study.

[This appendix appears only in the digital version of this work—in the DVD-ROM that accompanies the printed volume and as a separate file accompanying this chapter on the Web at http://pubs.usgs.gov/pp/1769]

This appendix includes glass compositional analyses from several major lithologies form the 2006 eruptive products. It also includes glass data from tephra samples from December 24, 2005 and January 13, 14, and 17,2006. Tephra analyses from 1986 samples are also included for comparison. The data included in this appendix is also plotted in figure 11 in the text.

Appendix 5. Representative Electron Microprobe Analyses of Plagioclase Phenocrysts in Augustine 2006 Samples used in this Study.

[This appendix appears only in the digital version of this work—in the DVD-ROM that accompanies the printed volume and as a separate file accompanying this chapter on the Web at http://pubs.usgs.gov/pp/1769]

The electron microprobe analyses presented here represent the core to rim transects shown in figure 12 of the text.